SIMULATION OF OPTICAL FIBRE COMMUNICATION SYSTEMS INFLUENCED BY STIMULATED BRILLOUIN SCATTERING

ALEXANDER STEPHEN RAE

Doctor of Philosophy

THE UNIVERSITY OF ASTON IN BIRMINGHAM

October 1996

THE UNIVERSITY OF ASTON IN BIRMINGHAM

SIMULATION OF OPTICAL FIBRE COMMUNICATION SYSTEMS INFLUENCED BY STIMULATED BRILLOUIN SCATTERING

ALEXANDER STEPHEN RAE

Doctor of Philosophy

1996

Summary

Boyd's SBS model which includes distributed thermal acoustic noise (DTAN) has been enhanced to enable the Stokes-spontaneous density depletion noise (SSDDN) component of the transmitted optical field to be simulated, probably for the first time, as well as the full transmitted field. SSDDN would not be generated from previous SBS models in which a Stokes seed replaces DTAN. SSDDN becomes the dominant form of transmitted SBS noise as model fibre length (MFL) is increased but its optical power spectrum remains independent of MFL. Simulations of the full transmitted field and SSDDN for different MFLs allow prediction of the optical power spectrum, or system performance parameters which depend on this, for typical communication link lengths which are too long for direct simulation.

The SBS model has also been innovatively improved by allowing the Brillouin Shift Frequency (BSF) to vary over the model fibre length, for the nonuniform fibre model (NFM) mode, or to remain constant, for the uniform fibre model (UFM) mode. The assumption of a Gaussian probability density function (pdf) for the BSF in the NFM has been confirmed by means of an analysis of reported Brillouin amplified power spectral measurements for the simple case of a nominally step-index single-mode pure silica core fibre. The BSF pdf could be modified to match the Brillouin gain spectra of other fibre types if required.

For both models, simulated backscattered and output powers as functions of input power agree well with those from a reported experiment for fitting Brillouin gain coefficients close to theoretical. The NFM and UFM Brillouin gain spectra are then very similar from half to full maximum but diverge at lower values. Consequently, NFM and UFM transmitted SBS noise powers inferred for long MFLs differ by 1-2 dB over the input power range of 0-15 dBm. This difference could be significant for AM-VSB CATV links at some channel frequencies.

The modelled characteristic of Carrier-to-Noise Ratio (CNR) as a function of input power for a single intensity modulated subcarrier is in good agreement with the characteristic reported for an experiment when either the UFM or NFM is used. The difference between the two modelled characteristics would have been more noticeable for a higher fibre length or a lower subcarrier frequency.

Index terms: nonlinear fibre optics, computer modelling, SBS, optical fibre nonuniformity, optical fibre model

Acknowledgements

I would like to thank EPSRC and GEC Marconi Materials Technology Ltd at Caswell for sponsoring me during the course of this project.

CONTENTS

LIST OF FIGURES AND TABLES

1. INTRODUCTION

1.1 OPTICAL FIBRE COMMUNICATION SYSTEMS

The development of single mode optical fibre with a loss of less than 0.2 dB/km at a wavelength of 1550 nm, together with single frequency semiconductor lasers, has enabled optical fibre communication systems to be designed for a wide variety of applications including long distance telecommunications, CATV, packet switched data networks, secure military communications, phased array antennas [1.1.1]-[1.1.3] and cellular radio networks [1.1.4]-[1.1.6]. Optical fibres offer considerable advantages over alternative transmission media such as copper cables, radio and satellite in terms of potential bandwidth, immunity from electromagnetic interference and low loss [1.1.7]-[1.1.10]. For long distance interactive audio or video communications, optical fibre links incur significantly smaller delays than those introduced by geostationary satellite channels [1.1.8].

The very high bandwidth of about 25,000 GHz theoretically available for optical fibre transmission is an important factor which favours its installation in any communication system where an increase in demand for capacity is probable. One recent and very striking example of such a demand is that for the bandwidth per user of the World Wide Web, which has accelerated to a factor of eight per year [1.1.7], [1.1.11]. Part of this increase is associated with the use of the Internet for the last four years or so to carry audio and video traffic around the world [1.1.7], [1.1.12].

Optical fibre is being installed at a high rate throughout the world. In the USA, the installation rate has been 4000 strand miles per day for many years and a total of over 10 million strand miles has now been accumulated [1.1.7], [1.1.13]. The interconnections between telecommunication company networks and cable TV trunk distribution links have been more or less completed so that fibre has come closer to

the user. In the UK, CATV companies have installed 45,000 km of fibre in hybrid fibre coax (or "fibre-to-the-neighbourhood") networks [1.1.14], [1.1.15].

In order to meet the demand for increased capacity in communication networks, worldwide research is being carried out into the use of a greater proportion of the theoretical bandwidth of optical fibres. One important approach to this aim is Wavelength Division Multiplexing (WDM) in which tuneable lasers or multiple wavelength laser arrays, together with other wavelength-selective optical components, enable simultaneous transmission over a single fibre at several wavelengths. WDM allows the capacity of a fibre link to be increased beyond that of the individual optoelectronic components. An extension of the simple WDM point-to-point link approach is that of all-optical networks in which the path between user nodes remains entirely optical [1.1.7]. Each path may be optically amplified and wavelength shifted without being converted back to an electrical signal between nodes. Two examples of all-optical networks are the broadcast and select network, which may be used for Local Area Networks (LANs) and Metropolitan Area Networks (MANs), and the wavelength routing mesh network, which is appropriate for Wide Area Networks (WANs)[1.1.7], [1.1.16].

Work on wideband all-optical WDM networks is being sponsored in the USA by the Advanced Research Projects Agency (ARPA) [1.1.17]-[1.1.19] and in Europe by the Commission of the European Communities under the RACE (Research and Development in Advanced Communications in Europe) programme [1.1.20], [1.1.21]. Other examples of American research are the MONET (Multiwavelength Optical Networking) programme [1.1.22] and STARNET broadband optical WDM LAN [1.1.23], while in Japan, NTT have demonstrated the performance of an all-optical self-healing ring network [1.1.24]. The principal ARPA funded all-optical WDM network testbed employs 20 wavelengths with a data-rate-per-wavelength from 10 Mbit/s to 10 Gbit/s [1.1.17]. Ten wavelengths are partitioned for use in the passive broadcast LAN and ten are shared between the passive wavelength-routed MAN and the configurable wavelength-routed WAN. In an alternative

approach, the same ARPA funded Consortium on Wideband All-Optical Networks is also investigating architecture and technology for single-stream, 100 Gbit/s shared media area networks (LAN/MAN) with slotted TDM [1.1.25]. Experimental results of 80 Gbit/s 90 km soliton transmission and simulations up to 111 Gbit/s over 1000 km are also given in the same paper.

The capacity of long distance and transoceanic optical transmission systems will also need to be increased to meet the growing demand for interactive video, or multimedia, services. The use of WDM for these links is an attractive alternative to very high speed TDM [1.1.26], [1.1.27]. Before the development of Erbium Doped Fibre Amplifiers (EDFAs), with output powers greater than 20 dBm [1.1.28], [1.1.29] and gains greater than 25 dB [1.1.28], [1.1.30], WDM transmission distances were limited to those obtainable without intermediate repeaters, since a WDM repeater consisting of a wavelength demultiplexer, individual optoelectronic 3R (retiming, reshaping and regenerating) repeaters for all the wavelengths and a wavelength multiplexer was not considered practical [1.1.26]. Indeed, even for single wavelength links, EDFA repeaters are to be preferred to traditional 3R repeaters. The first transoceanic EDFA systems were installed in 1995 with a single 5 Gbit/s optical channel [1.1.31], twice the capacity of the most advanced digital regenerator based undersea fibre optic system [1.1.27].

The transmission of many WDM channels over transoceanic distances can be limited by a variety of phenomena, including the finite bandwidth of the EDFA repeaters, the nonlinear interactions between channels and the noise accumulation along the chain of amplifiers [1.1.27]. The effects of these fibre optic nonlinearities can be reduced by managing the group velocity dispersion over the length of the link. Passive gain equalisation can increase the usable bandwidth in long amplifier chains by a factor of two to three. Bit-synchronous polarization and phase modulation in Non-Return-to-Zero (NRZ) transmission systems can remove the excess noise accumulation caused by polarisation hole-burning and simultaneously improve transmission performance by decreasing Four-Wave Mixing between channels and

increasing the received eye opening. By adopting these techniques and by using Forward Error Correction, 20 WDM channels of 5 Gbit/s (100 Gbit/s in total) have been transmitted over 9100 km by means of a circulating loop experiment [1.1.27], [1.1.32].

The importance of modelling WDM and even single wavelength optical fibre links is apparent from the number and complexity of effects which have been taken into account in this and other experiments. The modelling of optical communication systems is discussed in the next section, with special emphasis on nonlinear effects in optical fibres.

1.2 COMPUTER MODELLING OF OPTICAL COMMUNICATION SYSTEMS

The principal linear effects for an optical fibre are loss and group velocity dispersion (GVD) [1.2.1]. Primary nonlinear effects can be divided into

i those resulting from third order susceptibility:

Self Phase Modulation (SPM), Cross Phase Modulation (XPM) and Four Wave Mixing (FWM),

ii stimulated inelastic scattering effects:

Stimulated Brillouin Scattering (SBS) and Stimulated Raman Scattering (SRS).

SPM refers to the self-induced intensity-dependent nonlinear phase shift experienced by an optical field during propagation, while XPM refers to the nonlinear phase shift of an optical field induced by a copropagating field at a different wavelength. FWM is the generation of a fourth optical frequency component from three optical frequency components.

SBS is initiated by backscattering of light from an effective grating formed through strain-optic interaction by a thermally induced acoustic wave [1.2.2]. SBS growth occurs through amplification of the acoustic wave due to electrostriction, whereby a density change is produced from light intensity variation induced by the beating of the pump (incident) and Stokes (backscattered) waves [1.2.3]. As the input power progressively increases above the SBS threshold, backscattered light at an optical frequency lower than that of the incident light by the Brillouin shift frequency intensifies, while the transmitted power reaches a limiting value. The theory of SBS will be described in more detail in chapters 2 and 3.

SRS involves the interaction between light and the vibrational modes of silica molecules and results in the growth of one or more frequency down-shifted optical waves (Stokes waves) at the expense of the incident optical wave (pump wave) [1.2.1], [1.2.4], [1.2.5].

In WDM systems, any of the above nonlinear effects can dominate high power performance depending on the number of channels, channel spacing, modulation format, data rate or modulation bandwidth, fibre GVD, loss, length, whether optical amplifiers are used as intermediate repeaters and other factors [1.2.4], [1.2.6]-[1.2.12].

Zou et al. have simulated the combined effects of SPM, XPM, SRS, GVD and loss on various examples of dispersion managed WDM transmission system, in which two to eight 10 Gbit/s NRZ WDM channels are transmitted through a cascade of EDFAs over distances of up to 4,000 km [1.2.13]. The various lengths and sequences of fibre sections of alternating fibre type, chosen from conventional single-mode fibre, dispersion-shifted fibre and dispersion-compensating fibre, are such that the total link GVD is zero at one of the channel wavelengths. However, the GVD over any small section is that of the local fibre type and is very significant. They argue that the local GVD causes a phase mismatch between channels thereby

destroying any efficient FWM production, so that FWM is neglected in their model. SBS is not taken into account either, on the basis that the bandwidth associated with the effect is extremely narrow in comparison to the data channel bandwidths.

However, this assumption with regard to SBS may not always be justified for NRZ intensity modulation WDM systems. For narrow linewidth lasers followed by external intensity modulation, a substantial component of power exists at the optical carrier frequency. SRS will cause the longer wavelength channels to be amplified at the expense of the shorter wavelength channels. If the power in the longest wavelength channel remains at a power of the order of milliwatts over an EDFA cascaded link length of thousands of kilometres, the effective interaction length for SBS would also be a substantial proportion of the link length if a reverse optical path were allowed through the EDFAs. The effects of SBS would then be very significant. More usually, isolators would be used at each end of every EDFA, so that depletion of the carrier by SBS and the introduction of SBS noise should be considered separately for every fibre section between EDFAs. Even in this case, the accumulation of carrier depletion and noise due to SBS over the entire link length may not always be negligible. The phase modulation applied to the WDM system of [1.1.27] and [1.1.32] would reduce the power in any given optical band of bandwidth equal to the Brillouin gain linewidth and so help to suppress SBS.

In the above model of [1.2.13], the NRZ pulses are approximated to as super-Gaussian pulses. Propagation over the link in the presence of SPM, XPM, SRS, GVD and loss is simulated by numerical solution of an appropriate version of the nonlinear Schrödinger equation [1.2.1] for each of the WDM channels. The split-step Fourier method, whereby a solution step in the time domain for the nonlinearities is alternated with a solution step in the frequency domain for GVD, is applied [1.2.1].

1.3 STIMULATED BRILLOUIN SCATTERING

SBS is of special interest in the design of single wavelength, long distance, high data rate links for which remote electrical powering of optical amplifiers is not permissible or desirable. In such cases, a compact optical spectrum is necessary to minimise the effects of GVD and the launch power is maximised. Two frequently adopted alternative schemes are external intensity modulation of a narrow linewidth laser, followed by a direct detection receiver, and direct frequency modulation, often known as CPFSK (Continuous Phase Frequency Shift Keying), followed by a heterodyne detection receiver. SBS can lead to a limiting of part of the output optical power spectrum from the fibre as the input power is increased, with consequent distortion of the detected signal and a sensitivity penalty. It can also result in optical noise and hence a Bit Error Rate (BER) floor. The effects of SBS in introducing demodulated waveform distortion, sensitivity penalties and BER floors in coherent CPFSK systems [1.3.1]-[1.3.3] and externally intensity modulated links [1.3.4], [1.3.5] have recently been studied experimentally. For high data rate external intensity modulation, it is possible to raise the SBS threshold power by modulating the optical frequency or phase of the launched signal at a sufficiently low rate for a dispersion penalty not to be incurred[1.3.6]-[1.3.9]. For coherent CPFSK, this technique is not likely to be as practicable since the local oscillator in the receiver is normally held at a constant frequency. Instead, the SBS threshold power has been increased by inserting a number of fibre sections each with a significantly different Brillouin shift frequency [1.3.10]. The same effect has been used to design fibres with higher thresholds than for conventional fibres [1.3.11]-[1.3.13]. Alternatively, the effects of SBS on the measured BER for CPFSK have been ameliorated by adjusting the threshold voltage in the decision circuit [1.3.2].

Another important example of a system whose design may be influenced by SBS is that of externally modulated AM-VSB CATV transmission [1.3.14]-[1.3.16]. The importance of using SMF links for this type of CATV distribution and the advantages of applying external rather than direct laser modulation are discussed in

Appendix A1.1, together with a representative configuration for such a system, power spectra at various points and typical parameters. As the optical input power increases above the threshold, SBS noise at the fibre link output increases sharply, so that the Carrier-to-Noise Ratio of a modulated video channel reaches a maximum value and then decreases rapidly. As for the digital external intensity modulation case considered above, external phase modulation may be suitably applied to increase the SBS threshold [1.3.15], [1.3.17]-[1.3.19]. Although direct frequency modulation also increases the threshold, the residual AM can introduce unacceptable interference in the band of the CATV channels [1.3.16]. External phase modulation is effective in reducing interferometric intensity noise [1.3.17] and composite second order distortion due to SPM [1.3.20] as well as the influence of SBS.

It can be seen from the above discussion that there is considerable recent interest both in the experimental characterisation of the performance of these systems in the presence of SBS and also in the efficiency and side effects of techniques for increasing the threshold. In order that an effective worst case design approach can be adopted, an analytical method or computer model is required which will enable prediction of system performance under SBS conditions with and without the application of threshold increasing techniques. It will be shown in the next chapter that previously reported analytical and numerical models fall short of this requirement in important respects. The primary objective of this project has been to provide a simulation tool for systems influenced by SBS which represents a substantial improvement on previous models, with particular emphasis on externally modulated AM-VSB CATV transmission links.

In chapter 2, an overview of the theory of SBS is given, followed by a discussion of previously reported work on the modelling of SBS in optical fibre systems. In chapter 3, a description is given of a numerical SBS model based on existing theory for a uniform fibre, whereby the Brillouin shift frequency (BSF) may be regarded as invariant over the length of the fibre. Simulated SBS characteristics are compared with those from a published experiment. A new method of simulating the

transmitted power spectrum expected at fibre lengths too long to simulate directly is described and used to generate examples of these spectra for the parameters of the same published experiment.

In chapter 4, the uniform fibre model (UFM) is adapted to allow the BSF in each small section of the model fibre to be different, so that fibre nonuniformity is represented. The validity of an assumption made about the probability density function of the BSF is confirmed for the case of a pure silica fibre from an analysis of reported measurements. Simulated SBS characteristics using this nonuniform fibre model (NFM) are compared with those from the reported experiment featured in the UFM comparison example of chapter 3. Similarities and differences between the UFM and NFM SBS characteristics of backscattered, transmitted signal and transmitted noise powers as functions of input power are illustrated and discussed.

In chapter 5, the computer model is extended to enable the effects of SBS on the carrier-to-noise ratio (CNR) of a single subcarrier channel of an optical AM CATV link to be simulated. Simulations of CNR at different model fibre lengths are used together with the simulated CNR inferred for very high lengths in order to predict the CNR at the real fibre length for a reported experiment. For both the UFM and the NFM, contributions of CNR from SBS are combined with those from the experimental link with the fibre replaced by a linear optical attenuator and from multipath interference over the fibre length to give total predicted CNRs which can be directly compared with the measured CNRs for the experimental link with fibre.

In chapter 6, conclusions from the work presented are stated and ideas for extending the model to simulate Bit Error Rates of digital transmission systems under SBS conditions are discussed, together with issues relating to the incorporation of Group Velocity Dispersion and other optical nonlinear effects within the model.

2. ANALYSIS AND COMPUTER MODELLING OF STIMULATED BRILLOUIN SCATTERING IN OPTICAL FIBRE SYSTEMS

Before discussing previously reported work on the modelling of SBS in optical fibre systems, it is appropriate to give an overview of the theory of SBS. In section 2.1, the theory is described with reference to frequently used terms such as Brillouin shift frequency, Brillouin gain and Brillouin threshold. In section 2.1.4, a simple theoretical technique for evaluating the effect of signal modulation on the Brillouin threshold is outlined. The Brillouin gain spectrum for fused silica is discussed in section 2.1.5 and the influence of acoustic guidance and material considerations on Brillouin gain spectra of single mode fibres in section 2.1.6.

Section 2.2 on computer models begins, in section 2.2.1, with a discussion of the required properties of a SBS model. Techniques for modelling SBS are described in section 2.2.2, with particular reference to the use of Stokes seeds for initiating the SBS growth process and the preferability of including in the model a distributed fluctuating source which imitates thermal acoustic noise more directly. In section 2.2.3, some examples of SBS modelling are discussed. These include the work of Höök and Bolle in simulating intensity waveforms of a PSK transmission system and that of Boyd and Gaeta in simulating statistical and spectral characteristics of SBS backscattered light by incorporating a distributed fluctuating source description of thermal acoustic noise.

2.1 THEORY

2.1.1 Brillouin Shift Frequency

The process of SBS can be described classically as a parametric interaction among the pump wave (usually the input optical signal, here assumed to be CW and with a

very narrow linewidth), the Stokes wave and an acoustic wave [1.2.1]. A thermally generated acoustic wave produces a corresponding periodic modulation in refractive index through strain-optic interaction [1.2.2]. This index grating scatters the pump light through Bragg diffraction. The scattered light is downshifted in optical frequency by the acoustic frequency, ν_a, as a result of the Doppler effect, since the grating is moving at the acoustic velocity, v_a. The scattered light is most intense if the Bragg condition

$$2\lambda_a \sin(\theta) = \lambda_o/n \qquad (2.1.1)$$

is satisfied, where λ_a (= v_a/ν_a) and λ_o are the acoustic and optical wavelengths, respectively, n is the refractive index of the fibre core and θ is the angle between the incident optical beam and the normal to the acoustic direction of propagation [1.3.5].

Equation (2.1.1) can also be derived by viewing the scattering process quantum-mechanically as if the annihilation of a pump photon creates simultaneously a Stokes photon and an acoustic phonon. Since both the energy and the momentum must be conserved during each scattering event, the frequencies and the wave vectors of the three waves are related by

$$\nu_a = \nu_p - \nu_s \qquad (2.1.2)$$

$$\mathbf{k}_a = \mathbf{k}_p - \mathbf{k}_s \qquad (2.1.3)$$

where ν_a, ν_p and ν_s are the frequencies and $\mathbf{k}_a$, $\mathbf{k}_p$ and $\mathbf{k}_s$ are the wave vectors of the acoustic, pump and Stokes waves, respectively, and

$$|\mathbf{k}_s| \sim |\mathbf{k}_p| = 2\pi n/\lambda_o \qquad (2.1.4)$$

$$|\mathbf{k}_a| = 2\pi/\lambda_a. \qquad (2.1.5)$$

From (2.1.1), $\theta = \pi/2$ for backscattered light and the shift in frequency, known as the Brillouin shift frequency, is given by

$$\nu_b = \nu_a = 2n\nu_a/\lambda_o. \qquad (2.1.6)$$

For fused silica, $\nu_a = 5.96.10^3$ ms^{-1} and n = 1.44 at $\lambda_o = 1.55\mu$m, giving ν_b = 11.1 GHz [1.2.3]. The presence of both the pump wave at an optical frequency of ν_o and the backscattered Stokes wave at $(\nu_o - \nu_b)$ gives rise to an intensity variation at the difference frequency of ν_b. Through electrostriction, this intensity variation leads to a corresponding density variation which reinforces the original acoustic wave at this frequency. The amplified acoustic wave produces an increased depth of refractive index modulation and a greater proportion of pump light is backscattered. In this way, the Stokes wave grows from a small intensity determined by thermal acoustic noise at the end of the fibre furthest from the input pump to a larger intensity at the pump end.

2.1.2 Brillouin Gain

The gain process may be examined quantitatively by means of the following coupled wave equations for the slowly varying complex envelopes of the optical electric field of the Stokes wave, E_s, and of the density variation of the acoustic wave, ρ, on the fibre core axis [1.2.3]:

$$dE_s/dz = -iK_2\rho^*E_p + \alpha E_s/2 \qquad (2.1.7)$$

$$d\rho^*/d\tau = -iK_1E_p^*E_s - \Gamma\rho^*, \qquad (2.1.8)$$

where z is the distance from the pump input end of the fibre, $\tau = t + z/v_g$ is time relative to a travelling Stokes wavefront, v_g is the optical group velocity, t is time, α is the intensity attenuation coefficient, Γ^{-1} is the acoustic phonon lifetime resulting in a spontaneous Brillouin scattering linewidth of $\Delta\nu_B = \Gamma/\pi$ (FWHM) and

$$K_1 = K_2\rho_0n^2\varepsilon_0/(2v_a) \qquad (2.1.9)$$

$$K_2 = \pi n^3p_{12}/(\lambda_o\rho_0), \qquad (2.1.10)$$

where p_{12} is the longitudinal elasto-optic coefficient, ρ_0 is the average density and ε_0 is the free space permittivity. For simplicity, the equivalent coupled wave equation for the pump field, E_p, is omitted here since it will initially be assumed that the Stokes wave intensity is always small enough compared to the pump intensity not to deplete the pump significantly. The pump field is therefore given by

$$E_p(z) = E_p(0)\exp(-\alpha z/2). \tag{2.1.11}$$

Thermal acoustic noise has not been included in (2.1.8) so as to illustrate how a Stokes wave seed inserted at $z = L$, where L is the fibre length, grows to a larger intensity at the pump end, $z = 0$. By setting $d\rho^*/d\tau = 0$ in (2.1.8) to determine the steady-state response, substituting ρ^* from (2.1.8) and $E_p(z)$ from (2.1.11) into (2.1.7) and integrating, the intensity gain for the Stokes wave may be obtained as

$$|E_s(0)|^2/|E_s(L)|^2 = \exp(GL_{eff} - \alpha L) \tag{2.1.12}$$

where L_{eff} is the effective length given by

$$L_{eff} = [1 - \exp(-\alpha L)]/\alpha \tag{2.1.13}$$

and G is given by

$$G = 2K_1K_2|E_p(0)|^2/(\pi\Delta\nu_B). \tag{2.1.14}$$

By using the relationship [1.2.3]

$$P_p/A_{eff} = n\varepsilon_0 c|E_p(0)|^2/2 \tag{2.1.15}$$

where P_p is the pump power launched into the fibre, A_{eff} is the effective mode cross-sectional area and c is the speed of light in vacuo, the Brillouin gain, G_B, may be expressed as

$$G_B = GL_{eff} = g_B P_p L_{eff}/A_{eff} \qquad (2.1.16)$$

where g_B is the Brillouin gain coefficient given by

$$g_B = 2\pi n^7 p_{12}^2/(c\lambda_o^2 \rho_0 v_a \Delta\nu_B). \qquad (2.1.17)$$

In fused silica, the spontaneous Brillouin scattering linewidth, $\Delta\nu_B$, is found to be 38.4 MHz at $\lambda_o = 1.0\ \mu m$ and varies as λ_o^{-2} [1.2.3], [2.1.1]. The following bulk parameters are also assumed for fused silica [1.2.3], [2.1.2], [2.1.3]: $\rho_0 = 2.21.10^3\ kg.m^{-3}$, $v_a = 5.96.10^3\ ms^{-1}$, $p_{12} = 0.286$ and at $\lambda_o = 1.55\ \mu m$, $n = 1.44$ and $\Delta\nu_B = 16$ MHz. g_B is then equal to $4.34.10^{-11}\ mW^{-1}$.

If the optical frequency of the Stokes wave is changed from $\nu_s = \nu_p - \nu_b$ to $\nu_s = \nu_p - \nu_b + f$, the frequency dependence of its intensity gain may be obtained by setting $E_s = E_{s1} \exp\{i\omega\tau\}$ and $\rho^* = \rho_1^* \exp\{i\omega\tau\}$, where $\omega = 2\pi f$ and E_{s1} and ρ_1^* are independent of τ, and solving (2.1.7) and (2.1.8) to give a frequency dependent version of (2.1.12) in which G{f} replaces G, where

$$G\{f\} = GR\{f\} \qquad (2.1.18)$$

and

$$R\{f\} = 1/(1 + (f/(\Delta\nu_B/2))^2) \qquad (2.1.19)$$

is the relative Brillouin gain spectrum, which is Lorentzian with a FWHM linewidth equal to that of the spontaneous Brillouin scattering spectrum, $\Delta\nu_B$.

The above analysis applies to the simple case where both the pump and Stokes waves have the same optical polarization. The more realistic situation in which this is not true is considered in a later section. The theory also applies strictly to a uniform fibre, in which the core is of pure silica and has no variations in density due to, for example, stresses induced by cabling. Practical single-mode fibres cannot usually be regarded as uniform for the purposes of predicting SBS performance, as discussed in chapters 4 and 5.

2.1.3 Brillouin Threshold

A very simple approximate formula for the input power at which the SBS backscattered power becomes significant compared to the pump power was developed by R.G. Smith [1.2.5] and this has been quoted by many authors [1.2.1], [1.2.3], [1.2.4], [1.2.6]-[1.2.9], [1.3.5], [1.3.9], [1.3.14], [2.1.4]-[2.1.7], usually in the form

$$\gamma G_B = 21 \qquad (2.1.20)$$

where γ is a polarisation factor between 0.5 and 1, often previously assumed to be 0.5 for low birefringence fibres when polarisation scrambling occurs, and G_B is the Brillouin gain defined in (2.1.16). Since this formula has been so widely used, it is interesting to examine its derivation so that its accuracy for typical optical links may be assessed and also its applicability to comparison with experimental characteristics of backscattered power as a function of input power for a monochromatic CW signal.

The starting point is a steady state differential equation, derived from (B1) of [1.2.5], for the photon occupation number, N_S, of the backward wave, assuming no depletion of the pump from SBS but only from linear attenuation:

$$[(d/dz) - \alpha_S]N_S = -gSp(z)(N_S + n_a) \qquad (2.1.21)$$

where α_s is the intensity attenuation coefficient at the Stokes frequency, g is the frequency dependent Brillouin gain coefficient given by $g_B R\{f\}$ from (2.1.17) and (2.1.19), $S_p(z)$ is the distance dependent pump intensity given by $P_p(z)/A_{eff}$ and $n_a = 1 + \langle n \rangle$, where $\langle n \rangle$ is the mean number of phonons per mode of the acoustic field and is given by [2.1.8]

$$\begin{aligned} \langle n \rangle &= (\exp(h\nu_a/k_B T) - 1)^{-1} \\ &\approx k_B T/h\nu_a \text{ for } k_B T >> h\nu_a \end{aligned} \qquad (2.1.22)$$

where k_B is Boltzmann's constant, T the temperature, h Planck's constant and ν_a the acoustic frequency given by (2.1.6). n_a represents the distributed thermal acoustic noise which initiates SBS in the absence of an injected Stokes signal. It is shown in chapter 3 and Appendix 3.1 that (2.1.21) may be derived from a set of partial differential equations which include a thermal noise term obtained from thermodynamic considerations in [2.1.8].

The optical power spectral density for the Stokes radiation at the pump end, $z = 0$, is given by $H_s\{f\} = h\nu_s N_s(z = 0)$ and, from (B5) of [1.2.5], is equal to

$$H_s\{f\} = h\nu_s n_a \int_0^L g S_p(0) \exp\left\{-(\alpha_s + \alpha_p)z + \frac{g S_p(0)}{\alpha_p}[1 - \exp(-\alpha_p z)]\right\} dz \qquad (2.1.23)$$

where α_P is the intensity attenuation coefficient at the pump frequency. This equation is used later for comparing simulated and theoretical backscattered power spectra.

In the derivation of the formula of (2.1.20), the assumption was made that the fibre length, L, is long compared to $1/\alpha$, where $\alpha = \alpha_P = \alpha_S$. If it is also assumed that $g_B S_p(0)/\alpha >> 1$, then from (B6) of [1.2.5],

$$H_s\{f\} = h\nu_s n_a \exp[gS_p(0)/\alpha]/[gS_p(0)/\alpha]. \qquad (2.1.24)$$

For $g_B S_p(0)/\alpha >> 1$, the effective noise bandwidth of this power spectrum is given approximately by (8) of [1.2.5]

$$B_{eff} = (\pi^{1/2}/2)\Delta\nu_B/[g_B S_p(0)/\alpha]^{1/2}. \qquad (2.1.25)$$

Smith employed an artificial definition for a threshold input pump power, P_{crit}", such that the total SBS backscattered power at the pump end, $P_s(z=0)$, is equal to the input power:

$$P_s(z=0) = H_s\{f=0\}B_{eff} = P_{crit}". \qquad (2.1.26)$$

This condition is unrealizable experimentally, since pump depletion ensures that the mean backscattered power is always less than the input power for a CW pump. By setting $G_{BT} = g_B P_{crit}"L_{eff}/A_{eff} = g_B S_p(0)/\alpha$, which is valid for the condition assumed above that $L >> 1/\alpha$, (2.1.26) becomes (17) of [1.2.5]

$$G_{BT}^{5/2}\exp(-G_{BT}) = K_T \qquad (2.1.27)$$

where

$$K_T = (\pi^{1/2}/2)(k_B T\nu_s/\nu_a)[g_B/\alpha A_{eff}]\Delta\nu_B. \qquad (2.1.28)$$

Smith assumed the following values at $\lambda_o = 1.06\ \mu m$ for the parameters in (2.1.28): $g_B = 3.10^{-11}$ m.W^{-1}, $\alpha = 5.10^{-3}$ m^{-1}, corresponding to ~20 dB/km, $A_{eff} = 10^{-11}$ m^2, $\Delta\nu_B = 50$ MHz, for which $K_T = 1.9.10^{-6}$ at room temperature. (2.1.27) then gives $G_{BT} = 21$, as stated in (19) of [1.2.5]. Taking more typical present values for a non-dispersion shifted fibre at $\lambda_o = 1.55\ \mu m$ [2.1.6], but deriving g_B and $\Delta\nu_B$ for fused silica as in [1.2.3]: $g_B = 4.34.10^{-11}$ m.W^{-1}, $\alpha = 4.14.10^{-5}$ m^{-1},

corresponding to 0.18 dB/km, $A_{eff} = 0.95.10^{-10}$ m^2, $\Delta\nu_B = 16$ MHz, for which $K_T = 1.1.10^{-5}$, a better approximation is $G_{BT} = 19$.

It is more useful to define a threshold input power, P_{cr}, such that the backscattered power, $P_s(z=0)$, reaches a fraction, r_{th}, of the input power:

$$P_s(z=0) = r_{th}P_{cr}. \qquad (2.1.29)$$

In this case, (2.1.27) should be replaced by

$$G_{BT}^{5/2}\exp(-G_{BT}) = K_T/r_{th}. \qquad (2.1.30)$$

r_{th} should be chosen to be small enough that pump depletion is not significant when $(P_s/P_p)(z=0) = r_{th}$, but large enough that the SBS backscattered power can be distinguished in the presence of Rayleigh backscattering from an experimental plot of total backscattered power as a function of input power. From simulated and experimental results presented in a later chapter, $r_{th} = 10^{-3}$ seems a reasonable choice. Based on the parameters given above for a non-dispersion shifted fibre at $\lambda_o = 1.55$ μm, the approximate equation $G_{BT} = 10.4$ should be used for $r_{th} = 10^{-3}$.

2.1.4 Effect of Signal Modulation on Brillouin Threshold

Lichtman et al. have shown that the relative Brillouin gain spectrum for a modulated signal, $R_m\{f\}$, is given by the convolution of the normalised input optical power spectrum, $p\{\nu\}$, with the relative Brillouin gain spectrum for a CW signal, $R\{f\}$, [2.1.7], [2.1.9] where

$$R_m\{f\} = \int p\{\nu\}R\{f - \nu\}\, d\nu \qquad (2.1.31)$$

where ν = frequency relative to input optical carrier frequency, ν_{pc}, f = frequency relative to nominal Stokes frequency, $\nu_{pc} - \nu_b$. They assume that the increase in threshold input power relative to that for an unmodulated carrier is equal to the reduction in peak Brillouin gain caused by modulation, where the modulated and unmodulated input signals have the same total power. This assumption represents a reasonable approximation, even though the value of G_{BT} determined by (2.1.27) or (2.1.30) and (2.1.28) shows a slight dependence on the Brillouin gain linewidth, which can increase significantly under modulation. By calculating the power spectra for ASK, PSK and FSK and assuming a Lorentzian Brillouin gain spectrum in the absence of modulation, they have obtained formulae for the corresponding modulated gain spectra as functions of the ratio of data rate to unmodulated Brillouin linewidth. The threshold increase, equal to the reduction in peak Brillouin gain, is then plotted as a function of this normalised data rate. The highest rate of increase in threshold with increasing data rate is given for PSK, since the carrier is completely suppressed. Measured and theoretical normalised peak gains have been compared by Bolle et al. for NRZ and CMI data formatted PSK modulation at data rates up to 150 Mbit/s [2.1.10]. Agreement between measurement and theory is good.

Sugie used the same technique to calculate threshold increase as a function of normalised data rate for CPFSK with modulation indices (peak-peak frequency deviation/data rate), m, between 0 and 1 [2.1.6]. The characteristic for m = 0.65 is very similar to that for PSK. Agreement between theoretical and experimental threshold increases at data rates up to 2.5 Gbit/s for m = 1 is fair.

If the power spectrum of a laser with linewidth, $\Delta\nu_L$, and the ideal unmodulated Brillouin gain spectrum with linewidth, $\Delta\nu_B$, are both assumed to be Lorentzian, the reduction in peak gain, and hence the increase in threshold, for CW operation of the laser is given by [2.1.5], [2.1.6]

$$g_B/g_{BL} = (\Delta\nu_B + \Delta\nu_L)/\Delta\nu_B. \qquad (2.1.32)$$

2.1.5 Brillouin gain spectrum for fused silica

Measurements by Pine of the Brillouin scattering spectrum for longitudinal acoustic waves in fused silica when pumped by CW light at a wavelength of 632.8 nm show that this does take the Lorentzian form predicted by theory [2.1.11]. Pine finds that the observed dependence of the Brillouin scattering linewidth on temperature, which features a pronounced peak at a temperature of about 130°K, is best explained using an anharmonic model in which scattering occurs between two acoustic modes with frequencies which differ by the Brillouin shift frequency, ν_b.

Heiman has shown that the Brillouin scattering linewidth measured for fused silica is proportional to ν_b^m, for 25 GHz < ν_b < 35 GHz, where m is about 2.7 [2.1.1]. This value of m is rather larger than expected, since both the anharmonic model favoured by Pine and an alternative known as the structural relaxation model predict that $m \leq 2$.

2.1.6 Influence of acoustic guidance and material considerations on Brillouin gain spectra of single mode fibres

Although the Brillouin gain spectrum of a single mode fibre when pumped by CW light is often assumed, for the purposes of simplified theory, to take the Lorentzian form given in (2.1.19), various effects modify its shape. Jen et al. have analysed the conditions under which a single mode fibre can guide acoustic as well as optical waves and the influence of guided acoustic longitudinal modes on SBS [2.1.12]-[2.1.15]. One important condition for acoustic guidance is that the longitudinal acoustic wave velocity be smaller in the core than in the cladding. This holds for the common case of a SMF with a GeO_2-doped silica core and pure silica cladding, but not for a SMF with a pure silica core and F-doped silica cladding.

Jen et al. have shown that for weakly guiding acoustic waveguides, in which the differences between the acoustic parameters (longitudinal and shear velocities and

density) of its core and infinitely thick cladding are small, the dispersion characteristics of acoustic phase velocity as a function of normalised acoustic frequency for the longitudinal modes may be predicted to a good approximation by solving the dispersion equation obtained under the ideal condition of equal shear velocities and densities for core and cladding [2.1.14]. Analysis of the coupling coefficients between the incident and SBS backscattered optical waves for the acoustic longitudinal modes indicates that only some of these coefficients are non zero [2.1.12],[2.1.13].

Shibata et al. have observed Brillouin gain spectra for SMFs with a GeO_2-doped silica core and pure silica cladding and found that these spectra each consist of a dominant lobe and two smaller lobes [2.1.16]-[2.1.18]. For the BSF of the peak of each lobe, the corresponding acoustic velocity can be calculated from (2.1.6). The equivalent velocity-frequency points lie close to the acoustic dispersion curves of phase velocity as a function of normalised frequency predicted for the three lowest order acoustic longitudinal modes of each SMF [2.1.17],[2.1.18]. The velocities and frequencies of the three peaks lie between those for the core and cladding materials. In the experiment of [2.1.18], the frequency spacing between the three Brillouin gain spectral peaks for a 9.0 mol.% GeO_2-doped core fibre measured at a wavelength of 1550 nm was found to be about 300 MHz and this spacing was evaluated as about 100 MHz for a commercially available SMF with a 3 mol.% GeO_2-doped core.

In contrast, the Brillouin gain spectrum for a SMF with a pure silica core and 2.2 mol.% F-doped silica cladding was found only to contain a main peak corresponding to the silica core and a much smaller peak at a reduced BSF whose value is predicted for the cladding material [2.1.18]. This is as expected, since the acoustic velocity of F-doped silica is less than that of pure silica, so that no guiding of longitudinal acoustic modes occurs.

The measured linewidth of the principal peak of the Brillouin gain spectrum for a SMF with a silica core and F-doped silica cladding is usually significantly larger than that predicted for bulk fused silica. For example, a linewidth of 48 MHz was observed for such a SMF at a wavelength of 1.55 μm in comparison to 16 MHz for bulk silica [2.1.17]. This was attributed to the refractive index profile variation of the SMF [2.1.17],[2.1.19]. Although a step change in refractive index may be desired between core and cladding with no variations within these regions, typical profiles are more gradual. Strictly speaking, the different BSFs for different parts of the core arise mainly from the variations in acoustic velocity corresponding to changes in dopant concentration rather than directly from the accompanying refractive index characteristic. Inconsistencies in dopant cross-sectional profile along the fibre length can give rise to Brillouin linewidth broadening as well [2.1.19],[2.1.20].

These mechanisms for linewidth broadening also apply to SMFs with a GeO_2-doped silica core and pure silica cladding [2.1.19],[2.1.20]. In addition, the phonon lifetime for each of the guided acoustic modes, particularly the subsidiary ones, may differ from that for bulk fused silica [2.1.17]. The doping associated with the more complex refractive index profile required for a dispersion-shifted fibre can give rise to another significant contribution to linewidth broadening [2.1.20].

2.2 COMPUTER MODELS

2.2.1 Required properties of a SBS model

Wherever possible, the model should take as input parameters the known physical and material constants which are unlikely to vary significantly between the optical fibres to be simulated. The model should be useful for predicting system performance based on a minimum of parameters which are measurable and hence specifiable for a fibre. These parameters should preferably be in use already and referred to widely in the literature. The following have been chosen for this model:

the peak gain and linewidth from the measured Brillouin gain spectrum, the effective core area, Brillouin shift frequency, refractive index of the core, fibre length and loss.

For a CW input, simulated characteristics of mean SBS backscattered power at the pump input and mean output signal power after transmission over the fibre length as functions of input power should be in good agreement with experimental characteristics, at least over a useful input power range. Over the lower part of this range, the modelled backscattered power should agree with that predicted for an undepleted pump using an integration of (2.1.23) over the frequency domain for an appropriate Brillouin gain spectrum.

The presence of BER floors observed experimentally in CPFSK and externally intensity modulated systems [1.3.1]-[1.3.5] under SBS conditions shows that the modelling of BER performance for digital systems and CNR performance for AM subcarrier multiplexed systems requires accurate simulation of SBS noise. A change in detected or demodulated signal-to-noise ratio of 1 dB at the decision point for a digital link can result in a corresponding change in BER of more than one order of magnitude. In AM CATV systems, great care is needed to minimise all potential sources of CNR degradation, such as interferometric intensity noise and laser relative intensity noise, and the upper bound of the CNR specification of 55 dB can be difficult to achieve, as apparent from the example in Appendix 1.1. A difference of 1 dB in CNR due to SBS can therefore be very significant. The power spectrum and time domain behaviour of the transmitted field should be simulated so that they can be inserted into an appropriate receiver model for BER or CNR prediction. The backscattered power spectra should be in agreement with those obtained for an undepleted pump using (2.1.23) at low input powers. Simulated system performance should agree with available experimental results.

2.2.2 SBS modelling techniques

Although many authors have used the simple approximate formula for the CW SBS threshold input power developed by R.G. Smith [1.2.5] whose derivation is discussed in section 2.1.3, neither his definition of the threshold nor his reliance on undepleted pump theory are very satisfactory. A better approach is to solve the two steady state differential equations for the pump and Stokes intensities in order to obtain characteristics of backscattered and fibre output powers as functions of CW input power. These characteristics would show the effects of pump depletion as well as linear loss. As pointed out by P. Bayvel and P.M. Radmore, the exact analytical solutions to the differential equations are only known for the special case of zero loss, so the authors have solved these numerically by means of the fourth order Runge-Kutta algorithm [2.2.1]. The boundary condition for the Stokes input noise intensity was calculated either by using the approximation that the spontaneous Stokes noise within the Brillouin bandwidth is equal to the injection of one photon per mode [1.2.5] or from scattering theory [2.2.2]. From the characteristics obtained in this way, the threshold input power, defined as that at which the ratio of backscattered intensity to pump input intensity reaches 1%, could be determined for different values of fibre loss. The principles outlined in section 2.1.4 were then used to calculate the factor by which this threshold would increase for a finite laser linewidth and for signal modulation.

In order to simulate the dynamic behaviour of the transmitted field as well as the backscattered field, it is necessary to solve numerically the three partial differential equations for the pump, Stokes and density wave amplitudes for the desired input optical field as a function of time [2.1.8], [2.2.3]-[2.2.6].

Many examples of such modelling have used the artificial device of a deterministic Stokes seed, inserted at the opposite end of the model fibre or Brillouin medium from the pump. In some cases, this seed has taken the form of a constant amplitude

at the nominal Stokes frequency [2.2.5]-[2.2.7]. Höök and Bolle have made the seed appear more like the Stokes wave generated by spontaneous Brillouin scattering by using a constant amplitude, randomly phase modulated envelope [2.2.3]. In other cases, a constant amplitude seed with randomly distributed phase has been injected at regular intervals along the simulated fibre length in order to represent more realistically the distributed nature of spontaneous Brillouin scattering [2.2.8], [2.2.9]. If the average waveform of a periodic transmitted signal is required, but without the need to model SBS noise originating from the amplification of thermal acoustic noise, the use of a constant amplitude seed may yield an approximate solution. However, noise simulation is important for the proposed model and it is shown below that the optical power spectrum of the transmitted field would not be well represented by applying a Stokes seed rather than distributed thermal acoustic noise.

If a Stokes seed of any kind is used, effort is required to ensure that its magnitude is appropriate for modelling spontaneous Brillouin scattering which is distributed over the length of the fibre. Although the correct magnitude can be evaluated for a given CW input power and a given set of fibre parameters, this would, in principle, need to be recalculated for a different input power. This has been demonstrated by Boyd in fig. 2 of [2.1.8], where characteristics of normalised backscattered power (SBS reflectivity) as a function of normalised input power (single-pass Brillouin gain) have been plotted for two cases: "localised source (undepleted pump)" and "distributed fluctuating source (undepleted pump)". The first case corresponds to the injection of a Stokes seed and the intensity gain is equivalent to that given by (2.1.12), while the second case is equivalent to the assumption of distributed thermal acoustic noise given by the differential equation of (2.1.21). The shapes of the two characteristics are significantly different, particularly at low input powers.

For some examples of modulated signals, the input power may fluctuate very significantly, even when averaged over the effective length of the fibre. More

flexibility is therefore afforded by including distributed thermal acoustic noise in the model than by using a Stokes seed calculated for a particular average input power.

It is shown in chapter 3 and Appendix 3.2 that a minimum limit for the transmitted SBS noise spectral density may be evaluated by considering the dynamic pump depletion arising from the product of the Stokes field and the locally generated thermal acoustic noise at each fibre length element. In other words, this component of transmitted SBS noise originates from interaction between the stimulated backscattered optical field and the spontaneous part of the density variation. Simulations described in chapter 3 have indicated that the transmitted SBS noise spectrum is dominated by this Stokes-spontaneous density depletion noise for long model fibre lengths. In order to simulate transmitted SBS noise, it is therefore necessary to model not only the Stokes field, which might otherwise have been generated approximately from a suitable seed, but also the thermal acoustic noise within each length element. Only transmitted SBS noise arising from the product of the stimulated backscattered optical field and the stimulated part of the density variation can be modelled if the Stokes seed is the only source of spontaneous Brillouin scattering.

Another reason for using a distributed acoustic noise model is that the simulated power spectrum of the Stokes field should be sufficiently well represented that the computed transmitted SBS noise power spectrum can be relied on at the relative optical frequencies required for system performance evaluation. For example, in the modelling of an AM-VSB CATV link described in chapter 5, the transmitted SBS noise power spectrum needs to be characterised for frequencies relative to that of the optical carrier of up to 70 MHz. The power spectrum of the Stokes field up to similar relative frequencies is then also required. The simulated Brillouin gain for a Stokes input frequency of 70 MHz relative to the nominal Stokes frequency is found to be about 0.2 of the peak value. The approximation reported by R.G. Smith that distributed thermal acoustic noise may be represented using a Stokes seed equivalent to a single photon is stated to be valid only for Brillouin gains much

greater than unity [1.2.5]. This approximation cannot be relied on for the range of frequency dependent Brillouin gains featured in the CATV example. The use of the distributed acoustic noise model allows the Stokes power spectrum to be simulated without this source of inaccuracy.

The effect of fibre nonuniformity on the peak Brillouin gain, and hence on SBS threshold, has been analysed by Mao et al. [2.1.4]. They have calculated the reduction in peak gain from concatenating a number of fibre lengths, each with a different measured Brillouin shift frequency, and found this to correspond with the experimentally determined increase in SBS threshold. However, in all the reported examples of numerical modelling of the SBS PDEs seen so far, the BSF is assumed to be constant over the length of the fibre. The phonon decay rate is increased from the value expected for bulk silica to one which corresponds to the measured Brillouin gain linewidth for the fibre. By adopting this procedure, the Brillouin gain spectrum is assumed to be Lorentzian. As discussed in sections 2.1.6 and 4.1, variations in dopant concentration over the core-cladding cross-section and other effects give rise to Brillouin gain spectra for SMFs which differ significantly from a Lorentzian form, particularly for gains below half of the maximum.

Although it is found in chapter 4 that differences in Brillouin gain spectra below half-maximum have no observable effect either on total transmitted power or on total backscattered power, except, in the latter case, at input powers well below threshold, they do influence the backscattered power spectrum outside the FWHM Brillouin gain linewidth and also the transmitted power spectrum at frequencies beyond half of the Brillouin gain linewidth relative to the optical carrier frequency. In chapter 5, this effect on the transmitted power spectrum is shown to modify the carrier-to-noise ratio contribution from SBS noise for an optical intensity modulated subcarrier representative of that in an AM-VSB CATV link. The development of Boyd's SBS model to include variations in BSF over the model fibre length, as described in chapter 4, therefore appears to both novel and useful.

2.2.3 Examples

Höök and Bolle have simulated the effect of SBS on the intensity waveforms of a PSK transmission system at data rates between 1 and 100 Mbit/s [2.2.3], [2.2.7], [2.2.10]. Agreement with experimental waveforms has been found to be quite good [2.2.10], [2.2.11]. The three SBS partial differential equations for the amplitudes of the pump and Stokes fields and the density variation have been derived from optical and density wave equations [2.2.3]. Although the authors have studied the average depletion of the transmitted modulated signals, they pay little attention to the characterisation of noise induced on these signals by SBS which would be essential for modelling sensitivity penalties and BER floors for a transmission link.

Instead of using a theoretical value for the Brillouin gain coefficient, g_B, for fused silica and a theoretical polarisation factor, γ, as given in (2.1.20), the Brillouin gain has been measured and a corresponding experimental value of g_B derived. This takes into account both the reduction in peak gain associated with fibre nonuniformity and the average coupling between the polarisations of pump and Stokes waves. The experimental g_B would be $4.34.\ 10^{-11}$ m.W^{-1} for fused silica and a uniform fibre with $\gamma = 1$. For a section of fibre with a measured Brillouin linewidth of 36 MHz at 1.52 μm, compared to a theoretical linewidth of 16 MHz at this wavelength, their experimental g_B was $2.2.\ 10^{-11}$ m.W^{-1}, which they comment on as seeming a factor of 2 too high, even though they accepted it for the simulations. They may have based this comment on the expectation that γ would be 1/2 for a typical fibre with complete polarisation scrambling between pump and Stokes waves [1.2.3] and that the broadened Brillouin gain spectrum would be Lorentzian, corresponding to a simple change in the phonon decay time, Γ, in (2.1.8). On this basis, g_B would be $0.5.(16/36).4.34.\ 10^{-11}$ m.W^{-1} = $0.96.\ 10^{-11}$ m.W^{-1}. As will be explained later, γ is expected to be 2/3 for a low birefringence fibre and could be higher, while, for the mechanism to be proposed for the simulation of fibre nonuniformity, the reduction in peak gain is not predicted to be

as large as for a Lorentzian spectrum. Their experimental g_B of 2.2. 10^{-11} m.W^{-1} is therefore not surprising.

In a second experiment [2.2.3], [2.2.11], they concatenated 3 spliced fibre segments with slightly shifted gain curves, giving a total length of 19.8 km and an overall effective linewidth of 47 MHz, the gain maximum being the same as above (2.2. 10^{-11} m.W^{-1}). An externally phase modulated PSK signal was applied to this fibre and the transmitted output intensity waveforms studied for various modulating data patterns. This system was simulated by numerically solving the three SBS PDEs they had derived for a uniform fibre, with the appropriate constants in these equations chosen to give a peak gain coefficient equal to their measured value and a phonon decay time constant, Γ, determined by the total measured linewidth of 47 MHz. It would have been more realistic to have simulated the changes in Brillouin shift frequency over the length of the fibre, and to have assumed a value of Γ applicable to a short section of fibre. As described in chapter 4, this approach is used to model nonuniform fibre.

The three PDEs were solved as a coupled system of ordinary differential equations along the characteristic curves corresponding to the three velocities: the forward optical group velocity for the pump field amplitude propagation equation, the reverse optical group velocity for the Stokes field amplitude propagation equation and the acoustic velocity for the density wave propagation equation. Since the acoustic velocity is very much smaller than the optical group velocity, it is assumed to be zero for the purpose of solution along the characteristics. These characteristics are divided into intervals resulting in a normalised distance-time plane or mesh. For their simulated data rate of 100 Mbit/s with a bit period of 10 ns, they assumed a π-radian phase shift duration of 2 ns and found that at least 6 distance mesh points were required for the length of fibre traversed in this time. Consequently, the maximum distance they could simulate for a practical processing time was 420 m, rather than the real fibre length of 19.8 km. The end-to-end loss and Brillouin gain for the model fibre were made the same as for the real fibre, so that the attenuation

and Brillouin gain coefficients were multiplied by the length shortening factor of about 50. This distance scaling procedure is shown later to be valid for obtaining some important simulated statistical and spectral data and is used in the proposed model.

Höök and Bolle have simulated spontaneous Brillouin scattering in their model by means of an injected Stokes seed field which is randomly phase modulated such that its power spectrum is Lorentzian with a FWHM linewidth of 100 MHz. This linewidth was simply chosen to be large enough compared to the simulated Brillouin gain linewidth of 47 MHz that spectral components were present over a relevant part of the spectrum. The amplitude of the Stokes seed field was chosen to match one point on the simulated characteristic of SBS depleted output power as a function of input power to the same point on the experimental characteristic. As discussed above, this procedure will not result in a modelled output power - input power characteristic which is consistent with the theory for distributed thermal acoustic noise.

Boyd et al. have developed a model for the dynamic behaviour of SBS which includes an appropriate description of thermal acoustic noise [2.1.8]. This model applies to any SBS medium, but does not include the effects of loss. The simulation technique, theory and numerically obtained results are nevertheless of great interest for the modelling of SBS in optical fibres. The authors have derived the three SBS partial differential equations for the amplitudes of the pump and Stokes fields and the density variation, which have the same form as those derived by Höök and Bolle except that they have also included in the density equation a noise source that describes the thermal excitation of acoustic waves. The pdf (probability density function) of this random variable, which is a function of time and distance, is assumed to be Gaussian and its acf (autocorrelation function) proportional to a product of delta functions in time and distance, giving uniform temporal and spatial power spectral densities. An expression for the magnitude of the acf has been obtained by considering the energy of a sound wave in a volume element of the

Brillouin medium and this is proportional to absolute temperature. A theoretical relationship for the SBS reflectivity, the ratio of backscattered power to pump power, is derived for the artificial case of a pump undepleted by SBS or attenuation. This equation is equivalent to the result of integrating (2.1.23) over the frequency domain for $\alpha = 0$.

By numerically integrating the three SBS PDEs for different input powers and ratios of medium transit time to phonon decay time, $\Gamma_i T_t$, characteristics of SBS reflectivity, normalised standard deviation (nsd) of the Stokes intensity and Stokes power spectral linewidth as functions of Brillouin gain for different $\Gamma_i T_t$ have been obtained. While SBS reflectivity characteristics are found to be only slightly sensitive to $\Gamma_i T_t$, the Stokes intensity nsd and spectral linewidth depend significantly on $\Gamma_i T_t$ for gains above threshold.

Boyd's model for a thermal acoustic noise source has been adopted for the proposed model. The minimal dependence of the SBS reflectivity on $\Gamma_i T_t$, and hence on the model fibre length, validates Höök and Bolle's technique of fibre length scaling, at least for the determination of mean power characteristics for a CW input. The known dependence of the Stokes nsd and spectrum on $\Gamma_i T_t$ is a useful starting point in assessing how large the model fibre length needs to be to obtain simulated backscattered and transmitted power spectra which are representative of those for real fibre lengths that are too long to be simulated.

Gaeta and Boyd have obtained experimental results that are in good agreement with a version of Boyd's model which has been extended to include fibre loss [2.2.4]. They found that about 70% of the total output Stokes light was contained in the polarisation direction parallel to that of the incident laser and concluded that a polarisation factor of 0.7 was required in the expression for the Brillouin gain. The experimental characteristic of Stokes linewidth as a function of Brillouin gain was then found to be in very good agreement with the simulated characteristic. Experimental normalised correlation functions and a characteristic of Stokes nsd as a

function of gain also corresponded well with simulated equivalents when the polarisation factor was taken into account. They argue that the larger the value of $\Gamma_i T_t$, the less rapid is the rate of decrease in Stokes nsd for increasing gain above threshold. For $\Gamma_i T_t = 450$, this decrease is found experimentally and numerically at a gain of 80 to be only about 10% compared to the nsd for gains below threshold.

2.2.4 Conclusions

A model is needed to simulate the effects of SBS on transmission system performance in terms of Bit Error Rate for digital systems and Carrier-to-Noise Ratio or Signal-to-Noise Ratio in analogue systems. Although corresponding experimental studies have been carried out, no comparison of simulated and experimental performance degradations have, to our knowledge, been reported. Instead, various subsidiary effects such as intensity waveform degradation for PSK transmission and the dynamics of the backscattered field have been simulated and compared with experimental results. The spectral and statistical properties of the noise induced on the transmitted signal by SBS do not appear to have been simulated previously.

SBS modelling has often relied on the use of an injected Stokes seed. This technique has been shown to be inaccurate for situations in which large temporal variations in input power can be expected. More importantly, it is found in chapter 3 that a significant component of transmitted SBS noise originates from interaction between the stimulated backscattered optical field and the spontaneous part of the density variation. Only transmitted SBS noise arising from the product of the stimulated backscattered optical field and the stimulated part of the density variation can be modelled if the Stokes seed is the only source of spontaneous Brillouin scattering. In addition, the optical power spectrum of the Stokes field can become distorted if a Stokes seed is used, particularly for low values of frequency dependent Brillouin gain, and this would lead to inaccuracy in the transmitted noise spectrum. The inclusion of a distributed thermal acoustic noise description within the dynamic

model is therefore essential, even though this can add substantially to the processing time. The basis of such a model has been developed and experimentally confirmed by Boyd, Gaeta et al. for the backscattered field. They did not extend their study to the transmitted field. The technique used by Höök and Bolle of simulating a fibre as a much shorter model fibre length with the same end-to-end loss and Brillouin gain has been validated, subject to conditions, by some results of Boyd and Gaeta and is adopted for the model to be described in chapter 3.

Previous dynamic SBS models have assumed the Brillouin shift frequency to be constant over the fibre length and hence the Brillouin gain spectrum to be Lorentzian. This assumption is justifiable for the simulation of total backscattered and transmitted powers and for modelling the distortion of periodic transmitted signal waveforms, but can lead to inaccuracy when simulating transmitted SBS noise spectra. An important example of this is described in chapter 5 for the modelling of the carrier-to-noise ratio contribution from SBS noise for an optical intensity modulated subcarrier representative of that in an AM-VSB CATV link. The development of Boyd's SBS model to include variations in BSF over the model fibre length, as described in chapter 4, therefore appears to both novel and useful.

3. MODELLING OF STIMULATED BRILLOUIN SCATTERING FOR A UNIFORM FIBRE

Most of the available theory for SBS makes use of the assumption that the material or materials of the medium are homogeneous and that the relevant parameters such as density and cross-sectional dimensions are constant, so that the Brillouin shift frequency (BSF) may also be regarded as invariant over the medium. In this chapter, a numerical model based on this uniform medium theory is developed, partly as a starting point for deriving a new nonuniform model which includes BSF variations along the light path and which will be described in chapter 4. In addition, it is useful to compare simulated SBS characteristics obtained from the two models.

In section 3.1, the existing theory for a uniform fibre model of SBS is described, assuming linearly polarised light. In section 3.2, the theory is extended to include the effects of polarisation properties associated with typical communication optical fibres which have a low, but variable, birefringence. In section 3.3, the SBS partial differential equations are approximated to as difference equations along the characteristic lines for the three propagating waves. From these, an appropriate computational algorithm is derived as the basis for a programme for simulating statistics and optical power spectra for the transmitted and SBS backscattered fields. In section 3.4, the numerical model is verified for various simplified test conditions by comparing simulated results with theory and with published simulated results. In section 3.5, a strategy for simulating optical links which are too long to model directly is described whereby results from suitably defined shorter model fibres are used to predict performance for the real optical link.

In section 3.6, simulated characteristics of optical transmitted and backscattered powers as functions of input power for a CW optical input carrier are compared with those for a published experiment. These simulated characteristics are found to be very similar to each other for a wide range of model fibre lengths, confirming the

usefulness of the scaling strategy. Transmitted and backscattered power spectra for different input powers and model fibre lengths are also shown and discussed, together with statistical characteristics. A new method of simulating the component of the transmitted SBS noise power spectrum which does not vary significantly with model fibre length is discussed and examples of these noise spectra are compared with the full simulated transmitted power spectra.

3.1 THEORETICAL DESCRIPTION OF SBS

When thermal acoustic noise is ignored, the equations for the slowly varying complex amplitudes of the pump, Stokes and density waves may be written as [2.2.3]:

$$\begin{aligned}
&[\partial/\partial\tau + \partial/\partial\zeta]E_{1n} = -E_{2n}Q - \alpha_n E_{1n} \\
&[\partial/\partial\tau - \partial/\partial\zeta]E_{2n} = E_{1n}Q^* - \alpha_n E_{2n} \\
&[\partial/\partial\tau + \delta]Q = \gamma_n E_{1n}E_{2n}^*,
\end{aligned} \tag{3.1.1}$$

where

$$\begin{aligned}
&E_{1n} = -ir_1E_{1u}, \qquad E_{2n} = -ir_2E_{2u}, \qquad Q = -ir_aA, \\
&\zeta = z/L, \qquad \tau = t/(L/v_g), \quad \delta = \Gamma_B L/v_g, \quad \alpha_n = \alpha L/2,
\end{aligned} \tag{3.1.2}$$

in which $r_1 = r_2 = |E_{1u}(z = 0,t = 0)|^{-1}$ and $r_a = (\omega^2 L/4kc_0^2).(\partial\varepsilon_r/\partial\rho)$, E_{1n}, E_{2n} and Q are normalised pump, Stokes and density wave amplitudes and E_{1u}, E_{2u} and A are the corresponding amplitudes given in (6) of [2.2.3] before normalisation, ζ and τ are normalised variables for distance, z, and time, t, L is the fibre length, α is the power attenuation coefficient per unit distance, v_g is the optical group velocity, ω is the optical angular frequency, k is the approximate magnitude of the pump and Stokes wave vectors given by (2.1.4), c_0 is the speed of light in vacuo, ε_r is the relative permittivity of the fibre core, ρ is its density, Γ_B is the phonon amplitude

decay rate, equal to $\pi\Delta\nu_B$, where $\Delta\nu_B$ is the theoretical Brillouin gain linewidth and γ_n is given by

$$\gamma_n = \rho_0\varepsilon_0(\partial\varepsilon_r/\partial\rho)^2.(\omega^2/16kc_0^2).(L^2k_a/v_gv_a).|E_{1u}(z = 0,t = 0)|^2 \qquad (3.1.3)$$

where ρ_0 is the average density of the fibre core, ε_0 is the free space permittivity and k_a is the magnitude of the density wave vector given by (2.1.5). The normalised versions of the fibre length, the time of flight through the fibre and the input intensity, $|E_{1n}(\zeta = 0)|^2$, are all equal to unity.

By deriving the steady state equation for the Stokes intensity from (3.1.1) in the absence of pump depletion from SBS, and by obtaining an equivalent expression to that of (2.1.12), Höök and Bolle have related their normalised parameters, δ and γ_n, to those of (2.1.16) by equation (14) of [2.2.3]:

$$\gamma_n = g_BP_p\delta L/2A_{eff}. \qquad (3.1.4)$$

If the expressions for P_p/A_{eff} from (2.1.15) with $|E_p(0)|^2 = |E_{1u}(z = 0,t = 0)|^2$ and g_B from (2.1.17) with p_{12} given by [3.1.1]

$$p_{12} = \rho_0(\partial\varepsilon_r/\partial\rho).(1/n^4) \qquad (3.1.5)$$

are substituted in (3.1.4), the equation for γ_n in (3.1.3) is obtained.

Thermal acoustic noise has been taken into account in equations (5a), (5b) and (9) of [2.1.8] by Boyd et al., which are otherwise equivalent to (3.1.1). The amplitude of the Langevin force for this thermal noise, f_{thn}, appears in (9) and may be included in the density wave equation of (3.1.1) by adding to the RHS the term f_{nthn}, where

$$f_{nthn} = -iK_9.f_{thn}, \qquad (3.1.6a)$$

$$K_9 = r_a.(L/v_g). \qquad (3.1.6b)$$

In accordance with the analysis of [2.1.8], f_{thn} is a Gaussian random variable with zero mean and is δ-correlated such that

$$<f_{thn}(z,t)f_{thn}^{*}(z',t')> = Q_{thn}\,\delta(z-z')\delta(t-t') \qquad (3.1.7)$$

where

$$Q_{thn} = 2k_B T\rho_0\Gamma_i/(v_a^2 A_{eff}), \qquad (3.1.8)$$

in which Γ_i is the phonon intensity decay rate, equal to $2\Gamma_B = 2\pi\Delta\nu_B$. By expressing $(\partial\varepsilon_r/\partial\rho)^2$ in terms of g_B using (2.1.17) and (3.1.5), f_{nthn} may be similarly defined with

$$\begin{aligned} <f_{nthn}(\zeta,\tau)f_{nthn}^{*}(\zeta',\tau')> &= Q_{nthn}\,\delta(\zeta-\zeta')\delta(\tau-\tau') \qquad (3.1.9)\\ &= K_9^2.Q_{thn}\,\delta(z-z')\delta(t-t') \end{aligned}$$

where

$$\begin{aligned} Q_{nthn} &= K_9^2.Q_{thn}.(v_g/L^2)\\ &= \delta^2.(g_B c^2 k_B T/(2n^2 v_a A_{eff})). \qquad (3.1.10) \end{aligned}$$

It is shown in Appendix 3.1 that the partial differential equations of (3.1.1) with the thermal noise term f_{nthn} added to the RHS of (3.1.1c) may be used to derive the steady state differential equation for the photon occupation number of the SBS backscattered field envelope quoted by R.G. Smith in (B1) of [1.2.5] and given in (2.1.21).

3.2 THEORETICAL POLARISATION PROPERTIES OF SBS

Stolen has provided a polarisation model for SBS in linear birefringence fibres, also known as polarisation-maintaining fibres, in which the optical phase difference between waves in the fast and slow principal axes can be assumed to increase linearly with distance along the fibre [3.2.1]. In an experiment on a linear-birefringence fibre, he found that the SBS gain for a Stokes wave injected into one principal axis was insignificant if the pump wave was launched in the orthogonal principal axis. When the pump polarisation was changed to 45° relative to both principal axes, the SBS gain was found to be substantial and independent of the polarisation of the Stokes wave. He and other authors [1.2.1], [1.2.3], [1.3.5], [2.1.5] have interpreted from this that in low-birefringence fibres, in which random variations in polarisation are expected, the net effect is that half of the pump power is coupled with an injected Stokes wave regardless of its polarisation, so that $\gamma = 0.5$ in (2.1.20). Since most typical single mode fibres used in communication systems are nominally of low birefringence, whether the dispersion-zero-wavelength is 1.3μm (standard) or 1.55μm (dispersion shifted), this case is of greater practical interest than that of linear-birefringence fibres.

Deventer and Boot have investigated theoretically and experimentally the polarisation properties of SBS in a representative single mode fibre [3.2.2]. They argue that the state of polarisation (SOP) of the Stokes wave is always related to that of the pump wave by considering SBS as the reflection of the pump from the travelling acoustic wave. At an optical reflection, the rotation of the polarisation is changed from clockwise to anticlockwise and vice-versa, but the orientation and ellipticity of the polarisation ellipse remains the same [3.2.3]. They also justify the assumption that, for a low-birefringence fibre, the SOP is uniformly distributed over the Poincaré sphere [3.2.4]. The mixing efficiencies of identically and orthogonally polarised pump and Stokes waves are then derived as, respectively [3.2.2]:

$$\eta_i = 2/3$$

$$\eta_o = 1/3. \qquad (3.2.1)$$

The expression for the intensity gain of an injected Stokes wave in the absence of pump depletion given in (2.1.12) for an idealised fibre with no birefringence and identical linear pump and Stokes polarisations may be modified for the case of a low-birefringence fibre by multiplying the term $G_B = GL_{eff} = g_B P_p L_{eff}/A_{eff}$ by η, where η is given by (3.2.1). The polarisation-sensitive Brillouin gain, $G_{BP} = \eta G_B$, is therefore expected to vary by a factor of two as the SOP of the injected Stokes wave is changed. The gain variation between 10% and 20% observed in [3.2.5] is in agreement with this theory. If components of the Stokes wave exist in both the identical and orthogonal states, SBS gain occurs for each component independently of the other, in the absence of pump depletion. If pump depletion occurs, this reduces the SBS gain for each component equally.

When the SBS backscattered power arises only from thermal acoustic noise, rather than an injected Stokes wave, the amplified power for each component or polarisation mode is very approximately proportional to $\exp(G_{BP})$ when $G_{BP} >> 1$, where G_{BP} is the Brillouin gain for that mode. For $\eta_i G_B >> 1$, $\exp(\eta_i G_B) >> \exp(\eta_o G_B)$, since $\eta_i = 2\eta_o$, and the power in the dominant mode far exceeds that in the subsidiary mode. It is shown experimentally in [3.2.2] that at pump powers high enough for pump depletion to be observable, the SBS backscattered power in the subsidiary mode is more than 25 dB lower than that in the dominant mode. For the purpose of simulating the mean transmitted power for a CW input, it is therefore reasonable to model only the dominant mode.

Since the average proportion of pump power coupled to one of the Stokes polarisation modes is η, where η is either η_i or η_o, the average proportion of pump field coupled to the Stokes field for that mode is $(\eta)^{1/2}$. For electrostriction, the interaction takes place between a field and a density variation with the same orientation. Density waves are considered to exist in the same polarisation modes as

the Stokes waves. Therefore the average proportion of pump field coupled to the density amplitude for the mode selected above is also $(\eta)^{1/2}$. For this mode, the equations of (3.1.1), together with the thermal noise term, f_{nthn}, of (3.1.6), should be modified to

$$[\partial/\partial\tau + \partial/\partial\zeta]E_{1n} = -(\eta)^{1/2}E_{2n}Q - \alpha_n E_{1n} \qquad (3.2.2a)$$

$$[\partial/\partial\tau - \partial/\partial\zeta]E_{2n} = (\eta)^{1/2}E_{1n}Q^* - \alpha_n E_{2n} \qquad (3.2.2b)$$

$$[\partial/\partial\tau + \delta]Q = (\eta)^{1/2}\gamma_n E_{1n}E_{2n}^* + f_{nthn}. \qquad (3.2.2c)$$

Multiplying (3.2.2c) by $(\eta)^{1/2}$ and letting $Q_P = (\eta)^{1/2}Q$, $\gamma_{nP} = \eta\gamma_n$, and $f_{nthnP} = (\eta)^{1/2}f_{nthn}$, (3.2.2) becomes

$$[\partial/\partial\tau + \partial/\partial\zeta]E_{1n} = -E_{2n}Q_P - \alpha_n E_{1n} \qquad (3.2.3a)$$

$$[\partial/\partial\tau - \partial/\partial\zeta]E_{2n} = E_{1n}Q_P^* - \alpha_n E_{2n} \qquad (3.2.3b)$$

$$[\partial/\partial\tau + \delta]Q_P = \gamma_{nP}E_{1n}E_{2n}^* + f_{nthnP}. \qquad (3.2.3c)$$

Setting the time derivatives equal to zero for the steady state case, $f_{nthnP} = 0$, $2\gamma_{nP}/\delta = 2\eta\gamma_n/\delta = \eta g_B P_p L/A_{eff}$ (from (3.1.4)) and applying the normalisation equations of (3.1.2) yield the steady state differential equations given in (8) of [3.2.2]:

$$dP_1/dz = -\eta(g_B/A_{eff})P_1P_2 - \alpha P_1 \qquad (3.2.4a)$$

$$dP_2/dz = -\eta(g_B/A_{eff})P_1P_2 + \alpha P_2 \qquad (3.2.4b)$$

where P_1 and P_2 are the pump and Stokes powers as functions of distance.

In order to simulate SBS taking into account the thermal acoustic noise present in both polarisation modes, the PDEs of (3.2.3) may effectively be solved alternately between the two modes over small intervals of distance and time by adopting the following procedure:

(i) All three of the PDEs of (3.2.3) are simultaneously solved for the dominant mode with $\gamma_{nP} = \eta_i \gamma_n$, yielding new values of E_{1n}, E_{2nd} and Q_{Pd}, where E_{2nd} and Q_{Pd} are the dominant mode components of E_{2n} and Q_P.

(ii) Since E_{1n} is determined primarily by the dominant mode solution of (i), the new value of E_{1n} is used to solve (3.2.3b) and (3.2.3c) for the subsidiary mode with $\gamma_{nP} = \eta_o \gamma_n$, yielding new values of E_{2ns} and Q_{Ps}, where E_{2ns} and Q_{Ps} are the subsidiary mode components of E_{2n} and Q_P.

(iii) E_{1n} is adjusted for the depletion from the subsidiary mode using (3.2.3a) and the new values of E_{2ns} and Q_{Ps}. This depletion is not likely to affect significantly the mean transmitted power for a CW input, but does alter the transmitted power spectrum appreciably.

3.3 NUMERICAL SOLUTION OF SBS PARTIAL DIFFERENTIAL EQUATIONS

The three partial differential equations of (3.2.3) are numerically solved for the points in the normalised distance - time plane, (ζ,τ), corresponding to intersections of equally spaced lines with the three characteristic normalised velocities, +1, -1, 0, of the pump, Stokes and density waves, respectively, as shown in fig. 3.1.

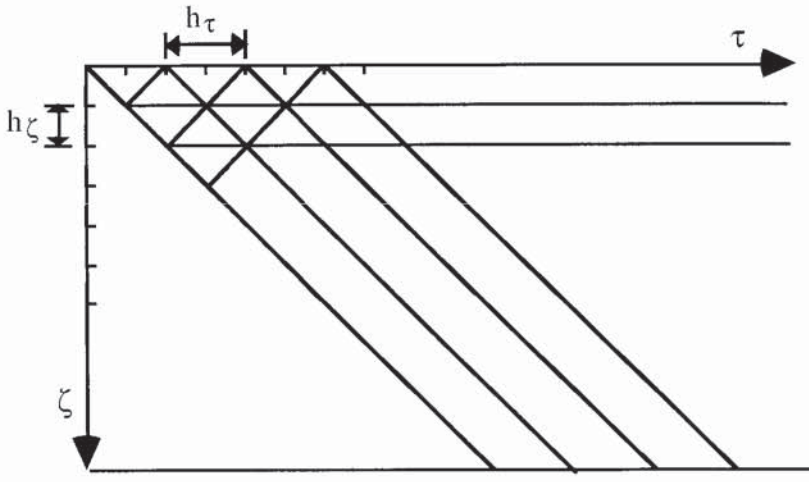

Fig. 3.1: Characteristic lines for propagation of the pump, Stokes and density waves in the (ζ,τ) plane

The number of distance intervals over the model fibre length is N_ζ, giving a normalised distance interval of $h_\zeta = 1/N_\zeta$. The interval between successive mesh point values of τ is then $h_\tau = 2h_\zeta = 2/N_\zeta$. For the purposes of allocating these mesh points to a two dimensional array format for computation, it is convenient to transpose the (ζ,τ) plane to the (ζ,τ'') plane, as shown in fig. 3.2, where

$$\tau'' = \tau - \zeta. \qquad (3.3.1)$$

The interval between successive mesh point values of τ'' is then $h_{\tau''} = h_\tau = 2h_\zeta = 2/N_\zeta$.

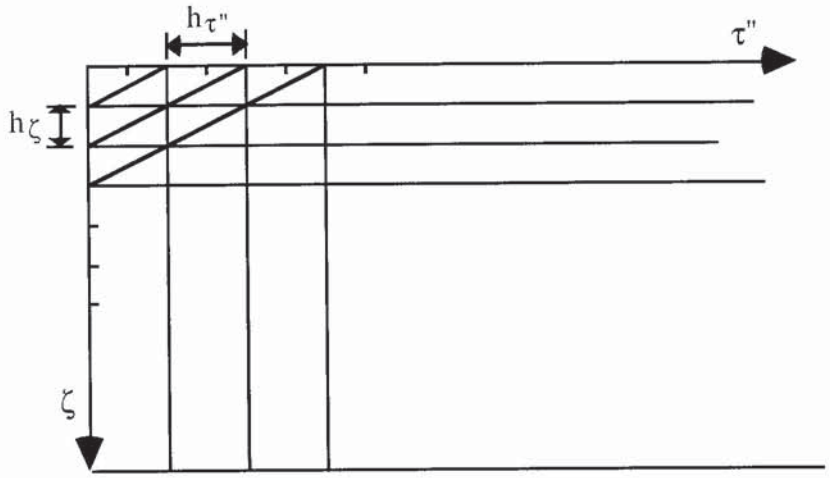

Fig. 3.2: Characteristic lines for propagation of the pump, Stokes and density waves in the (ζ,τ'') plane

(3.2.3) may be rewritten in terms of ζ and τ'' as

$$[\partial/\partial\zeta]\, E_{1n} = -E_{2n}Q_P - \alpha_n E_{1n} \qquad (3.3.2a)$$

$$[2\partial/\partial\tau'' - \partial/\partial\zeta]\, E_{2n} = E_{1n}Q_P^* - \alpha_n E_{2n} \qquad (3.3.2b)$$

$$[\partial/\partial\tau'' + \delta]\, Q_P = \gamma_{nP}E_{1n}E_{2n}^* + f_{nthnP}. \qquad (3.3.2c)$$

These PDEs are equivalent to the following ordinary differential equations (ODEs) along their characteristics:

$$[d/d\zeta]E_{1n} = -E_{2n}Q_P - \alpha_n E_{1n} \qquad \text{for } d\tau''/d\zeta = 0$$

$$[-d/d\zeta]E_{2n} = E_{1n}Q_P^* - \alpha_n E_{2n} \qquad \text{for } d\zeta/d\tau'' = -1/2$$

$$[d/d\tau'' + \delta]Q_P = \gamma_{nP}E_{1n}E_{2n}^* + f_{nthnP} \qquad \text{for } d\zeta/d\tau'' = 0. \qquad (3.3.3)$$

All of these ODEs are of the general form

$$[d/dt + T^{-1}]x = f(t), \qquad (3.3.4)$$

for which the result of integrating from $t_m = m\Delta t$ to t_{m+1}, where Δt is a small interval of t and m is an integer, can be expressed as [3.3.1]

$$x_{m+1} = x_m \exp\{-\Delta t/T\} + \int \exp\{-(t_{m+1} - t')/T\} f(t')\, dt', \qquad (3.3.5)$$

where $x_m = x(m\Delta t)$. If f(t') is assumed to vary linearly with time between t_m and t_{m+1}, the integral can be evaluated to give [3.3.1]

$$x_{m+1} = Cx_m + Af_m + Bf_{m+1} + O((\Delta t)^3), \qquad (3.3.6)$$

where $f_m = f(m\Delta t)$ and

$$C = \exp\{-\Delta t/T\},$$
$$A = T[(T/\Delta t)(1 - \exp\{-\Delta t/T\}) - \exp\{-\Delta t/T\}],$$
$$B = T[1 - (T/\Delta t)(1 - \exp\{-\Delta t/T\})]. \qquad (3.3.7)$$

The assumption of linear variation over a distance or time step for the product term corresponding to f(t) in each of the three ODEs of (3.3.3) is justified provided that the changes in amplitude and phase of the three envelopes over the step can be considered small. The main strategies used were firstly to ensure that the sampling frequency was sufficiently high compared to the most significant parts of the backscattered or transmitted power spectra and secondly to obtain convergence of

these spectra or other output data as the step size was decreased while other parameters, such as model fibre length, were kept constant. No phase or frequency modulation was applied to the input pump carrier for any of the simulations in this work. However, the variations in Brillouin shift frequency applied in the nonuniform fibre model give rise to phase shifts in the appropriate product terms over the steps. The necessity to limit these is discussed in section 4.4. Since the variation in the product terms over the steps is not linear under all anticipated conditions for either the uniform or the nonuniform fibre model, it may well be that other numerical solution methods such as fourth order Runge-Kutta would be more efficient than that assumed here.

The ODEs of (3.3.3) are, thus, approximated by the following difference equations:

$$[E_{1n}]_{m+1}^{j+1} = C_e[E_{1n}]_{m+1}^{j} + A_e[-E_{2n}Q_P]_{m+1}^{j} + B_e[-E_{2n}Q_P]_{m+1}^{j+1} \tag{3.3.8a}$$

$$[E_{2n}]_{m+1}^{j+1} = C_e[E_{2n}]_{m}^{j+2} + A_e[E_{1n}Q_P^*]_{m}^{j+2} + B_e[E_{1n}Q_P^*]_{m+1}^{j+1} \tag{3.3.8b}$$

$$[Q_P]_{m+1}^{j+1} = C_q[Q_P]_{m}^{j+1} + A_q[\gamma_{nP}E_{1n}E_{2n}^*]_{m}^{j+1} + B_q[\gamma_{nP}E_{1n}E_{2n}^*]_{m+1}^{j+1} + (A_q + B_q)[f_{nthnP}]_{m}^{j+1} \tag{3.3.8c}$$

where $[x]_m^j = x(\tau''_m, \zeta_j) = x(m\Delta\tau'', j\Delta\zeta)$, $\Delta\tau'' = h_{\tau''} = 2h\zeta$, $\Delta\zeta = h\zeta$ and

$$\begin{aligned}
C_e &= \exp\{-\alpha_n h\zeta\},\\
A_e &= (1/\alpha_n)[(1/\alpha_n h\zeta)(1 - \exp\{-\alpha_n h\zeta\}) - \exp\{-\alpha_n h\zeta\}],\\
B_e &= (1/\alpha_n)[1 - (1/\alpha_n h\zeta)(1 - \exp\{-\alpha_n h\zeta\})],\\
C_q &= \exp\{-\delta h_{\tau''}\},\\
A_q &= (1/\delta)[(1/\delta h_{\tau''})(1 - \exp\{-\delta h_{\tau''}\}) - \exp\{-\delta h_{\tau''}\}],\\
B_q &= (1/\delta)[1 - (1/\delta h_{\tau''})(1 - \exp\{-\delta h_{\tau''}\})],
\end{aligned} \tag{3.3.9}$$

and $[f_{nthnP}]_m^{j+1}$ is an equivalent value of f_{nthnP} over the rectangle in the τ'',ζ plane given by $mh_{\tau''} \le \tau'' < (m+1)h_{\tau''}$ and $(j+1/2)h\zeta \le \zeta < (j+3/2)h\zeta$, such that [2.1.8]

$$\langle([f_{nthnP}]_m^j)([f_{nthnP}]_{m'}^{j'})^*\rangle = (\eta Q_{nthn}/(h\tau''.h\zeta))\delta_{mm'}\delta_{jj'}. \qquad (3.3.10)$$

The thermal acoustic noise samples, $[f_{nthnP}]_m^j$, are generated by means of functions for producing pseudorandom variables with a Gaussian probability density function (pdf) and a uniform power spectral density [3.3.2]. These functions are based on the use of the Wichmann-Hill algorithm to generate variables uniformly distributed between 0 and 1 with a pseudorandom period of 7.10^{12} [3.3.3] and the Box-Muller transformation to convert the uniform pdf to a Gaussian pdf [3.3.2], [3.3.4].

The intrinsic difference equations of (3.3.8) can be solved simultaneously with greater ease by first rewriting them as

$$\begin{aligned} E_{1\nu} &= C_e[E_{1n}]_{m+1}^j + A_e e_{1k\nu} + B_e(-E_{2\nu}Q_\nu) \\ &= E_{1k\nu} + B_e(-E_{2\nu}Q_\nu) \qquad (3.3.11a) \\ E_{2\nu} &= C_e[E_{2n}]_m^{j+2} + A_e e_{2k\nu} + B_e(E_{1\nu}Q_\nu^*) \\ &= E_{2k\nu} + B_e(E_{1\nu}Q_\nu^*) \qquad (3.3.11b) \\ Q_\nu &= C_q[Q_P]_m^{j+1} + A_q[\gamma_{nP}E_{1n}E_{2n}^*]_m^{j+1} + B_q[\gamma_{nP}E_{1n}E_{2n}^*]_{m+1}^{j+1} + \\ &(A_q + B_q)[f_{nthnP}]_m^{j+1} \\ &= Q_{k\nu} + B_q\gamma_{nP}(E_{1\nu}E_{2\nu}^*) \qquad (3.3.11c) \end{aligned}$$

where $E_{1\nu}$, $E_{2\nu}$ and Q_ν are the unknown values at (m+1, j+1) to be determined, $E_{1k\nu}$, $E_{2k\nu}$ and $Q_{k\nu}$ are the expressions in known values of the variables required to evaluate $E_{1\nu}$, $E_{2\nu}$ and Q_ν, respectively and

$$\begin{aligned} e_{1k\nu} &= [-E_{2n}Q_P]_{m+1}^j \\ e_{2k\nu} &= [E_{1n}Q_P^*]_m^{j+2}. \qquad (3.3.12) \end{aligned}$$

An approximate solution to (3.3.11) is obtained by means of the coefficients M_1 and M_2, which are functions of first order estimates, E_{1e} and E_{2e}, of $E_{1\nu}$ and $E_{2\nu}$, respectively, and is given by

$$E_{1\nu} = [1 + B_e^2 M_1 M_2 (Q_{k\nu} Q_{k\nu}^*)]^{-1} \{M_2 E_{1k\nu} + B_e M_1 M_2 (-E_{2k\nu} Q_{k\nu})\} \quad (3.3.13a)$$

$$E_{2\nu} = M_1 \{E_{2k\nu} + B_e (E_{1\nu} Q_{k\nu}^*)\} \quad (3.3.13b)$$

$$Q_\nu = Q_{k\nu} + B_q \gamma_{nP} (E_{1\nu} E_{2\nu}^*) \quad (3.3.13c)$$

where

$$M_1 = [1 - b(E_{1e} E_{1e}^*)]^{-1}$$

$$M_2 = [1 + b(E_{2e} E_{2e}^*)]^{-1}$$

$$b = B_e B_q \gamma_{nP}$$

$$E_{1e} = E_{1k\nu} + B_e (e_{1k\nu})$$

$$E_{2e} = E_{2k\nu} + B_e (e_{2k\nu}). \quad (3.3.14)$$

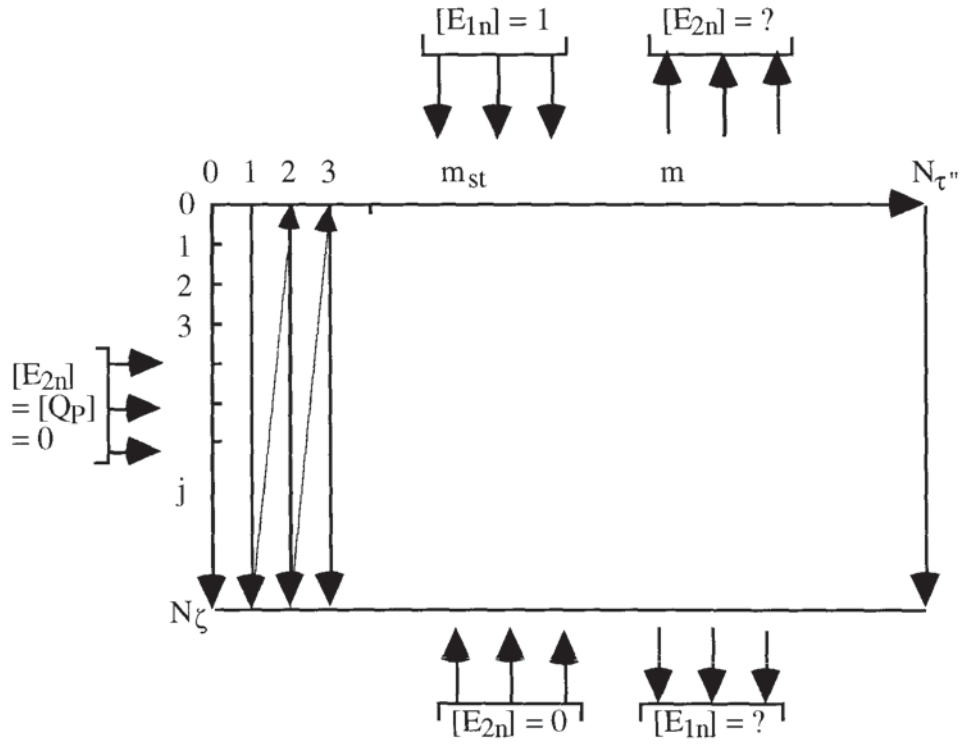

Fig. 3.3: Boundary conditions and computation sequence for numerical solution

The computation of the values of $[E_{1n}]$, $[E_{2n}]$ and $[Q_P]$, as illustrated in fig. 3.3, proceeds by assuming the following initial conditions:

$[E_{2n}]_{m=0}^{j}$ and $[Q_P]_{m=0}^{j} = 0$ for $0 \leq j \leq N\zeta$,

$[E_{2n}]_m^{j=N\zeta} = 0$ for all m, except when a test Stokes seed is injected,

$[E_{1n}]_m^{j=0} = 1$ for all m, when the pump input is CW. (3.3.15)

$[E_{1n}]_{m=0}^{j}$ is then computed for $0 < j \leq N\zeta$, using (3.3.13a). $[E_{1n}]$, $[E_{2n}]$ and $[Q_P]$ are determined using (3.3.13) for m = 1, starting at j = 0 and finishing at $j = N\zeta$. This process is repeated for values of m up to $N_{\tau''} = (N_{mft}/2).N\zeta$, where N_{mft} is the number of model fibre transit times to be simulated. The computed values of $[E_{2n}]_m^{j=0}$ and $[E_{1n}]_m^{j=N\zeta}$ are stored in an array for subsequent processing and represent the backscattered field at the pump end and the transmitted field at the opposite end, respectively. The mean powers are calculated by multiplying the specified pump input power by the average of the squares of these normalised field samples, starting from $m = m_{st} = (N_{mftst}/2).N\zeta$, where N_{mftst} is the number of model fibre transit times allowed for transient settling. $N_{mftst} = 20$ is found to be adequate for the cases simulated for a CW pump.

The power spectra are estimated using the Discrete Fourier Transform (DFT), obtained using a Fast Fourier Transform (FFT) algorithm, of the complex field samples after transient settling, multiplied by a Hanning window (raised cosine) function [3.3.5]. Without the application of the Hanning window, the abrupt changes of field in the time domain between the two ends of the sequence of samples would give rise to frequency components in the DFT which would be unrepresentative of a much longer sequence. The power spectral density at each frequency is obtained from the sum of the squares of the real and imaginary components of the DFT at this frequency. A bandwidth averaged power spectrum is then derived by arranging the original spectral lines into non-overlapping groups of n_{SL} lines with a group noise bandwidth of B_N, and calculating the average spectral density in each group. The main reason for doing this is to reduce the standard deviation, for a given number of simulation runs with different pseudorandom thermal acoustic noise sample sequences, of the spectral density at each displayed

frequency and hence provide a smoother spectrum [3.3.5]. Another important benefit is that the output spectral data file generated by the programme is reduced.

3.4 VERIFICATION OF NUMERICAL MODEL

3.4.1 Comparison of simulated results with theory

Various tests have been carried out on the model described above with an injected Stokes seed and the thermal acoustic noise parameter, $[f_{nthnP}]_m^j$, set to zero. For the first set of these, a simplified programme is used in which the term $-E_{2n}Q_P$ in (3.3.3) associated with depletion of the pump by SBS is eliminated. The steady state gain of the Stokes field (ssgsf) is found to be in good agreement with (2.1.12) for various values of Brillouin gain, G_B, attenuation, α_n and normalised acoustic wave decay rate, δ. In table 3.1, the simulated ssgsf is shown as a function of the number of distance steps, $N\zeta$, in comparison to the theoretical value, for $G_B = 20$, $\alpha_n = \log_e(10)/2$ and $\delta = 100$. The simulated ssgsf converges on the theoretical value with increasing $N\zeta$. Even at $N\zeta = 200$, the error in ssgsf is only 0.65%, which corresponds to an intensity gain error of less than 0.06 dB. With the Stokes seed equal to zero, the acoustic amplitude, Q_P, falls exponentially with normalised time, τ'', from an initial value as expected.

$N\zeta$	ssgsf
200	7010.34
400	6976.58
800	6968.18
theory	6965.38

Table 3.1: Simulated steady state gain for Stokes field (ssgsf) as a function of the number of distance steps, $N\zeta$, compared to theoretical value, for $G_B = 20$, $\alpha_n = \log_e(10)/2$ and $\delta = 100$.

The programme which includes pump depletion has been tested for an injected Stokes seed by confirming that the simulated steady state pump and Stokes

intensities, $I_P(z)$ and $I_S(z)$ respectively, satisfy the following equation which has been derived from (3.2.4):

$$[\log_e\{I_S(z_2)I_P(z_2)\} - \log_e\{I_S(z_1)I_P(z_1)\}] = (\eta g_B/\alpha)[\{I_P(z_2) - I_S(z_2)\} - \{I_P(z_1) - I_S(z_1)\}]. \qquad (3.4.1)$$

An important discrepancy with the commonly cited theoretical description given by Agrawal [1.2.1] is noted here. A comparison was initially made with Agrawal's theoretical characteristics of pump and Stokes relative intensities as functions of normalised distance for $g_B I_P(0)L = 10$, $\alpha L = 0.1$, and a Stokes seed intensity relative to the input pump intensity of 0.01 as shown in fig. 9.2 of [1.2.1]. These characteristics were derived from equations (9.2.7) to (9.2.10) of [1.2.1], which he introduces with reference to [3.4.1]. The steady state intensity equations solved by Enns and Batra in [3.4.1] apply to a forward scattering mechanism such as Stimulated Raman Scattering. It would therefore appear that Agrawal has erroneously attempted to adapt the solution of Enns and Batra for the backward scattering mechanism of SBS. Significant differences were observed between the simulated steady state intensities and the corresponding values predicted by Agrawal. The modelled Stokes relative intensity at the pump end was 0.647 compared to his figure of 0.684, and the modelled pump relative intensity at the opposite end was 0.310 compared to his figure of 0.296. It was then found that his characteristics did not satisfy (3.4.1), whereas those simulated did. Differentiation of Agrawal's (9.2.7) and (9.2.8) yield $dI_P/dz = -g_B I_S I_P - \alpha I_P$, as expected, but $dI_S/dz = -g_B I_S I_P - \alpha I_S$, instead of the correct expression, $-g_B I_S I_P + \alpha I_S$, given in his (9.2.1). His solutions of (9.2.7) to (9.2.10) are therefore accurate for $\alpha = 0$, but not for other values of α. A comparison between simulated and theoretical characteristics for $\alpha = 0$, based on these solutions, gives excellent agreement. For $G_B = 10$ and an output Stokes intensity of 0.6 of the input pump intensity, the agreement between simulated and theoretical intensities is better than 0.02% or 0.001 dB for $N_\zeta = 200$.

A comparison between theory and simulations which include distributed thermal acoustic noise rather than a constant envelope injected Stokes seed is given and discussed in the context of an experimental example in section 3.6.

3.4.2 Comparison with published simulated data

The computer model has been tested by reproducing representative simulation results reported by Boyd et al. for the example of SBS in CS_2 [2.1.8]. In (3.3.3), the parameters α_n, δ and γ_{nP} were set by the relations:

$$\alpha_n = 0 \qquad \delta = \Gamma_i T_t/2 \qquad \gamma_{nP} = G_{sp}\delta/2 \tag{3.4.2}$$

where $\Gamma_i T_t$ is the product of the phonon intensity decay rate, Γ_i, and the transit time, T_t, through the medium and G_{sp} is the Brillouin gain, referred to in [2.1.8] as the single-pass gain. The strength of the thermal acoustic noise parameter, ηQ_{nthn}, in (3.3.10) is determined in accordance with the conditions stated in [2.1.8].

$N\zeta$	N_{mft}	$N_{\tau''}$	$\lvert E_{2n}\rvert^2$	nsd
200	350	35,000	0.1169 0.1189 0.1144 0.1167 av: 0.1167	0.8038 0.7494 0.7869 0.7874 av: 0.7819
400	350	70,000	0.1166 0.1191 av: 0.1179	0.8509 0.7969 av: 0.8239
800 [2.1.8]	-	-	0.11 to 0.12	0.8

Table 3.2: Simulated values of mean normalised Stokes intensity, $|E_{2n}|^2$, and normalised standard deviation (nsd) of the Stokes intensity at $G_{sp} = 30$ and $\Gamma_i T_t = 20$ in comparison to equivalent values reported in ref. [2.1.8]

The simulated mean normalised Stokes intensity, $|E_{2n}|^2$, equal to the SBS reflectivity, R, referred to in [2.1.8], is in excellent agreement with the "distributed fluctuating source (numerical integration)" curve in fig. 3 of [2.1.8] at the two values of G_{sp} investigated, 30 and 60. The normalised standard deviation (nsd) of the Stokes intensity simulated at $G_{sp} = 30$ and $\Gamma_i T_t = 20$ also agrees well with the appropriate curve in fig. 5 of [2.1.8]. Simulated values of $|E_{2n}|^2$ and nsd at $G_{sp} = 30$ and $\Gamma_i T_t = 20$ are shown in table 3.2 in comparison to equivalent values reported in [2.1.8], together with the number of distance steps per model fibre length, N_ζ, the number of model fibre transit times per simulation run, N_{mft}, and the number of time steps per model fibre length, N_τ".

3.5 DISTANCE SCALING FOR EFFICIENT SIMULATION OF TYPICAL LINKS

The simulation of SBS in an optical link using the three dynamic SBS PDEs requires a minimum sampling frequency for the power spectra to be modelled with a sufficiently high bandwidth. For modulated pump signals, this sampling frequency is typically determined by the modulation type and data rate or modulation bandwidth, as, for example, for the 100 Mbit/s PSK simulations of Höök and Bolle [2.2.3] discussed in 2.2.3. Even for a CW pump, the sampling frequency should preferably be at least ten times the Brillouin gain linewidth so that the gain is small at the Nyquist frequency compared to the peak gain.

Given that the sampling interval, Δt, is determined by the minimum sampling frequency, the distance interval, $\Delta z = v_g \Delta t/2$, is also fixed. The simulated fibre length, L_{mf}, is therefore proportional to the number of distance intervals, N_ζ. A certain number of fibre transit times, say 20, should also be allowed for transients to settle. The transit time is also proportional to N_ζ. The programme execution time is approximately proportional to $N_\zeta N_\tau$", where $N_\tau" = [(N_{mft}/2).N_\zeta]$ is the number of time intervals for N_{mft} transit times. So the execution time depends on N_ζ^2 and

hence on L_{mf}^2. It is found that the simulation of model fibre lengths greater than about 1km rapidly becomes prohibitive. For typical link lengths of 10 to 100 km, a distance scaling technique is required such that behaviour can be predicted from the simulation of a scaled down model fibre length.

By multiplying the steady state differential equation for SBS growth from thermal acoustic noise in the absence of pump depletion, (2.1.21), by the fibre length L, the parameters z, α_S and g in (2.1.21) may be replaced by their normalised equivalents, $\zeta = z/L$, $\alpha_{SL} = \alpha_S L$ and $g_L = gL$. The backscattered power spectral density given by (2.1.23) is then seen to be independent of L for constant $\alpha_S L$ and gL. Under these conditions, the steady state pump and Stokes differential equations of (3.2.4) are also independent of L.

The following scaling strategy is therefore used as an initial basis for predicting SBS performance for fibres too long to simulate directly:

$$L_m = s_F L_t \qquad \alpha_m = \alpha_t / s_F \qquad g_{Bm} = g_{Bt} / s_F \tag{3.5.1}$$

where s_F is a suitable scale factor, L_m, α_m and g_{Bm} are the model fibre values of L, α and g_B for insertion into (3.1.2), (3.1.4) and (3.1.10), while L_t, α_t and g_{Bt} are the corresponding true fibre values.

The simulations of normalised standard deviation and linewidth of the Stokes output intensity as functions of Brillouin gain shown in figs. 5 and 6 of [2.1.8] reveal no dependence on the normalised medium length, $\Gamma_i T_t$, at gains low enough for pump depletion to be negligible. However, at higher gains for which pump depletion is significant, these parameters vary appreciably with length. In contrast, the normalised average Stokes output intensity is not found to depend sensitively on length. It is therefore appropriate to predict the power spectra of the backscattered and transmitted fields for the true fibre length, L_t, by simulating these spectra for increasing values of the model fibre length, L_m, and observing the trends.

3.6 COMPARISON WITH EXPERIMENTAL RESULTS

The input parameters for the uniform fibre model are chosen to match the conditions of an experiment by van Deventer and Boot, in which mean optical output and backscattered powers were characterised as functions of input power for a CW input signal in fig. 3 of [3.2.2]. This experiment was chosen because the important parameters are stated, enabling a comparison with the model to be made without the need to infer values or perform simulations for a likely range of values for any of the parameters, except for a single fitting factor, the Brillouin gain coefficient. For example, the Brillouin gain linewidth is not measured for all reported SBS experiments, but in this case, the measured value is given, together with a tolerance. For most reported SBS experiments, no measurements are made to indicate or confirm the value of the polarisation factor, whereas in this case, the theoretical prediction is confirmed by observation. For one experiment in which the Brillouin gain linewidth is measured, the overall link loss is stated to be greater than the fibre loss by as much as 1.7 dB, with little indication as to what proportion of this is at the fibre input end [2.1.6]. In the chosen paper, this excess loss is as little as 0.3 dB [3.2.2].

One unsatisfactory aspect of the paper by van Deventer and Boot is that they have compared their measured SBS characteristics with theoretical curves derived from "an exact solution" of the two steady state differential equations for the pump and Stokes powers given in a paper by Enns and Batra [3.4.1]. As discussed in section 3.4.1, the equations solved by Enns and Batra apply to a forward scattering mechanism such as Stimulated Raman Scattering. Their analytical solution is therefore not applicable to SBS in the presence of loss. It is not surprising that the experimental backscattered power characteristic of van Deventer and Boot does not fit their theoretical curve as well as the modelled curves for the UFM and NFM to be described below.

In the experiment by van Deventer and Boot [3.2.2], a 1.537 μm distributed Bragg-reflector laser with a linewidth of 2 MHz was coupled via an Erbium doped fibre amplifier and other components into a 12.7 km long single mode fibre, with an attenuation of 0.19 dB/km, a mode field diameter of 10.3 μm, an effective core area of 83 μm^2, a Brillouin shift frequency of 10.88 GHz and a Brillouin gain linewidth of 40 $\pm$ 3 MHz. From fig. 3(b) of [3.2.2], it is found that the total linear loss between the measured input and output powers is 2.7 dB, of which 2.4 dB is from fibre attenuation and the remaining 0.3 dB is assumed to be between the fibre output and the output power measurement point. (This additional loss of 0.3 dB is taken into account in the comparison of simulated and experimental transmitted power characteristics (shown in fig. 3.7 b) on p. 68 and discussed there), but not in other graphs showing simulated transmitted power or power spectral density for different model fibre lengths.)

The parameters for the uniform fibre model are chosen to agree with these experimental values wherever possible. Instead of simulating the phase noise on the input signal to give a linewidth of 2 MHz as for the laser, an unmodulated input carrier is modelled and the phonon amplitude decay rate, Γ_B, in (3.1.2), where $\Gamma_B = \pi\Delta\nu_B$, is increased such that $\Delta\nu_B$ = 42 MHz, rather than 40 MHz. The value of the Brillouin gain coefficient, g_B, is chosen to give the best fit between the simulated and experimental characteristics of backscattered power as a function of input power shown in fig. 3.7 a) and is equal to $1.943.10^{-11}$ $m.W^{-1}$. The dominant and subsidiary polarisation modes are assumed to have polarisation factors of $\eta_i = 2/3$ and $\eta_o = 1/3$, respectively, as predicted by theory and discussed in section 3.2. The refractive index of the fibre core is assumed to be 1.44 at 1.537 μm, as for bulk fused silica [1.2.3]. Although the core is probably GeO_2 doped and the cladding of pure silica, the small increase in the index of about 0.004 from doping is likely to be approximately offset by the decrease from waveguiding. For the measured Brillouin shift frequency of 10.88 GHz, the value of acoustic velocity for the model is obtained from (2.1.6) as $5.81.10^3$ $m.s^{-1}$.

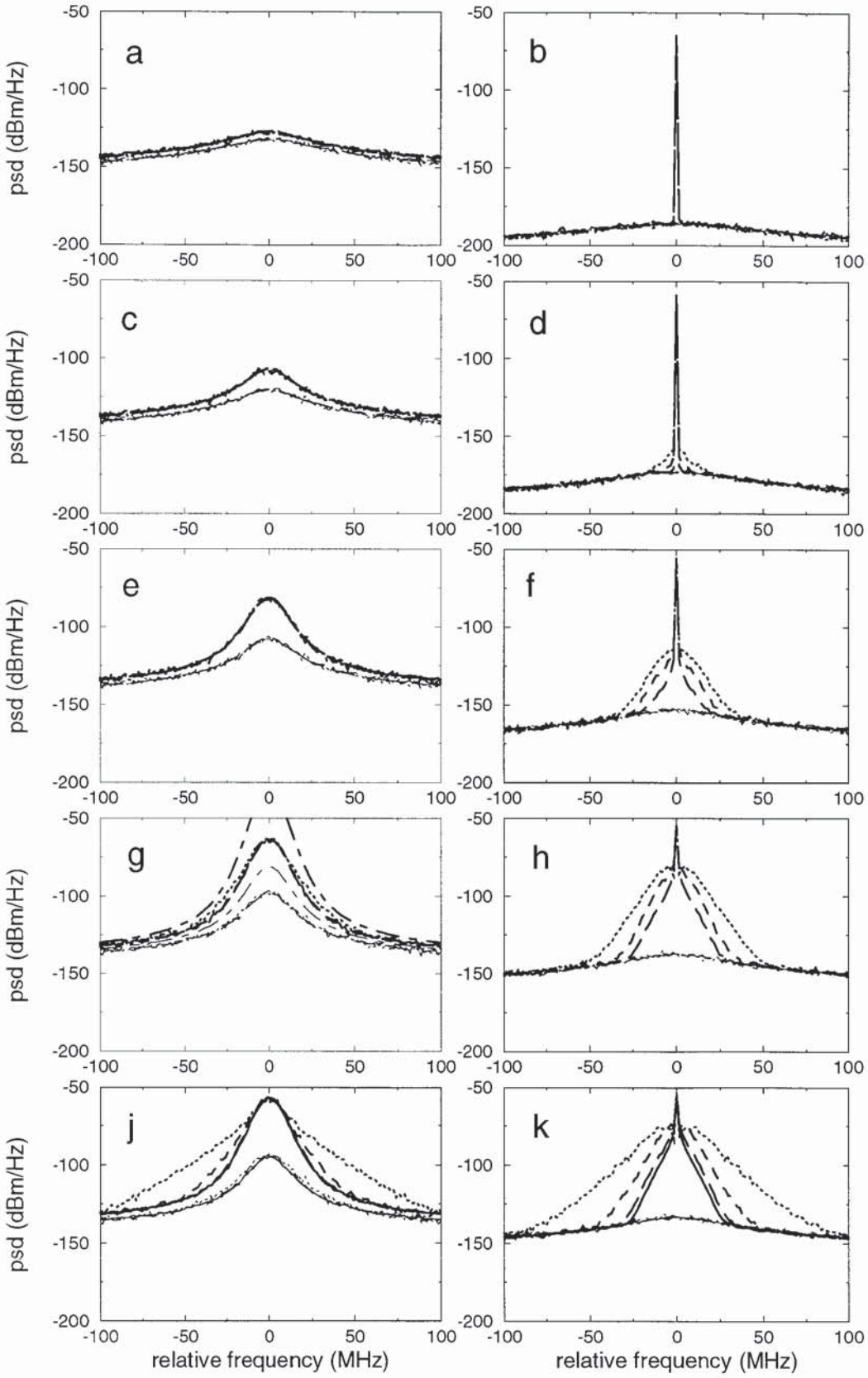

Fig. 3.4: Simulated SBS backscattered power spectra (left) for dominant (bold) and subsidiary (normal) polarisation modes and transmitted power spectra (right, bold) with corresponding inferred noise spectra (right, normal) for CW input powers of 0 dBm (a, b), 6 dBm (c, d), 9 dBm (e, f), 12 dBm (g, h), 15 dBm (j, k). Model fibre lengths of 31 m (dotted), 124 m (dashed), 496 m (long dashed) and, for 15 dBm only, 991 m (solid) have been simulated. Theoretical SBS backscattered power spectra assuming no pump depletion from SBS (dot-dashed) are shown for all powers except 15 dBm. Each power spectral density (psd) is determined as the average in a bandwidth of 1.6 MHz. A uniform fibre model has been assumed with a Brillouin linewidth of 42 MHz and a SBS gain coefficient of $1.943.\ 10^{-11}$ $m.W^{-1}$. The fibre loss is equivalent to that for 12.7 km at 0.19 dB/km.

If the sampling frequency, f_S, is given by $k_R\Delta\nu_B$, the model fibre length, L_m, can be expressed as

$$L_m = N\zeta(v_g\Delta t/2) = N\zeta v_g/(2k_R\Delta\nu_B). \qquad (3.6.1)$$

Also, the product of phonon intensity decay rate and transit time, $\Gamma_i T_t$, referred to in the simulations of [2.1.8], is given by

$$\Gamma_i T_t = 2\pi\Delta\nu_B L_m/v_g = \pi N\zeta/k_R. \qquad (3.6.2)$$

For $N\zeta = 500$ and $k_R = 10$, $\Gamma_i T_t = 157$. From [2.1.8], the simulated SBS backscattered power spectrum at high pump powers for this value of $\Gamma_i T_t$ is expected to be much closer to that for the experimental fibre length of 12.7 km than that for $\Gamma_i T_t = 20$ described in [2.1.8] would be. For these values of $N\zeta$ and k_R, (3.6.1) yields $L_m = 124$ m for $\Delta\nu_B = 42$ MHz and for $v_g = c/n$, where n =1.44. From the simulated SBS backscattered power spectra shown in fig. 3.4 for input powers of 0 to 15 dBm and model fibre lengths, L_m, of 31 to 991 m, it is clear that these spectra at $L_m = 124$ m are indistinguishable from those at higher L_m for input powers up to 12 dBm and considerably closer to convergence than for $L_m = 31$ m at 15 dBm. The agreement of the modelled spectra with those obtained by numerical integration of the theoretical equation for the SBS backscattered power spectral density, (2.1.23), based on the assumption of an undepleted pump, is excellent at all the selected values of L_m for input powers up to 9 dBm. At 12 dBm, the modelled spectra for both polarisation modes are seen to be substantially smaller than the corresponding theoretical ones due to pump depletion.

At high input powers, the divergence of the SBS backscattered spectra at low values of L_m from the convergent spectra attained for sufficiently high L_m is accompanied by a change in the normalised standard deviation (nsd) of the instantaneous SBS backscattered power from unity, as shown in fig. 3.5. The nsd is defined as the standard deviation of a random variable divided by the mean of the variable. For the

dominant polarisation mode, the nsd is reduced from unity under these conditions, as also observed in [2.1.8] from their simulations for a single polarisation mode. For the subsidiary polarisation mode, the nsd is reduced from unity at an input power of 9 dBm, but increased above unity at 15 dBm. This increase in nsd may well be associated with the significant power in the sidebands of the transmitted signal spectrum at low L_m, as shown in fig. 3.4 (k). The transmitted power spectra of fig. 3.4 are of great interest towards the aim of simulating transmission performance degradations using practicably low model fibre lengths and are discussed in detail below.

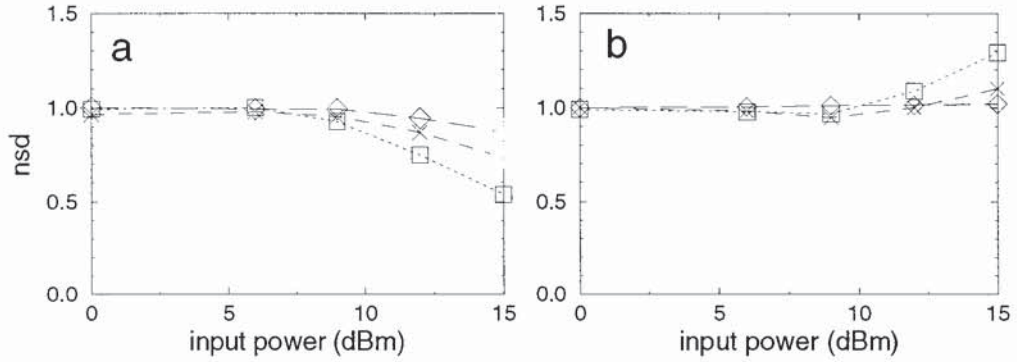

Fig. 3.5: Normalised standard deviation of the simulated SBS backscattered intensity for (a) the dominant and (b) the subsidiary polarisation modes as a function of CW input power and for model fibre lengths of 31 m (square, dotted), 124 m (cross, dashed) and 496 m (diamond, long dashed).

In fig. 3.6, the effect of varying L_m between 31 and 496 m on the simulated SBS backscattered and transmitted power characteristics is shown. Apart from the decrease in backscattered power with increasing L_m for the subsidiary polarisation mode at high input powers, there is no significant dependence on L_m for either of the backscattered or transmitted powers. Since the subsidiary mode power is 30 to 40 dB lower than that for the dominant mode at these input powers, the total backscattered power is essentially independent of L_m. The agreement of the simulated SBS backscattered powers with those obtained by numerical integration of the theoretical (undepleted pump) spectral densities obtained for fig. 3.4 is excellent for input powers up to 9 dBm. At 12 dBm, the simulated powers for both polarisation modes are seen to be much smaller than the corresponding theoretical ones due to pump depletion.

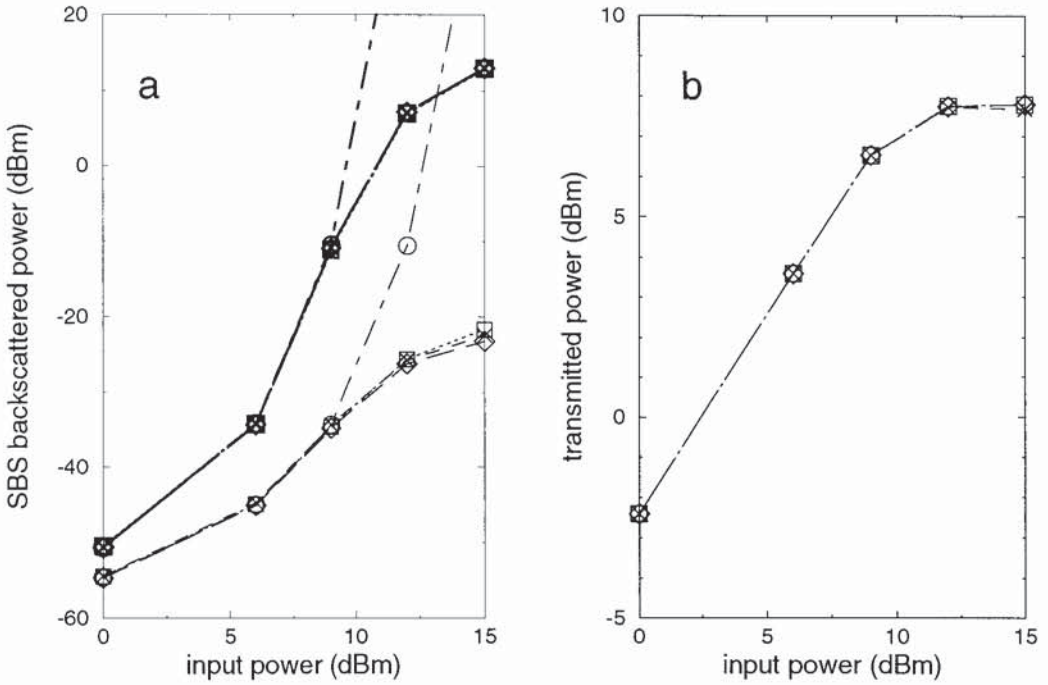

Fig. 3.6: (a) SBS backscattered power for the dominant (bold) and subsidiary (normal) polarisation modes and (b) transmitted power as functions of CW input power from (i) simulation for model fibre lengths of 31 m (square, dotted), 124 m (cross, dashed) and 496 m (diamond, long dashed), (ii) undepleted pump theory (circle, dot-dashed in (a), not shown in (b)) assuming a uniform fibre model.

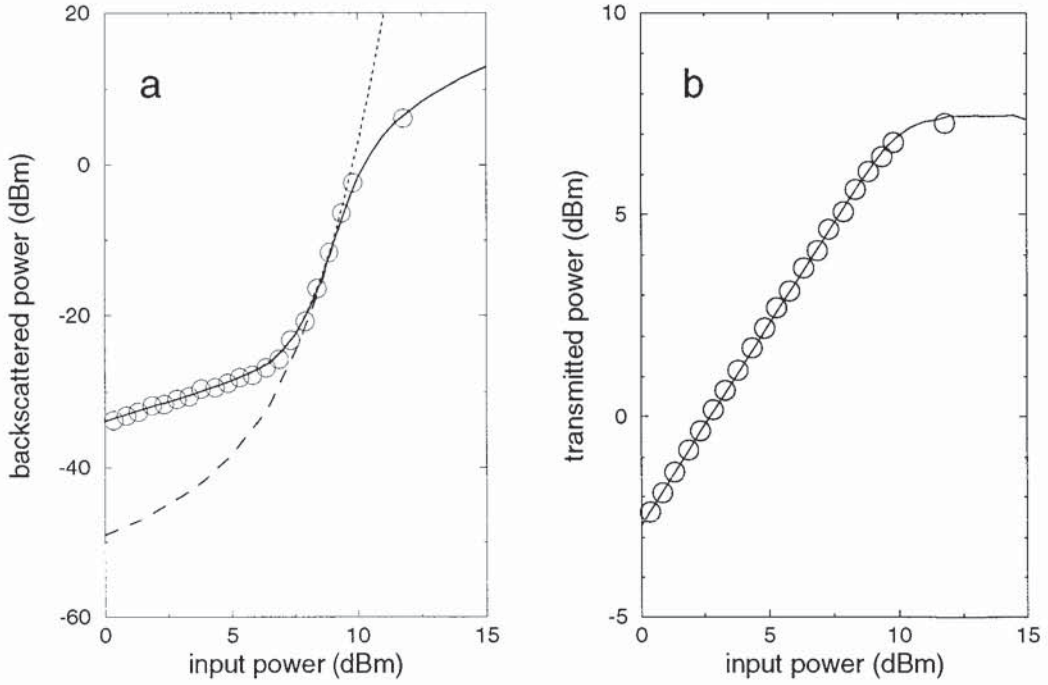

Fig. 3.7: (a) Backscattered and (b) transmitted powers as functions of CW input power from (i) experiment (circles) [3.2.2], (ii) simulation assuming uniform fibre model and including Rayleigh backscattering at -34.0 dB (solid), (iii) undepleted pump theory with assumptions of (ii) (dotted in (a), not shown in (b)), (iv) simulation of SBS alone (dashed).

It is apparent from the above that although the simulated backscattered and transmitted power characteristics of fig. 3.7 have been obtained for a model fibre length of 124 m, the same characteristics would have been generated for much higher lengths and that these may therefore be compared to the equivalent experimental ones for a true fibre length of 12.7 km. The agreement between the simulated curves and experimental points is very good for the fitting factor of $g_B = 1.943.10^{-11}$ m.W^{-1}. The value of g_B predicted using (2.1.17) with $\lambda_o = 1.537$ μm, $\Delta\nu_B = 42$ MHz, $v_a = 5.81.10^3$ m.s^{-1}, n = 1.44 and other parameters as for fused silica is $g_B = 1.73.10^{-11}$ m.W^{-1}. The discrepancy between this and the fitting factor is 0.5 dB. In the next chapter, the merits of adopting a nonuniform fibre model are discussed and corresponding simulated power characteristics compared with the same experimental points.

Simulated transmitted power spectra for the same example as above are shown in bold on the right hand side of fig. 3.4 for input powers of 0 to 15 dBm and model fibre lengths, L_m, of 31 to 991 m. Each transmitted power spectrum appears to consist of three elements:

(i) a line spectrum corresponding to the attenuated and SBS depleted optical carrier which is independent of L_m,

(ii) an underlying SBS noise spectrum which is also independent of L_m,

(iii) an approximately triangular spectrum which depends on L_m as well as input power.

At an input power of 0 dBm, the third of these spectral elements is not apparent for $L_m \geq 31$ m. As the input power increases, this element becomes more significant. By extrapolating from the spectra shown, it is estimated that even at $L_m = 12.7$ km, the experimental fibre length, some length dependent spectrum may dominate at low relative frequencies at input powers above about 12 dBm.

It is of great practical interest to know whether the underlying length independent SBS noise spectrum can be simulated in the absence of the other two spectral

elements using a small model fibre length for which processing times will be practicable. This would then represent the transmitted SBS noise for fibre lengths well in excess of about 10 km over the input power range of most interest, namely from below a threshold at which backscattered power from SBS becomes comparable to that from Rayleigh backscattering up to a level at which the mean transmitted power is close to saturation. It is shown in Appendix 3.2 that this component of transmitted SBS noise, the "inferred" transmitted SBS noise, may be simulated by solving two more partial differential equations in addition to the three given in (3.2.3a) to (3.2.3c) for each of the two polarisation modes:

$$[d/d\tau + d/d\zeta]E_{1xn} = -E_{2n}Q_{Px} - \alpha_n E_{1xn} \qquad (3.6.3a)$$

$$[d/d\tau + \delta]Q_{Px} = f_{nthnPx}, \qquad (3.6.3b)$$

where E_{1xn} represents the field envelope for the inferred transmitted SBS noise, Q_{Px} corresponds to the density variation envelope for spontaneous rather than stimulated Brillouin scattering and f_{nthnPx} is a thermal noise term equivalent to f_{nthnP} except that it is uncorrelated with f_{nthnP}. E_{2n} is the backscattered field envelope as obtained from (3.2.3a) to (3.2.3c).

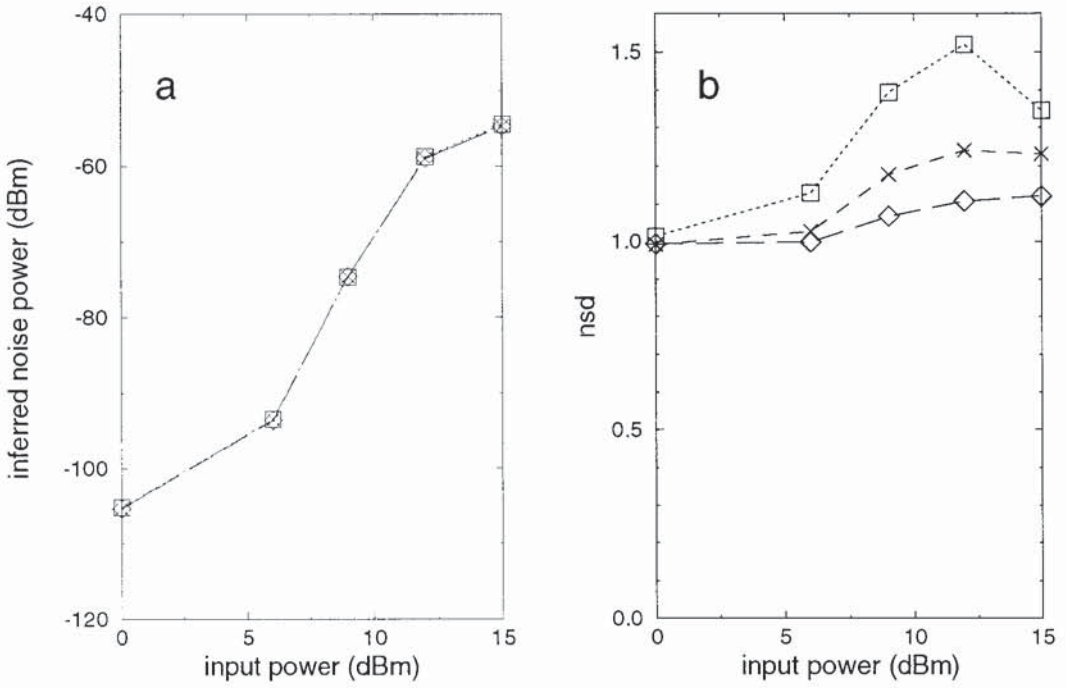

Fig. 3.8: (a) Mean and (b) normalised standard deviation of the inferred noise component power of the simulated transmitted signal as a function of CW input power and for model fibre lengths of 31 m (square, dotted), 124 m (cross, dashed) and 496 m (diamond, long dashed).

The simulated power spectra for the inferred transmitted SBS noise are shown in normal thickness on the right hand side of fig. 3.4 together with the corresponding complete transmitted power spectra (in bold) for the same input powers and model fibre lengths. It can be seen that the complete spectra converge on the inferred spectra with increasing magnitude of relative frequency and with increasing L_m and also that the inferred spectra at different L_m are indistinguishable from each other. From fig. 3.8 (a), it can be seen that the total inferred noise power does not vary with L_m over the range 31 to 496 m. However, the nsd of the instantaneous inferred noise power does vary with L_m and input power, as shown in fig. 3.8 (b). This implies that, at least for the uniform fibre model, inferred noise simulated at low L_m for higher true fibre lengths may be used for computing detected carrier-to-noise ratios in analogue transmission systems but that greater care is needed for simulating Bit Error Rates of digital baseband systems where the statistical distribution of the noise may be important.

3.7 CONCLUSIONS

A computer model for SBS based on the assumption that the Brillouin shift frequency (BSF) is constant over the length of the fibre has been developed. A normalised version of the thermal acoustic noise term described by Boyd et al. [2.1.8] has been included in the normalised partial differential equations of Höök and Bolle [2.2.3]. In accordance with the theory of Deventer and Boot [3.2.2], two orthogonal polarisation modes of the SBS backscattered (Stokes) wave are simulated. For a low-birefringence fibre, this theory indicates that the mixing efficiencies of the pump with the dominant and subsidiary polarisation modes of the Stokes wave are 2/3 and 1/3, respectively.

The computer model has been tested by reproducing representative simulation results reported by Boyd et al. for the example of SBS in CS_2 for a single

polarisation mode [2.1.8]. The simulated mean and standard deviation of the Stokes intensity are in excellent agreement with the characteristics simulated in [2.1.8]. It is found that the simulation of optical fibre lengths greater than about 1 km requires excessive processing time, so the distance scaling strategy of Höök and Bolle [2.2.3] has been adopted, whereby a model fibre, which is shorter than the real fibre but has the same end-to-end loss and Brillouin gain, is simulated.

Characteristics of mean optical output and backscattered powers as functions of input power for a CW input signal have been simulated using the uniform fibre model (UFM) and compared with those from an experiment by Deventer and Boot [3.2.2], in which light at 1.537 μm is coupled into a 12.7 km single-mode fibre. With the UFM Brillouin gain linewidth made equal to 42 MHz, the sum of the measured Brillouin gain and laser linewidths, the simulated and experimental characteristics agree very well if the Brillouin gain coefficient, g_B, is set to $1.943.10^{-11}$ m.W^{-1}. The equivalent value predicted from theory for a Brillouin gain linewidth of 42 MHz, a fibre core refractive index of 1.44, an acoustic velocity of $5.81.10^3$ m.s^{-1}, corresponding to the measured BSF of 10.88 GHz, and other parameters as for fused silica is $g_B = 1.73 . 10^{-11}$ m.W^{-1}. The difference between this and the fitting factor is 0.5 dB. In the next chapter, the merits of adopting a nonuniform fibre model are discussed and corresponding simulated power characteristics compared with the same experimental points.

The UFM simulated output and backscattered powers are independent of model fibre length, L_m, in the range investigated of 31 to 496 m. Agreement of the simulated backscattered power characteristic with undepleted pump theory is excellent for input powers up to 9 dBm. Each simulated transmitted power spectrum appears to consist of three elements:

(i) a line spectrum, corresponding to the attenuated and SBS depleted optical carrier, which is independent of L_m,

(ii) an underlying SBS noise spectrum which is also independent of L_m,

(iii) an approximately triangular spectrum which depends on L_m as well as input power.

The third of these elements decreases with increasing relative frequency and increasing L_m and increases with increasing input power. This arises from the depletion term corresponding to the product of the Stokes field and the Brillouin amplified, or stimulated, component of the density variation. It has been shown, to the best of my knowledge for the first time, that the second of these elements, the "inferred" transmitted SBS noise, may be simulated by solving two more partial differential equations in addition to the three principal ones for each of the two polarisation modes. The inferred transmitted SBS noise arises from the depletion term corresponding to the product of the Stokes field and the thermal, or spontaneous, component of the density variation. This Stokes-spontaneous density depletion noise (SSDDN) would not be apparent if a Stokes seed were used in the model rather than including distributed thermal acoustic noise. The simulated inferred transmitted SBS noise power is found to be independent of model fibre length in the range investigated of 31 to 496 m.

4. MODELLING OF SBS FOR A NONUNIFORM FIBRE

Brillouin gain linewidths of optical fibres have been found to be greater than that for bulk fused silica by a factor of from just over one to about ten. In section 4.1, this increase is attributed principally to variability of the properties of the core and cladding materials and hence to differences in Brillouin shift frequency for light travelling in different parts of the core-cladding cross-section and to fluctuations in BSF along the fibre length. A model to represent this fibre nonuniformity is proposed and its validity confirmed for the case of a silica core fibre from an analysis of reported measurements. In section 4.2, the SBS partial differential equations for the uniform fibre model are modified such that the BSF can be specified independently for each small section of the model fibre. In section 4.3, the procedure for numerically solving the PDEs for the nonuniform fibre model is described. In section 4.4, the verification of the numerical model for spatial variation of the BSF given by simple test patterns and a pseudorandom generator with a Gaussian probability density function is outlined.

In section 4.5, nonuniform fibre model (NFM) simulated characteristics of optical transmitted and backscattered powers as functions of input power for a CW optical input carrier are compared with those for the same published experiment as in the previous chapter. The Brillouin gain coefficient spectra required for the uniform and nonuniform fibre models to fit these experimental characteristics are contrasted and used to explain the similarities and differences between the corresponding UFM and NFM characteristics of transmitted signal, transmitted noise and backscattered powers as functions of input power. Transmitted and backscattered power spectra for different input powers and model fibre lengths are also shown and discussed, together with statistical characteristics.

4.1 VARIATION OF BRILLOUIN SHIFT FREQUENCY AS A FUNCTION OF DISTANCE

The Brillouin gain spectrum of a single mode fibre differs from the simple Lorentzian form for bulk fused silica, as previously discussed in section 2.2.6. The linewidth of the principal spectral lobe is broader than that for bulk silica partly because there is some variation in dopant concentration over the cross-section of the fibre core, even in nominally pure silica core, step-index fibres. The acoustic velocity and hence, through the relationship of (2.1.6), the Brillouin shift frequency (BSF) vary with dopant concentration, so that light travelling in different parts of the core is Brillouin backscattered with different BSFs [2.1.19]. In addition, the cross-sectional profile of dopant concentration may vary over the length of the fibre.

For a fibre with a GeO_2-doped silica core and a pure silica cladding, three longitudinal acoustic modes are typically guided for a pump wavelength of 1.55 μm, giving rise to a principal Brillouin gain spectral lobe and two subsidiary lobes with higher BSFs. The BSF of the principal lobe depends on the radius of the SMF core as well as its dopant concentration [2.1.14],[2.1.18]. For example, the BSF of a GeO_2-doped core fibre with a relative refractive index difference between core and cladding of 0.84% varies between 10.54 GHz for a core radius a = 3.5 μm and 10.52 GHz for a = 5.2 μm [1.3.11],[2.1.18]. For a = 5 μm and a GeO_2 doping concentration in the core of 3.7 mol.%, the BSF is about 10.86 GHz, compared to about 11.18 GHz for a fibre with a pure silica core and a Fluorine doped cladding [4.1.1]. This corresponds to a sensitivity of 86 MHz/mol.%. The core radius and dopant concentration may both vary along the fibre length, contributing to variations in BSF as a function of distance.

The process of drawing fibres from preforms gives rise to residual stresses in the core, which vary across the profile and according to the drawing tension. For a fibre with a pure silica core and a Fluorine doped cladding such that the relative index difference is 0.27%, an increase in the drawing tension from 5 g to 85 g resulted in

an increase in the BSF of 145 MHz at 1.55 μm in accordance with the measured and theoretically predicted residual stresses [4.1.2]. The cabling of optical fibres can also lead to tensile and compressive strain variations along the fibre length, with corresponding changes in BSF and a broadened end-to-end Brillouin gain spectrum. For a 4-fibre ribbon wound round a slot-type cable with a stranding pitch of 0.5 m, variations in strain in an outer fibre when the cable was wound on a drum of 200 mm radius broadened the Brillouin gain bandwidth (BGB) to 182 MHz at 1.3 μm compared to 42 MHz in the absence of strain [4.1.3].

The temperature coefficient of the BSF of a pure silica core fibre has been found to be in good agreement with that for bulk fused silica and is 1.42 MHz/°C at 1.3 μm, while that for a GeO_2 doped core fibre with 0.3% relative index difference is similar but slightly smaller [4.1.4]. The temperature coefficients of the BGB for these two fibres are also similar to that of bulk silica and are about -0.1 MHz/°C. The fact that the BGB is 34 MHz at 25 °C and 1.3 μm for the pure silica core fibre and 39 MHz for the GeO_2 doped core fibre compared to about 20 MHz for bulk silica is attributed in [4.1.4] to the inhomogeneous refractive index profiles of the fibres and the variations in dopant concentrations and residual stress along the fibre lengths, as described above.

As a consequence of the dependence of the BSF on these factors, the Brillouin gain spectrum can vary substantially both in shape and bandwidth from fibre to fibre. BGBs of between 20 MHz [4.1.5] and 100 MHz at 1.55 μm have been reported. Nevertheless, it is useful to make some simplifying assumptions in order to provide a SBS model which will enable approximate predictions of performance to be made. The fibre length may be considered to be divided into a large number, N_b, of sections, in each of which the uniform fibre model may be applied for a value of BSF specific to that section. BSF may be specified as a function of discrete distance in order to model not only the variations along the fibre length, but also those across the fibre core cross section, at least approximately. (For a GeO_2-doped core fibre, the subsidiary Brillouin gain spectral lobes associated with the higher order guided

acoustic longitudinal modes could be represented by arranging for appropriate proportions of the discrete distance sections to have BSFs displaced by about one or two acoustic mode frequency intervals. In the present work, only the principal lobe associated with the fundamental longitudinal acoustic mode is simulated, together with broadening from variation of the corresponding BSF.)

In each constant BSF section, the phonon decay rate is chosen to be that expected for an ideally homogeneous sample of the core material. The resultant broadening of the modelled Brillouin gain spectrum (BGS) from the theoretical Lorentzian spectrum to give a specified or measured BGB will then be achieved by means of BSF variations, which are believed to occur in real fibres, rather than by artificially increasing the phonon decay rate and assuming a constant BSF over the fibre length and core cross section, as is done for the uniform fibre model case.

If the BSF variations are assumed to arise from several different mechanisms, each of which contributes a probability density function (pdf) for the BSF with a similar standard deviation, then, according to the central limit theorem, the overall pdf is approximately Gaussian, even though the individual contributing pdfs may not be. On the basis of this assumption, the specified variation of BSF with discrete distance for the model is therefore modelled as a random variable with a Gaussian pdf and a uniform (or white) power spectral distribution. This latter stipulation is equivalent to demanding that the discrete random samples are independent of each other or that the mean autocorrelation is a discrete delta function, as also assumed for the modelled acoustic thermal noise variable, f_{nthn}, defined in (3.1.9). Unlike f_{nthn}, however, the BSF random variable is a function of discrete distance only and not of discrete time.

The assumption of a Gaussian pdf for the BSF is not expected to represent all fibres well. As indicated above, this assumption results in the subsidiary BGS lobes for a GeO_2 doped core fibre being neglected. The more complex design of the refractive

index cross-sectional profile for a dispersion-shifted fibre may also lead to a significantly different BGS from that generated using the Gaussian assumption.

In order to test the validity of this assumption for a relatively simple case, the Brillouin gain spectrum has been derived from power spectral measurements for a pure silica core fibre with F-doped cladding reported in [4.1.6]. In this experiment, the backward-travelling Stokes wave was dominated by that from a polarisation-scrambled optical signal with a white spectral distribution over at least the nominal Stokes optical frequency ± 50 MHz. In this way, the fibre was tested in a Brillouin amplifier mode at a wavelength of 1.55 μm and the power spectrum of the amplified probe signal was recorded at the pump end. It has been found that the Brillouin gain spectrum, which has been obtained by suitable processing of the beat spectra in fig. 2 of [4.1.6] and shown here in fig. 4.1, fits a theoretical spectrum consisting of the convolution of a Lorentzian spectrum, having a FWHM bandwidth of about 11 MHz, with a Gaussian probability density function (pdf) of relative frequency, f_r, for which the mean value of f_r is equal to zero and the standard deviation of f_r is 9.5 MHz.

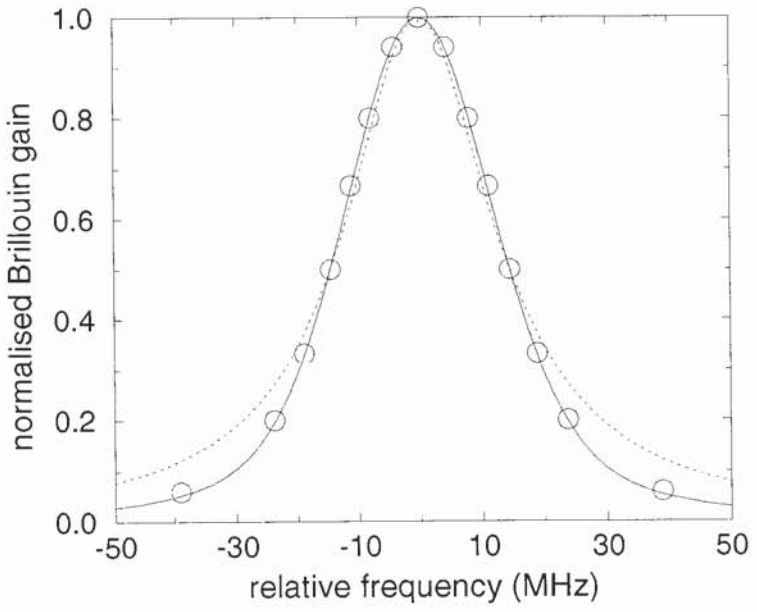

Fig. 4.1: Comparison of measured normalised Brillouin gain spectrum (circles), obtained from fig. 2 of [4.1.6], with (i) Lorentzian spectrum of FWHM bandwidth of 29.1 MHz (dotted) and (ii) convolution of Lorentzian spectrum with FWHM bandwidth of 11.2 MHz and Gaussian probability density function of standard deviation equal to 9.5 MHz, for which the overall FWHM bandwidth is 29.1 MHz (dotted)

The above fitting value of the Lorentzian spectral bandwidth of 11 MHz is significantly lower than the value of BGB predicted in [1.2.3], [4.1.6] for bulk silica at 1.55 μm as 16 MHz. This may be attributed partly to the inaccuracy of extrapolating from experimental values for bulk silica at lower wavelengths using the λ_0^{-2} relationship and partly to possible variations of BSF present in the experimental samples of bulk silica due to, for example, impurities and residual stresses. The phonon decay constant for modelling single mode fibres at 1.55 μm has therefore been derived from an idealised BGB of 11 MHz rather than 16 MHz. The standard deviation of the simulated BSF is obtained by finding the value which allows the theoretical nonuniform fibre model gain spectrum, consisting, as above, of the convolution of the idealised Lorentzian gain spectrum with the Gaussian pdf of the simulated BSF, to have a bandwidth equal to the measured or specified BGB for the fibre to be modelled.

4.2 MODIFICATION OF SBS PDES

As discussed in the previous section, the model fibre length is considered to be divided into a large number, N_b, of sections, in each of which the uniform fibre model may be applied for a value of BSF specific to that section. Let the BSF in the k^{th} constant BSF length section be given by

$$\nu_{bk} = \nu_{bav} + f_{bk}, \tag{4.2.1}$$

where ν_{bav} is the average value of the BSF for the fibre and f_{bk} is the BSF in the k^{th} length section relative to ν_{bav}. In this section, the envelopes E_{1n} of the pump wave at ν_L, Q_{Pbk} of the acoustic wave at ν_{bk} and E_{2nbk} of the Stokes wave at $\nu_L - \nu_{bk}$, where ν_L is the nominal pump laser optical frequency, obey the following partial differential equations for the uniform fibre model given in (3.2.3a) to (3.2.3c) for one of the two polarisation modes:

$$[\partial/\partial\tau + \partial/\partial\zeta]E_{1n} = -E_{2nbk}Q_{Pbk} - \alpha_n E_{1n} \quad (4.2.2a)$$

$$[\partial/\partial\tau - \partial/\partial\zeta]E_{2nbk} = E_{1n}Q_{Pbk}^* - \alpha_n E_{2nbk} \quad (4.2.2b)$$

$$[\partial/\partial\tau + \delta]Q_{Pbk} = \gamma_n E_{1n}E_{2nbk}^* + f_{nthnP}, \quad (4.2.2c)$$

where the thermal noise term, f_{nthnP}, is described for (3.2.3c) and in (3.1.6) to (3.1.10). The envelopes Q_{Pbk} and E_{2nbk} may be expressed in terms of the envelopes Q_{Pbav} of the acoustic wave at ν_{bav} and E_{2nbav} of the Stokes wave at $\nu_L - \nu_{bav}$, as follows:

$$Q_{Pbk} = \exp\{i\phi_{bk}\}.Q_{Pbav} \quad (4.2.3a)$$

$$E_{2nbk} = \exp\{-i\phi_{bk}\}.E_{2nbav} \quad (4.2.3b)$$

where

$$\begin{aligned}\phi_{bk} &= \int 2\pi f_{bk}\, dt \\ &= \int 2\delta(f_{bk}/\Delta\nu_{BT})\, d\tau \\ &= \int \omega_{bkn}\, d\tau, \end{aligned} \quad (4.2.4)$$

and δ and τ are defined in (3.1.2) for the phonon amplitude decay rate $\Gamma_B = \pi\Delta\nu_{BT}$, in which $\Delta\nu_{BT}$ is the Brillouin gain linewidth for the ideally uniform core material (assumed to be about 11 MHz for pure silica at 1.55 μm).

Inserting (4.2.3a) and (4.2.3b) into (4.2.2a) to (4.2.2c) gives

$$[\partial/\partial\tau + \partial/\partial\zeta]E_{1n} = -E_{2nbav}Q_{Pbav} - \alpha_n E_{1n} \quad (4.2.5a)$$

$$[\partial/\partial\tau - \partial/\partial\zeta][E_{2nbav}.\exp\{-i\phi_{bk}\}] = (E_{1n}Q_{Pbav}^* - \alpha_n E_{2nbav}).\exp\{-i\phi_{bk}\} \quad (4.2.5b)$$

$$[\partial/\partial\tau + \delta][Q_{Pbav}.\exp\{i\phi_{bk}\}] = \gamma_n E_{1n}E_{2nbav}^*.\exp\{i\phi_{bk}\} + f_{nthnP}. \quad (4.2.5c)$$

4.3 NUMERICAL SOLUTION OF SBS PDES

After rewriting the PDEs of (4.2.5) in terms of τ" instead of τ, where τ" is defined in (3.3.1), they are equivalent to the following ODEs along their characteristics:

$$[d/d\zeta]E_{1n} = -E_{2nbav}Q_{Pbav} - \alpha_n E_{1n} \qquad \text{for } d\tau''/d\zeta = 0 \qquad (4.3.1a)$$

$$[-d/d\zeta][E_{2nbav}.\exp\{-i\phi_{bk}\}] = (E_{1n}Q_{Pbav}^* - \alpha_n E_{2nbav}).\exp\{-i\phi_{bk}\} \qquad \text{for } d\zeta/d\tau'' = -1/2 \qquad (4.3.1b)$$

$$[d/d\tau'' + \delta][Q_{Pbav}.\exp\{i\phi_{bk}\}] = \gamma_n E_{1n}E_{2nbav}^*.\exp\{i\phi_{bk}\} + f_{nthnP} \qquad \text{for } d\zeta/d\tau'' = 0. \qquad (4.3.1c)$$

Differentiating the product terms yields

$$[d/d\zeta]E_{1n} = -E_{2nbav}Q_{Pbav} - \alpha_n E_{1n} \qquad (4.3.2a)$$

$$\exp\{-i\phi_{bk}\}.[-d/d\zeta - i\omega_{bkn}][E_{2nbav}] = (E_{1n}Q_{Pbav}^* - \alpha_n E_{2nbav}).\exp\{-i\phi_{bk}\} \qquad (4.3.2b)$$

$$\exp\{i\phi_{bk}\}.[d/d\tau'' + \delta + i\omega_{bkn}][Q_{Pbav}] = \gamma_n E_{1n}E_{2nbav}^*.\exp\{i\phi_{bk}\} + f_{nthnP}, \qquad (4.3.2c)$$

which simplifies to

$$[d/d\zeta + \alpha_n]E_{1n} = -E_{2nbav}Q_{Pbav} \qquad (4.3.3a)$$

$$[-d/d\zeta + (\alpha_n - i\omega_{bkn})][E_{2nbav}] = E_{1n}Q_{Pbav}^* \qquad (4.3.3b)$$

$$[d/d\tau'' + (\delta + i\omega_{bkn})][Q_{Pbav}] = \gamma_n E_{1n}E_{2nbav}^* + f_{nthnP}', \qquad (4.3.3c)$$

where $f_{nthnP}' = \exp\{-i\phi_{bk}\}.f_{nthnP}$, so that f_{nthnP}' has the same statistical properties as f_{nthnP}, as seen from (3.1.9). (4.3.3) has the same form as (3.3.3), with the complex coefficient $(\alpha_n - i\omega_{bkn})$ in (4.3.3b) replacing the real coefficient α_n in (3.3.3b) and, similarly, $(\delta + i\omega_{bkn})$ in (4.3.3c) replacing δ in (3.3.3c). The development and solution of difference equations from the ODEs of (4.3.3) then

follow the same procedure as described in section 3.3. The N_b values of ω_{bkn} required for the N_b sections with different BSF are generated by the same functions referred to in section 3.3 for producing the thermal acoustic noise samples with a Gaussian pdf and a uniform power spectral density.

4.4 VERIFICATION OF NUMERICAL MODEL

Some of the same tests described in 3.4 for the uniform fibre model have been repeated for the nonuniform model with the relative BSF, f_{bk}, set to zero for all model fibre length sections. The results were identical to those obtained for the uniform fibre model, as expected. Setting f_{bk} for all sections equal to the same positive or negative value shifted the SBS backscattered power spectrum along the relative frequency axis by the corresponding amount. Setting f_{bk} for consecutive sections equal to an alternating pattern of positive and negative values resulted in a symmetrical twin peaked backscattered power spectrum, such as that which might be expected for a nonuniform dopant concentration across the profile of a fibre core.

When f_{bk} was set to a constant value such that its ratio with the sampling frequency, f_{bk}/f_s, is equal to 0.207, for which the phase change over a time step, ϕ_{bk}, is $(2\pi. 0.207) = 1.3$ radians, the SBS backscattered power was reduced to about 2% of its expected value. For $f_{bk}/f_s = 0.041$, so that $\phi_{bk} = 0.26$ radians, the SBS backscattered power was not noticeably reduced from its expected value, within the simulation error limits for this test. Care has therefore been taken in choosing simulation parameters for the nonuniform fibre model that the magnitude of ϕ_{bk} rarely exceeds about 0.25 radians during a run.

The Brillouin gain coefficient of the ideally uniform core material as a function of ν_R, the frequency relative to the average Stokes frequency such that $\nu_R = \nu - (\nu_L - \nu_{bav})$, is given by

$$g_{BC}\{\nu_R\} = g_{B0}.R\{\nu_R\}, \tag{4.4.1}$$

where g_{B0} is the peak Brillouin gain coefficient and $R\{\nu_R\}$ is the Lorentzian relative Brillouin gain spectrum given in (2.1.19) for $\Delta\nu_B = \Delta\nu_{BT}$.

If the pdf of the BSF is $d_{BSF}\{f = f_{bk}\}$, the Brillouin gain coefficient spectrum is given by

$$g_R = g_B\{\nu_R\} = \int_{-\infty}^{+\infty} d_{BSF}\{f\}.g_{BC}\{\nu_R - f\}df \tag{4.4.2}$$

where

$$d_{BSF}\{f\} = \frac{1}{\sigma_{BSF}\sqrt{2\pi}}\exp\left\{-\frac{f^2}{2\sigma_{BSF}{}^2}\right\} \tag{4.4.3}$$

for a Gaussian pdf of the BSF with a standard deviation of σ_{BSF}.

The theoretical nonuniform fibre model SBS backscattered power spectral density has been obtained by numerically evaluating $g_B\{\nu_R\}$ using (4.4.2) and (4.4.3) and numerically integrating (2.1.23) for $g = g_B\{\nu_R\}$. This theoretical power spectrum is derived on the assumption that depletion of the pump by SBS is negligible. Agreement between simulated and theoretical power spectra for the nonuniform model has been found to be excellent for sufficiently low input powers, as also previously shown in fig 3.4 for the uniform model. In the next section, a comparison between simulated SBS backscattered powers and those obtained by numerical integration of these theoretical power spectra over the simulated frequency range is shown to give close correspondence at low input powers for the chosen example.

4.5 COMPARISON WITH EXPERIMENTAL RESULTS

The input parameters for the nonuniform fibre model are chosen to match the conditions of the same experiment as referred to in section 3.6, in which mean optical output and backscattered powers were characterised as functions of input power for a CW input signal in fig. 3 of [3.2.2]. The phonon amplitude decay constant is assumed to be given by $\Gamma_B = \pi\Delta\nu_{BT}$, in which $\Delta\nu_{BT}$ is the Brillouin gain linewidth for the ideally uniform core material. In section 4.1, $\Delta\nu_{BT}$ was deduced to be about 11 MHz for pure silica at 1.55 μm. This value is also used for the model here, even though the fibre core for the experiment was probably GeO_2 doped. However, it is increased to 13 MHz to take account of the laser linewidth of 2 MHz. The standard deviation of the BSF, σ_{BSF}, is then chosen to give a theoretical nonuniform model Brillouin gain linewidth of 42 MHz, the sum of the measured Brillouin gain and laser linewidths.

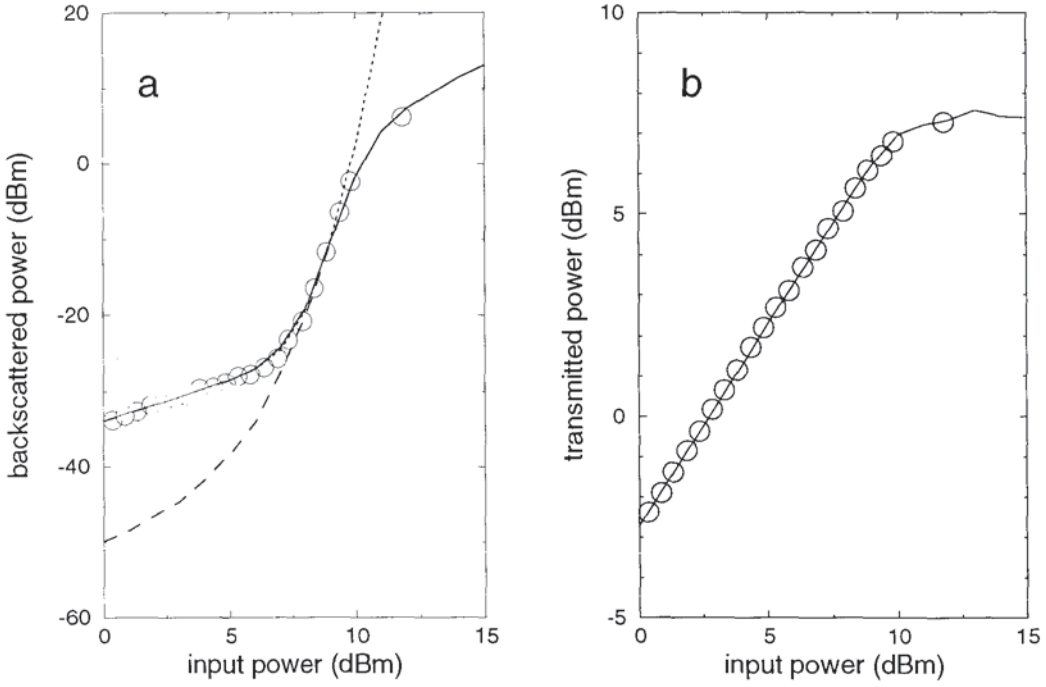

Fig. 4.2: (a) Backscattered and (b) transmitted powers as functions of CW input power from (i) experiment (circles) [3.2.2], (ii) simulation assuming nonuniform fibre model and including Rayleigh backscattering at -34.0 dB (solid), (iii) undepleted pump theory with assumptions of (ii) (dotted in (a), not shown in (b)), (iv) simulation of SBS alone (dashed).

The Brillouin gain coefficient, g_B, is selected to give the best fit between the simulated and experimental characteristics of backscattered power as a function of

input power shown in fig. 4.2 a) and is equal to $4.72.10^{-11}$ m.W^{-1}. The polarisation factors, core refractive index and acoustic velocity are the same as those given and discussed in section 3.6. The number of length sections for PDE solution, N_ζ, and the number of sections with different BSFs, N_b, are both 2,000, while the model fibre length, L_m, is 400 m, as reviewed below.

The agreement between the simulated curves and experimental points of fig. 4.2 is very good for both the backscattered and transmitted power characteristics with the fitting factor, g_B, equal to $4.72.10^{-11}$ m.W^{-1}. The value of g_B predicted using (2.1.17) with $\lambda_o = 1.537$ μm, $\Delta\nu_B = 13$ MHz, $v_a = 5.81.10^3$ m.s^{-1}, n = 1.44 and other parameters as for fused silica is $g_B = 5.59.10^{-11}$ m.W^{-1}. The discrepancy between this and the fitting factor is 0.7 dB. Up to 0.3 dB of this difference could be explained by assuming that the additional loss of 0.3 dB in the experiment of [3.2.2] occurs between the input power measurement point and the fibre, rather than between the fibre and the output power measurement point, as presumed in section 3.6. Another 0.3 dB may be accounted for if the measured Brillouin gain linewidth (BGL) is assumed to be at its upper limit of quoted accuracy at 43 MHz, so that the modelled BGL, taking into account the 2 MHz laser linewidth, should have been 45 rather than 42 MHz. Other possible sources of the discrepancy are slight differences in the density, ρ_0, and photoelastic constant, p_{12}, for the GeO_2 doped core compared to those for pure silica. Additionally, since the GeO_2 doped core fibre is expected to guide two subsidiary acoustic longitudinal modes as well as the principal one, it seems likely that the Brillouin gain coefficient for the principal acoustic mode may be modified in comparison to its value for the bulk material of the core in the absence of acoustic waveguiding [2.1.13].

The theoretical Brillouin gain coefficient spectrum (bgcs) for the nonuniform fibre model, evaluated using (4.4.2) and (4.4.3) with the above input fitting parameters, is compared in fig. 4.3 to that for the uniform model obtained for the parameters described in 3.6 to match the same experimental data and characteristics. The peak value of the nonuniform model bgcs is $1.922.10^{-11}$ m.W^{-1}, while that for the

uniform model is $1.943.10^{-11}$m.W^{-1}. These two spectra are quite close to each other from half maximum to maximum height, but diverge at lower heights.

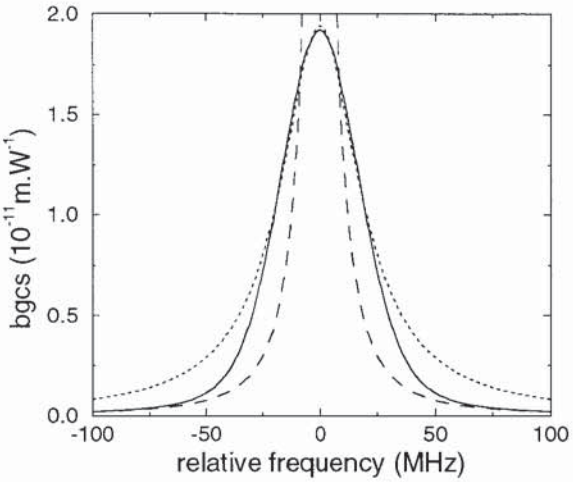

Fig. 4.3: Brillouin gain coefficient spectrum (bgcs) for (a) nonuniform fibre model (solid) with Lorentzian spectrum of g_{B0} = $4.72.10^{-11}$ m.W^{-1} and linewidth = 13 MHz convoluted with Gaussian pdf of $\sigma\{f_B\}$ = 1.112 . 13 MHz = 14.5 MHz, (b) uniform fibre model (dotted) with Lorentzian spectrum of g_{B0} = $1.943.10^{-11}$ m.W^{-1} and linewidth = 42 MHz and (c) Lorentzian spectrum (dashed) with g_{B0} = $4.72.10^{-11}$ m.W^{-1} and linewidth = 13 MHz.

The sampling frequency, f_S, has been kept at about the same value as for the uniform fibre model (UFM) comparison with experiment described in section 3.6. In order to achieve this, the ratio $k_R = f_S/\Delta\nu_{BTe}$, in which $\Delta\nu_{BTe}$ is the sum of the Brillouin gain linewidth for the ideally uniform core material and the laser linewidth, has been increased from 10 for the UFM to 40 for the nonuniform fibre model (NFM), corresponding approximately to the decrease of $\Delta\nu_{BTe}$ from 42 to 13 MHz. According to (3.6.2), N_ζ should then be increased from 500 to 2,000 for the case of $\Gamma_i T_t$ = 157. For these values of N_ζ and k_R, (3.6.1) yields L_m = 400 m for $\Delta\nu_{BTe}$ = 13 MHz and for $v_g = c/n$, where n = 1.44. In the investigation of the dependence of the simulated power spectra and statistical parameters on model fibre length, L_m, to be described, N_ζ is kept proportional to L_m with k_R maintained at 40 for 100 m $\leq$ $L_m \leq$ 801 m. In order that N_ζ is not reduced to below 500, k_R is increased to 160 for L_m = 25 m. The number of sections with different BSFs, N_b, is in all cases equal to the number of length sections for PDE solution, N_ζ.

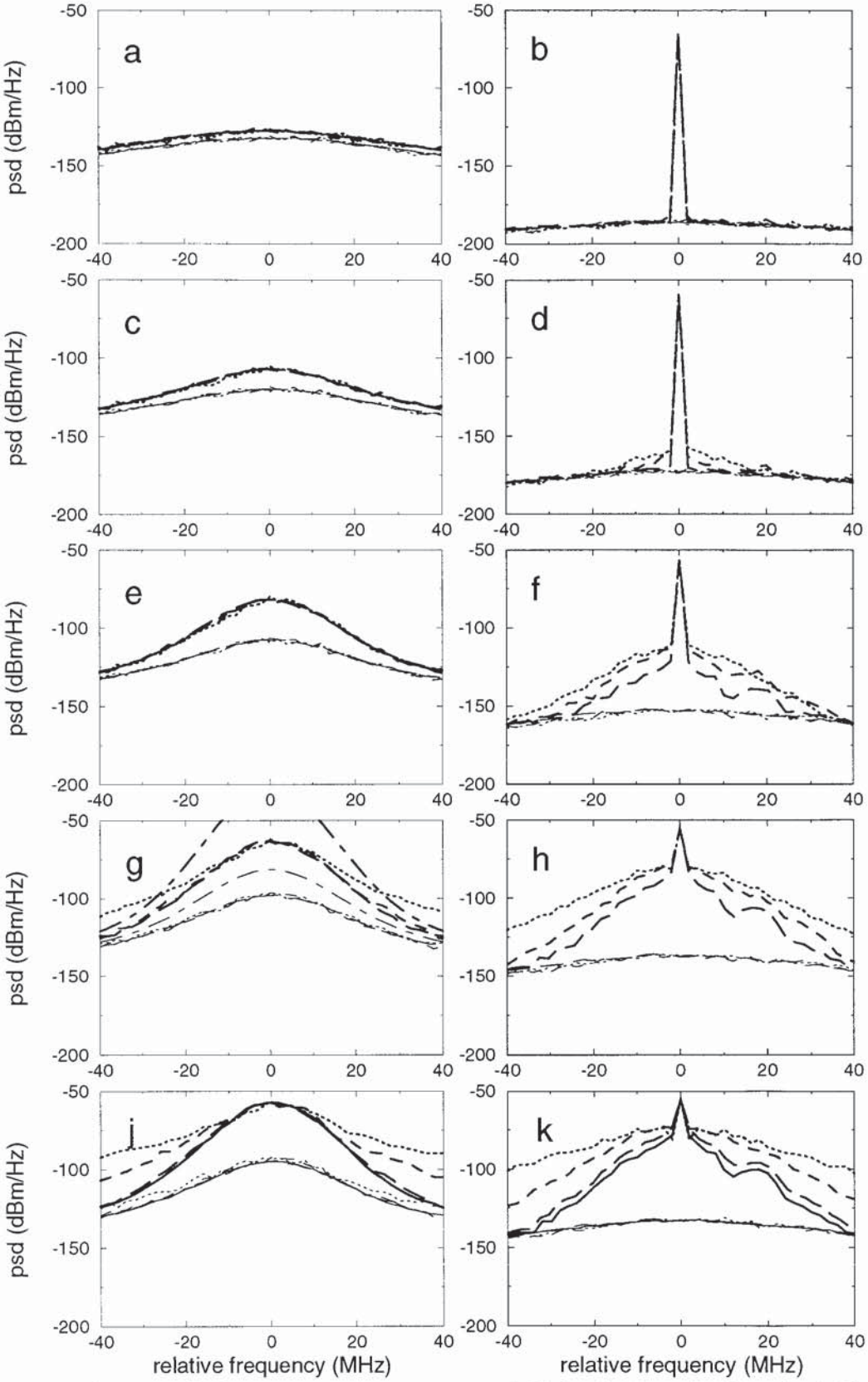

Fig. 4.4: Simulated SBS backscattered power spectra (left) for dominant (bold) and subsidiary (normal) polarisation modes and transmitted power spectra (right, bold) with corresponding inferred SBS noise spectra (right, normal) for CW input powers of 0 dBm (a, b), 6 dBm (c, d), 9 dBm (e, f), 12 dBm (g, h), 15 dBm (j, k). Model fibre lengths of 25 m (dotted), 100 m (dashed), 400 m (long dashed) and, for 15 dBm only, 801 m (solid) have been simulated. Theoretical SBS backscattered power spectra assuming no pump depletion from SBS (dot-dashed) are shown for all powers except 15 dBm. Each power spectral density (psd) is determined as the average in a bandwidth of 2.0 MHz. A nonuniform fibre model has been assumed with parameters such that the theoretical Brillouin gain coefficient spectrum (bgcs) is as shown in fig. 4.3 with an effective linewidth of 42 MHz and a peak bgcs of 1.922. 10^{-11} $m.W^{-1}$. The fibre loss is equivalent to that for 12.7 km at 0.19dB/km.

From the simulated SBS backscattered power spectra shown in fig. 4.4 for input powers of 0 to 15 dBm and model fibre lengths of 25 to 801 m, it is clear that these spectra at L_m = 400 m are very close to convergence for input powers up to 15 dBm. The theoretical SBS backscattered power spectra also shown in fig. 4.4 have been obtained by numerical integration of (2.1.23), based on the assumption of an undepleted pump, in which the theoretical NFM Brillouin gain coefficient spectrum of fig. 4.3 is substituted. The agreement of the modelled and theoretical backscattered spectra is excellent at all the selected values of L_m for input powers up to 9 dBm. At 12 dBm, the modelled spectra for both polarisation modes are seen to be substantially smaller than the corresponding theoretical ones due to pump depletion.

Each of the simulated transmitted power spectra of fig. 4.4 generally consists of the same three spectral elements as for the equivalent UFM spectra of fig. 3.4:

(i) a line spectrum corresponding to the attenuated and SBS depleted optical carrier which is independent of L_m,

(ii) an underlying SBS noise spectrum which is also independent of L_m,

(iii) an approximately triangular spectrum which depends on L_m as well as input power.

At an input power of 0 dBm, the third of these spectral elements is not apparent for $L_m \geq 25$ m. As the input power increases, this element becomes more significant. The underlying SBS noise spectrum is well modelled by the inferred transmitted SBS noise spectrum which is shown in conjunction with the complete simulated transmitted power spectrum in each case. It can be seen that the complete spectra converge on the inferred spectra with increasing magnitude of relative frequency and with increasing L_m and also that the inferred spectra at different L_m are similar to each other.

The L_m-dependent component of each NFM transmitted power spectrum of fig. 4.4 exhibits substantially greater fluctuation than that shown in fig. 3.4 for the UFM. Most of this fluctuation is associated with the simulated longitudinal pattern of Brillouin shift frequency (BSF) variation and a smaller amount with the simulated thermal acoustic noise as a function of distance and time. Both the BSF and thermal noise sequences are initiated, and therefore controlled, by the same set of seed numbers.

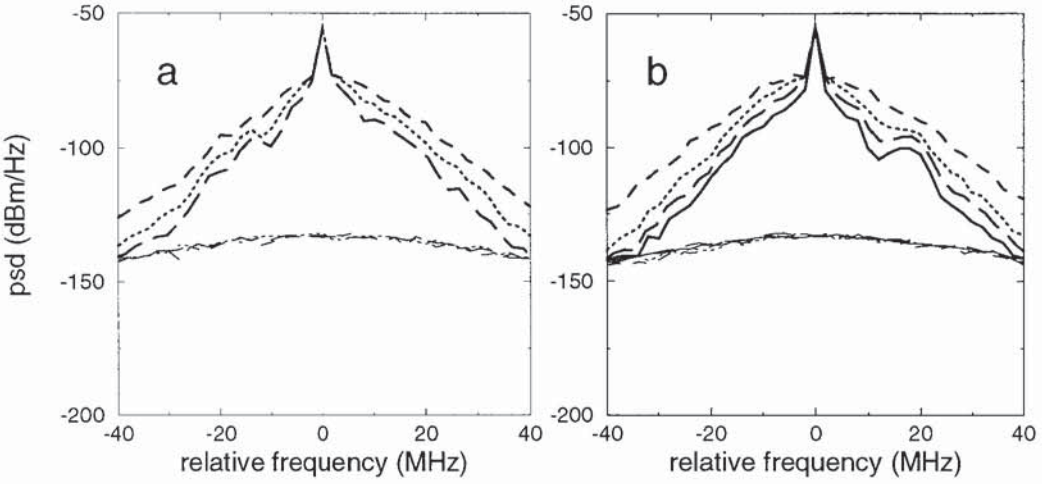

Fig. 4.5: Simulated transmitted power spectra (bold) with corresponding inferred SBS noise spectra (normal) for a CW input power of 15 dBm and two seeds defining the simulated thermal noise and Brillouin shift frequency longitudinal variation sequences: seed A (a) and seed B (b). Model fibre lengths of 100 m (dashed), 200 m (dotted), 400 m (long dashed) and, for seed B only, 801 m (solid) have been simulated. Each power spectral density (psd) is determined as the average in a bandwidth of 2.0 MHz. A nonuniform fibre model has been assumed with parameters such that the theoretical Brillouin gain coefficient spectrum (bgcs) is as shown in fig. 4.3 with an effective linewidth of 42 MHz and a peak bgcs of 1.922. 10^{-11} $m.W^{-1}$. The fibre loss is equivalent to that for 12.7 km at 0.19dB/km.

In fig. 4.5, simulated transmitted power spectra with corresponding inferred SBS noise spectra are shown for a CW input power of 15 dBm and two seeds. Those generated with seed A are given in fig. 4.5a, and those with seed B in fig. 4.5b. There is a degree of similarity between the spectra at different model fibre lengths for each seed, particularly at the higher values of L_m. For example, this is specially noticeable in fig. 4.5b at relative frequencies between 10 and 25 MHz. For all cases of L_m shown, the sampling frequency is the same and the variation of BSF with distance along the model fibre from the pump input end is also the same for a given seed. The apparently greater spectral fluctuations at higher L_m are consistent with

the narrowing of the triangular element of the transmitted spectrum with increasing L_m which occurs for the uniform model, as shown in fig. 3.4.

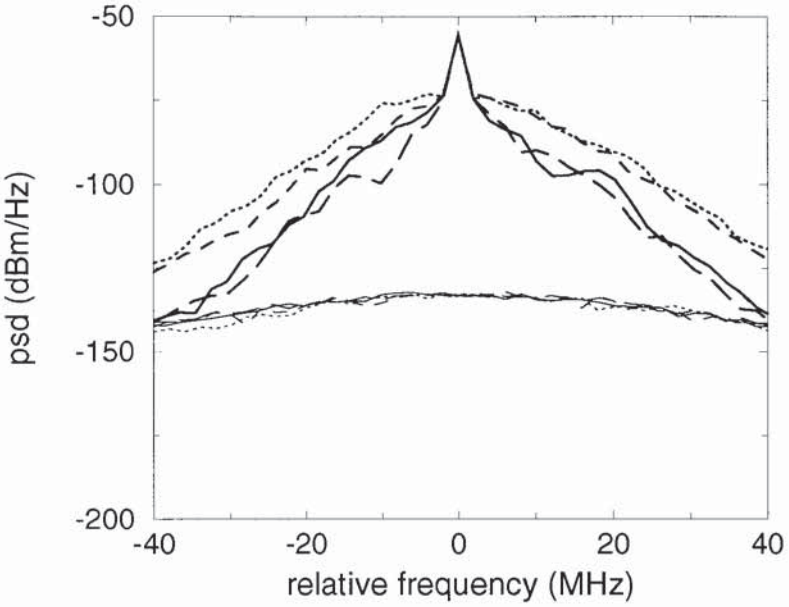

Fig. 4.6: Simulated transmitted power spectra (bold) with corresponding inferred SBS noise spectra (normal) for a CW input power of 15 dBm and two seeds defining the simulated thermal noise and Brillouin shift frequency longitudinal variation sequences: seed A (dashed and long dashed) and seed B (dotted and solid). Model fibre lengths of 100 m (dotted and dashed) and 400 m (long dashed and solid) have been simulated. Each power spectral density (psd) is determined as the average in a bandwidth of 2.0 MHz. A nonuniform fibre model has been assumed with parameters such that the theoretical Brillouin gain coefficient spectrum (bgcs) is as shown in fig. 4.3 with an effective linewidth of 42 MHz and a peak bgcs of 1.922. 10^{-11} m.W^{-1}. The fibre loss is equivalent to that for 12.7 km at 0.19dB/km.

In fig. 4.6, transmitted spectra for seeds A and B at L_m = 100 m and L_m = 400 m are superimposed on each other. For each value of L_m, the spectra for the two seeds are seen to follow the same underlying characteristic but with variations specific to that seed. This indicates the importance of taking the average and monitoring limits of uncertainty using different seeds when simulating transmitted power spectra and related system performance measures such as carrier-to-noise ratio with the nonuniform fibre model.

As in the case of the uniform fibre model, at high input powers, the divergence of the NFM SBS backscattered spectra of fig. 4.4 at low values of L_m from the convergent spectra attained for sufficiently high L_m is accompanied by a change in the normalised standard deviation (nsd = standard deviation/mean) of the instantaneous SBS backscattered power from unity, as shown in fig. 4.7. For the

dominant polarisation mode, the nsd is reduced from unity under these conditions, as also observed in [2.1.8] from their simulations for a single polarisation mode. For the subsidiary polarisation mode, the nsd is reduced very slightly from unity at an input power of 9 dBm, but increased above unity at 15 dBm. This increase in nsd may well be associated with the significant power in the sidebands of the transmitted signal spectrum at low L_m, as shown in fig. 4.4 (k).

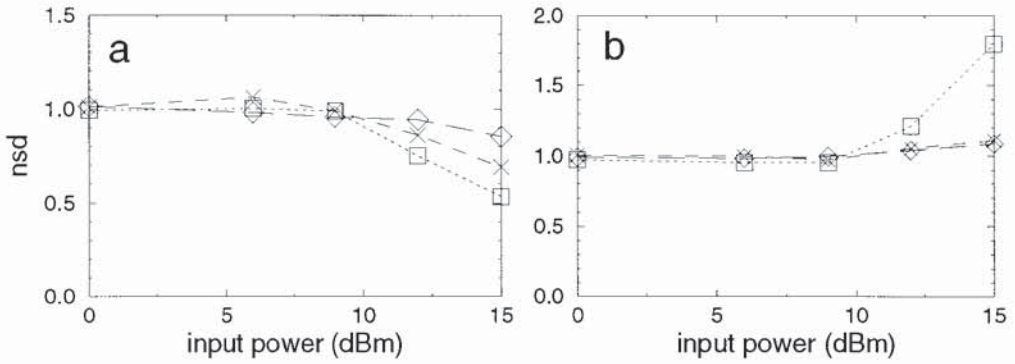

Fig. 4.7: Normalised standard deviation of the simulated SBS backscattered intensity for (a) the dominant and (b) the subsidiary polarisation modes as a function of CW input power and for nonuniform fibre model lengths of 25 m (square, dotted), 100 m (cross, dashed) and 400 m (diamond, long dashed).

In fig. 4.8, the effect of varying L_m between 25 and 400 m on the simulated NFM SBS backscattered and transmitted power characteristics is shown. Apart from the decrease in backscattered power with increasing L_m for the subsidiary polarisation mode at high input powers, there is no significant dependence on L_m for either of the backscattered or transmitted powers. Since the subsidiary mode power is 30 to 40 dB lower than that for the dominant mode at these input powers, the total backscattered power is essentially independent of L_m. The agreement of the simulated SBS backscattered powers with those obtained by numerical integration of the theoretical (undepleted pump) spectral densities obtained for fig. 4.4 is excellent for input powers up to 9 dBm. At 12 dBm, the simulated powers for both polarisation modes are seen to be much smaller than the corresponding theoretical ones due to pump depletion.

The simulated SBS backscattered (dominant polarisation mode only) and transmitted power characteristics for the uniform fibre model at L_m = 496 m are also shown in

fig. 4.8 for comparison with the equivalent NFM characteristics. The difference between the UFM and NFM curves is only noticeable at the lowest input power of 0 dBm at which the backscattered power differs by up to about 1 dB. The reason for this is that at moderate to high input powers, the FWHM bandwidth of the backscattered power spectrum is significantly less than the Brillouin gain FWHM linewidth, so that the regions of the UFM and NFM Brillouin gain spectra (shown in fig. 4.3) close to their peaks, over which agreement is close, have a dominant influence. At low input powers, the bandwidth of the backscattered power spectrum becomes comparable with the Brillouin gain linewidth, so that the regions of the UFM and NFM Brillouin gain spectra further from their peaks, over which the curves start to diverge, have a small but significant influence.

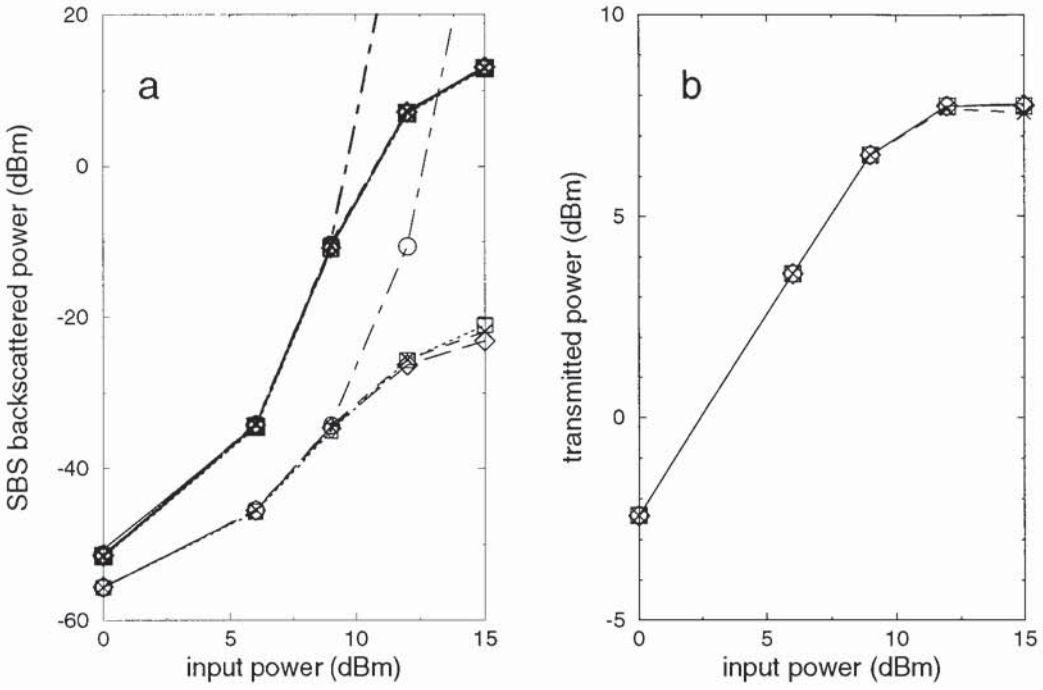

Fig. 4.8: (a) SBS backscattered power for the dominant (bold) and subsidiary (normal) polarisation modes and (b) transmitted power as functions of CW input power from (i) simulation for nonuniform fibre model lengths of 25 m (square, dotted), 100 m (cross, dashed) and 400 m (diamond, long dashed), (ii) undepleted pump theory (circle, dot-dashed in (a), not shown in (b)) and (iii) simulation for a uniform fibre model length of 496 m (normal, solid, shown in (a) for the dominant mode only and in (b)).

From fig. 4.9 (a), it can be seen that the total inferred noise power for the NFM does not vary with L_m over the range 25 to 400 m. However, the nsd of the instantaneous inferred noise power does vary with L_m and input power as shown in fig. 4.9 (b). This implies that, as for the uniform fibre model, inferred noise

simulated at low L_m for higher true fibre lengths may be used for computing detected carrier-to-noise ratios in analogue transmission systems but that greater care is needed for simulating Bit Error Rates of digital baseband systems where the statistical distribution of the noise may be important.

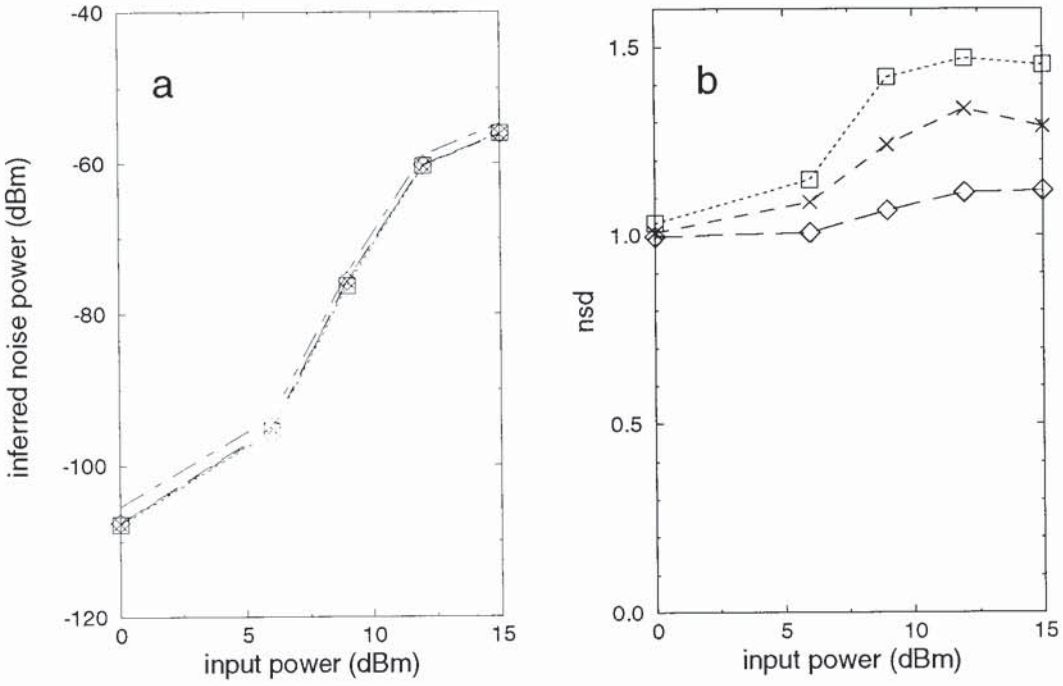

Fig. 4.9: (a) Mean and (b) normalised standard deviation of the inferred SBS noise component power of the simulated transmitted signal as a function of CW input power and for (i) nonuniform fibre model lengths of 25 m (square, dotted), 100 m (cross, dashed) and 400 m (diamond, long dashed), (ii) a uniform fibre model length of 496 m (normal, dot-dashed, shown in (a) only).

The inferred SBS noise power characteristic for the uniform fibre model at L_m = 496 m is also shown in fig. 4.9 for comparison with the equivalent NFM characteristics. The difference between the UFM and NFM inferred noise powers is just over 1 dB at an input power of 15 dBm and increases with decreasing input power to just over 2 dB at 0 dBm. The reason for this is based on the differential equation, (A3.2.4), for the inferred transmitted noise power spectral density, which depends on the convolution of the backscattered power spectrum with the Brillouin gain spectrum. At moderate to high input powers, the FWHM bandwidth of the inferred noise power spectrum is comparable with the Brillouin gain FWHM linewidth, so that the regions of the UFM and NFM Brillouin gain spectra (shown in fig. 4.3) further from their peaks, over which the curves start to diverge, have a small but significant influence. At low input powers, the increase in the UFM

backscattered power relative to that for the NFM of up to 1 dB, noted above in conjunction with fig. 4.8, contributes to the additional difference in the inferred noise powers.

4.6 CONCLUSIONS

The Brillouin shift frequency (BSF) of a single mode optical fibre is known to vary with doping concentrations, residual stresses and temperature. Differences in BSF for light travelling in different parts of the core-cladding cross-section and fluctuations in BSF along the fibre length therefore arise and lead to a broadening of the Brillouin gain spectrum relative to that expected for pure fused silica. In the case of a GeO_2-doped silica core fibre with pure silica cladding, guidance of acoustic longitudinal modes leads to the presence of subsidiary lobes as well as the principal lobe of the Brillouin gain spectrum and to a dependence of the BSF of the main lobe on core radius and the difference in acoustic velocity between core and cladding. As a consequence of the dependence of the BSF on these factors, the Brillouin gain spectrum can vary substantially both in shape and bandwidth from fibre to fibre.

For the development of the predictive computer model, the simplifying assumption has been made that the variation of BSF with distance is a random variable with a Gaussian pdf and a uniform (or white) power spectral distribution. The validity of this assumption has been confirmed for the case of a pure silica fibre with F-doped cladding, for which Brillouin amplified power spectral measurements at a wavelength of 1.55 μm are reported in [4.1.6]. The Brillouin gain spectrum has been derived from these measurements and found to fit a theoretical spectrum consisting of the convolution of a Lorentzian spectrum, having a FWHM bandwidth of about 11 MHz, with a Gaussian probability density function (pdf) of standard deviation equal to 9.5 MHz.

A nonuniform fibre model has been developed by considering the fibre length to be divided into a large number of sections, in each of which the uniform fibre model is applied for a value of BSF specific to that section. A pseudorandom sequence with a Gaussian pdf is generated to represent the BSFs of these sections. Characteristics of mean optical output and backscattered powers as functions of input power for a CW input signal have been simulated using the nonuniform fibre model (NFM) and compared with those from the same experiment as for the uniform fibre model (UFM) comparison in chapter 3. With the NFM end-to-end Brillouin gain linewidth made equal to 42 MHz, the sum of the measured Brillouin gain and laser linewidths, the simulated and experimental characteristics agree very well if the Brillouin gain coefficient, g_B, assumed in each model fibre section of constant BSF is set to $4.72.10^{-11}$ $m.W^{-1}$. The Brillouin gain linewidth in each constant BSF section is assumed to be 13 MHz, corresponding to the sum of the Brillouin gain linewidth assumed for the idealised core material of 11 MHz and the laser linewidth of 2 MHz. The equivalent value predicted from theory for a Brillouin gain linewidth of 13 MHz, a fibre core refractive index of 1.44, an acoustic velocity of $5.81.10^3$ $m.s^{-1}$, corresponding to the measured BSF of 10.88 GHz, and other parameters as for fused silica is $g_B = 5.59.10^{-11}$ $m.W^{-1}$. The discrepancy of 0.7 dB can be explained in terms of errors in the measured loss and Brillouin gain linewidth and differences in the density and photoelastic constant for the GeO_2 doped core compared to those for pure silica.

The theoretical NFM and UFM Brillouin gain coefficient spectra (bgcs), for which the simulated output and backscattered powers fit the same experimental characteristics, are very similar to each other from half to full maximum height, but diverge at lower heights. The peak value of the NFM bgcs is $1.922.10^{-11}$ $m.W^{-1}$, while that for the UFM is $1.943.10^{-11}$ $m.W^{-1}$. The NFM simulated output and backscattered powers are independent of model fibre length in the range investigated of 25 to 400 m. Agreement of the NFM simulated backscattered power characteristic with undepleted pump theory is excellent for input powers up to 9 dBm. The difference between the UFM and NFM curves is only noticeable at the

lowest input power of 0 dBm at which the dominant polarisation mode backscattered powers differ by up to about 1 dB. This divergence at low powers is attributable to the emerging difference in the two Brillouin gain coefficient spectra below half height. For the same reason, the NFM inferred transmitted SBS noise power, also found to be independent of model fibre length in the above range, is about 2 dB lower than that for the UFM at 0 dBm and about 1 dB lower at input powers between 6 and 15 dBm.

The component of the NFM transmitted power spectrum which is dependent on model fibre length exhibits substantially greater fluctuation than that for the UFM. Most of this fluctuation is associated with the simulated longitudinal pattern of BSF variation. It is therefore important to take the average and monitor limits of uncertainty using different seed numbers which initiate the BSF sequence when simulating transmitted power spectra and related system performance measures such as carrier-to-noise ratio with the nonuniform fibre model.

5. MODELLING OF OPTICAL AM CATV LINK PERFORMANCE DEGRADATION FROM SBS

A simplified optical AM CATV link in which the optical carrier is intensity modulated by a single, relatively small subcarrier, corresponding to one unmodulated AM CATV channel, provides an excellent example for applying the SBS model to the prediction of link performance degradation from SBS. The Carrier-to-Noise Ratio (CNR) for such an example has been measured by Mao et al. [1.3.14] as a function of input power and provides a basis for the comparison of simulated and experimental link performance.

In section 5.1, the computer model is extended to include simulation of the intensity modulation of the input carrier by a single subcarrier and to represent the detected photocurrent from a PIN photodiode placed at the output end of the model fibre. The procedure for evaluating the CNR of the subcarrier channel, both at the simulated model fibre length and at much higher lengths, is outlined.

In section 5.2, the CNR arising from transmitted SBS noise is predicted from uniform fibre model (UFM) simulations for the parameters and SBS backscattered power characteristic given in [1.3.14] for the experimental single channel link of Mao et al.. The prediction of CNR at the real fibre length for each input power is based both on the CNR from the component of SBS noise which is independent of model fibre length and also on the rate at which the CNR from the length-dependent component of SBS noise increases with increasing length. The complete modelled CNR for the link takes into account the experimental CNR with the fibre replaced by a linear optical attenuator of the same loss and also the CNR from multipath interference induced by signal double Rayleigh scattering. The complete modelled CNR is then compared with the experimental CNR in the presence of the fibre.

In section 3.3, the complete modelled CNR derived from nonuniform fibre model simulations of SBS is obtained at each input power and compared with the same experimental CNR as above, using a similar procedure to that described in section 3.2. In section 3.4, conclusions are drawn from the comparisons with experiment for the two models.

5.1 SIMULATION OF DETECTED POWER OF TRANSMITTED AM SUBCARRIER MODULATED OPTICAL SIGNAL

The instantaneous power of the transmitted optical signal is given by

$$P_{tr} = P_{in}.|E_{1n}(\zeta=1, \tau)|^2 \qquad (5.1.1)$$
$$= P_{in}.E_{1n}E_{1n}^*,$$

where P_{in} is the input power and E_{1n} is the normalised pump field of (3.1.1) such that $|E_{1n}(\zeta = 0, \tau)|^2$ is equal to unity. The detected photocurrent from a PIN photodiode with a responsivity of r_d is given by

$$I_P = r_d.P_{tr}. \qquad (5.1.2)$$

The power spectrum of the modelled detected photocurrent is estimated in the same way as for the simulated backscattered and transmitted fields, as described at the end of section 3.3.

In optical AM subcarrier modulation, the optical power is amplitude modulated at one or more subcarrier frequencies. The optical modulation index or depth, m_{sc}, for one of these subcarrier channels is defined as the peak amplitude, ΔP_{max}, of the corresponding power modulation divided by the average or unmodulated power, P_{av} [5.1.1], [5.1.2]:

$$m_{sc} = \Delta P_{max}/P_{av}. \qquad (5.1.3)$$

For a single subcarrier of frequency f_{sc}, the modulated optical power launched into the fibre, P_{modin}, may be represented as

$$P_{modin} = P_0 (1 + m_{sc} \cos (2\pi f_{sc} t)), \qquad (5.1.4)$$

and the normalised input field envelope as

$$E_{1n} = \sqrt{(1 + m_{sc} \cos (2\pi f_{sc} t))}$$
$$\approx 1 + (m_{sc}/2) \cos (2\pi f_{sc} t) \text{ for } m_{sc} \ll 1. \qquad (5.1.5)$$

The detected carrier-to-noise ratio (CNR) at f_{sc} is evaluated as

$$CNR = 10 \log10 (P_{fsc}/N_{scrb}) \text{ dB}, \qquad (5.1.6)$$

where P_{fsc} is the sum of the detected powers of the subcarrier at $\pm f_{sc}$ and N_{scrb} is the total detected noise in the subcarrier channel receiver bandwidth centred at $+ f_{sc}$ and $- f_{sc}$.

The simulated CNR obtained as above from the output field $E_{1n}(\zeta=1)$ for a feasible model fibre length, L_m, may be compared, for some cases, with that from an output field $E_{1nhlm}(\zeta=1)$ inferred for very high values of L_m. As discussed in chapter 3, an output field $E_{1xn}(\zeta=1)$, which represents the underlying SBS noise spectrum approached at high L_m, can be simulated at practicable model fibre lengths. When the SBS depleted signal spectrum expected at high L_m can be predicted to consist of a few easily identifiable spectral lines at known frequencies, these can be extracted from the DFT of the output field $E_{1n}(\zeta=1)$ modelled at moderate L_m. The output field $E_{1nhlm}(\zeta=1)$ inferred for high L_m can then be derived from the sum of the DFT of the noise field $E_{1xn}(\zeta=1)$ at all frequencies and the DFT of the total output field $E_{1n}(\zeta=1)$ at the identified signal frequencies. If the optical carrier before subcarrier

modulation is assumed to have negligible spectral linewidth, these relative signal frequencies are 0, + f_{sc} and - f_{sc} for modulation by a single subcarrier, given that the approximation of (5.1.5) is reasonable. The detected CNR predicted for high L_m, CNR_{hlm}, is obtained from $E_{1nhlm}(\zeta=1)$ in the same way as described above for that from $E_{1n}(\zeta=1)$.

5.2 COMPARISON WITH EXPERIMENTAL RESULTS USING UNIFORM FIBRE MODEL

Simulated characteristics of detected CNR for a single AM subcarrier as a function of input power have been compared with that from an experiment by Mao et al. in which the modulation index of the subcarrier at 67.25 MHz is 4% and the CNR is measured in a 4 MHz bandwidth [1.3.14]. Light from a single frequency F-centre laser, assumed from one of their previous papers [2.1.4] to be at 1.55 μm, is passed through a $LiNbO_3$ Mach-Zehnder interferometer amplitude modulator and passive optical components to a 13 km length of dispersion shifted fibre, with an attenuation of 0.31 dB/km and an effective core area of 35 μm^2. The laser linewidth is stated to be narrow but a value is not given. The Brillouin shift frequency and gain linewidth are also not known. However, characteristics of backscattered power as a function of input power are shown in figs. 1 and 4 of [1.3.14] and a characteristic of transmitted power as a function of input power is also given in fig. 1 of this paper.

Simulations of detected CNR have initially been carried out using the uniform fibre model with input parameters chosen to agree with these experimental values wherever possible. The laser linewidth is assumed to be negligible so that no phase noise is imposed on the simulated input carrier before amplitude modulation by the single subcarrier. The value of the Brillouin gain coefficient, g_B, is chosen to give the best fit between the simulated and experimental characteristics of backscattered

power as a function of input power shown in fig. 5.1 and is equal to $1.16.10^{-11}$ $m.W^{-1}$. The Brillouin gain linewidth is evaluated as 60 MHz from (2.1.17) for the parameters of bulk fused silica at a wavelength of 1.55 μm and the fitting value of g_B. The dominant and subsidiary polarisation modes are assumed to have polarisation factors of $\eta_i = 2/3$ and $\eta_o = 1/3$, respectively, as predicted by theory and discussed in section 3.2.

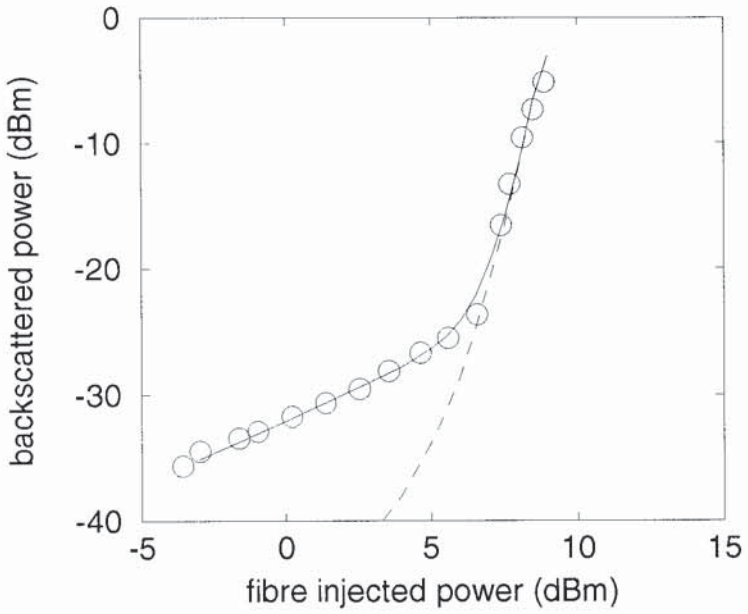

Fig. 5.1: Backscattered power as function of input power from (i) experiment (circles) [1.3.14], (ii) simulation assuming uniform fibre model and including Rayleigh backscattering at -32.2 dB (solid), (iii) simulation of SBS alone (dashed). The carrier is modulated by a single subcarrier at 67.25 MHz with a modulation index of 4%. The experimental fibre length of 13 km is simulated with a model fibre length of 87 m and the same total linear loss of 4 dB.

Characteristics of CNR and CNR_{hlm} as functions of input power have been simulated for different model fibre lengths, L_m, and are shown in fig. 5.2. At low input powers, the CNR curves converge on the CNR_{hlm} curves, which are similar for all L_m, as expected. CNR_{hlm} is in excellent agreement with $CNR_{c\text{-}nxsc}$, which is the ratio of the detected subcarrier power to the component of detected noise power in the subcarrier receiver bandwidth due to the beating of the transmitted field $E_{1n}(\zeta=1)$ at the optical carrier frequency with the inferred transmitted SBS noise field, $E_{1xn}(\zeta=1)$, at frequency bands centred round + f_{sc} and - f_{sc} relative to the optical carrier frequency. An expression for $CNR_{c\text{-}nxsc}$ is derived in Appendix 5.1

and provides a useful output parameter from the simulations for checking the determination of CNR and CNR_{hlm} from the modelled power detection.

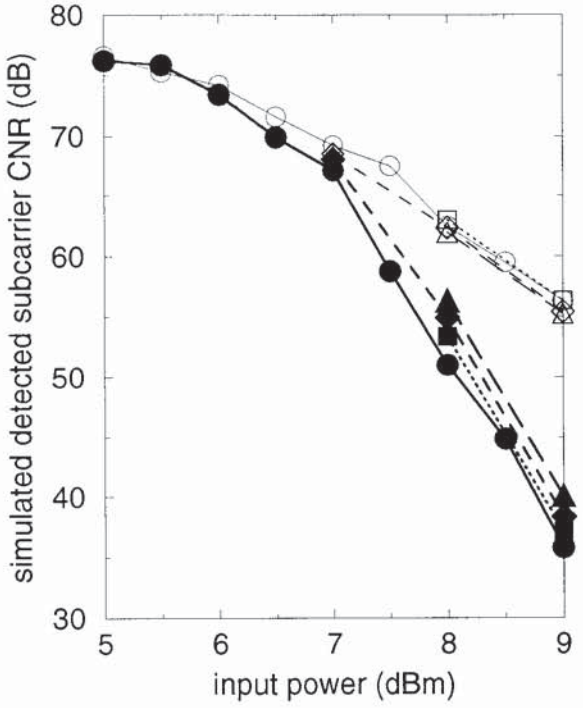

Fig. 5.2: Simulated characteristics, assuming uniform fibre model, of detected subcarrier CNR (filled, bold) and CNR_{hlm} (unfilled, normal), the CNR inferred for high model fibre lengths, as functions of input power for model fibre lengths of (i) 87 m (circles), (ii) 174 m (squares), (iii) 347 m (diamonds), (iv) 695 m (triangles).

At higher input powers, the CNR characteristics of fig. 5.2 are dominated by the component, $N_{sc-n\Delta c}$, of detected noise power in the subcarrier receiver bandwidth due to the beating of the transmitted field $E_{1n}(\zeta=1)$ at + f_{sc} and - f_{sc} relative to the optical carrier frequency with spectral elements of the transmitted field $E_{1n}(\zeta=1)$ at a frequency band centred round the optical carrier frequency. This can be seen in fig. 5.3, which shows the power spectra of the simulated detected photocurrent, the backscattered field, the transmitted field and the inferred transmitted SBS noise field at various input powers and model fibre lengths. For example, the approximately triangular or Δ-shaped, L_m dependent component of the dotted power spectrum of the transmitted field in fig. 5.3c is apparent in reduced form centred round the subcarrier frequencies in the dotted power spectrum of the photocurrent in fig.5.3e.

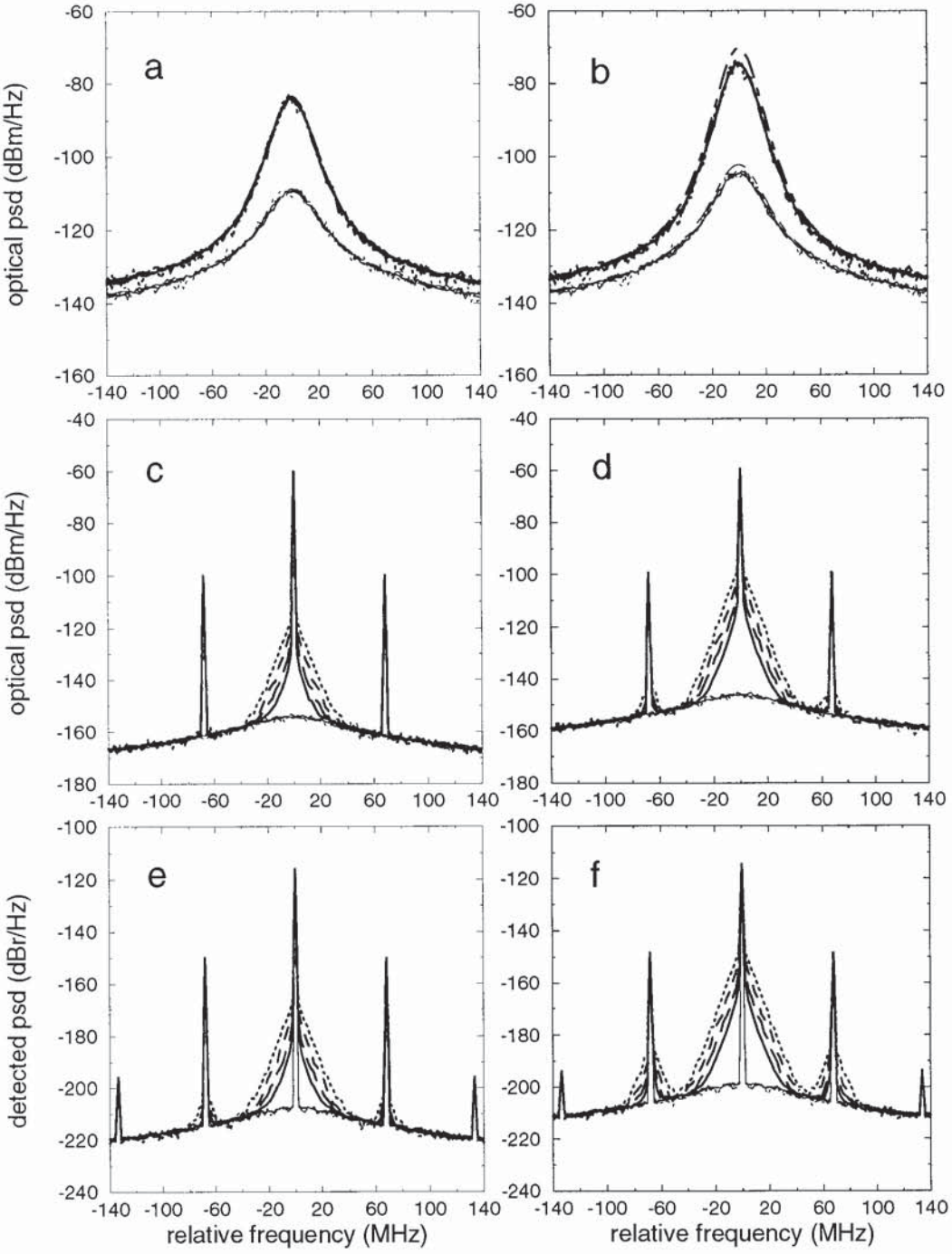

Fig. 5.3: Simulated SBS backscattered power spectra (top (a,b)) for dominant (bold) and subsidiary (normal) polarisation modes, transmitted optical power spectra (middle (c,d), bold) with corresponding inferred noise spectra (middle (c,d), normal) and detected electrical power spectra (bottom (e,f), bold) with corresponding inferred spectra (bottom (e,f), normal) for input powers of 8 dBm (left (a,c,e)) and 9 dBm (right (b,d,f)). Model fibre lengths of 87 m (dotted), 174 m (dashed), 347 m (long dashed) and 695 m (solid) have been simulated. Theoretical SBS backscattered power spectra assuming no pump depletion from SBS (dot-dashed) are also shown in a,b. Each power spectral density (psd) is determined as the average in a bandwidth of 2.3 MHz. Detected electrical psds are expressed in dB relative to 1 A^2/Hz, assuming a photodetector responsivity of 1 A/W. A uniform fibre model has been assumed with a Brillouin linewidth of 60 MHz and a SBS gain coefficient of 1.16. 10^{-11} m.W^{-1}. The fibre loss is equivalent to that for 13 km at 0.31 dB/km.

Another detected noise component, $N_{c-n\Delta sc}$, is expected as a result of the Δ-shaped, L_m dependent spectral elements which appear in the subcarrier sidebands of the

transmitted field power spectrum, as illustrated in fig. 5.3d, in association with the similar shaped element centred round the carrier. The CNR arising only from the L_m dependent detected noise components, $N_{sc-n\Delta c}$ and $N_{c-n\Delta sc}$, may be determined as the excess CNR, CNR_{exc}, from the overall simulated detected CNR, CNR_{ov}, and the CNR inferred at high L_m, CNR_{hlm}, using the relation

$$CNR_{exc} = -10 \log\{10^{-(CNR_{ov}/10)} - 10^{-(CNR_{hlm}/10)}\} \text{ dB.} \qquad (5.2.1)$$

In fig. 5.4, CNR_{exc} is plotted as a function of L_m at input powers of 8 and 9 dBm for the average, maximum and minimum of the simulated values for different thermal noise sequences, together with the best straight line fit used for predicting CNR_{exc} at the real fibre length, L_r, as CNR_{exclr}. On the assumption that this rate of increase remains constant for values of L_m up to L_r = 13 km, CNR_{exclr} is given by

$$CNR_{exclr} = CNR_{exclm0} + R_{pl} \log_{10}(L_r/L_{m0}) \text{ dB,} \qquad (5.2.2)$$

where CNR_{exclm0} is the excess CNR at $L_m = L_{m0}$ and R_{pl} is a measure of the rate of increase of CNR_{exc} with L_m for a given input power. From the straight line fits of fig. 5.4, CNR_{exclm0} = 51.7 dBm for L_{m0} = 87 m and R_{pl} = 6.8 at an input power of 8 dBm, while CNR_{exclm0} = 35.6 dBm for L_{m0} = 87 m and R_{pl} = 5 at an input power of 9 dBm.

The CNR from SBS depletion at the real fibre length is then

$$CNR_{sbs,lr} = -10 \log\{10^{-(CNR_{exclr}/10)} + 10^{-(CNR_{hlm}/10)}\} \text{ dB.} \qquad (5.2.3)$$

In fig. 5.5, $CNR_{sbs,lr}$, CNR_{exclr} and CNR_{hlm} are shown as functions of input power. Values of CNR_{exclr} at input powers of 8.5 dBm and 7.5 dBm have been obtained by using (5.2.2) with R_{pl} interpolated from the figures given above at 8 and 9 dBm, so that R_{pl} = 6 at 8.5 dBm and R_{pl} = 7 at 7.5 dBm. Approximate upper and lower estimated limits for $CNR_{sbs,lr}$ for input powers between 8 and

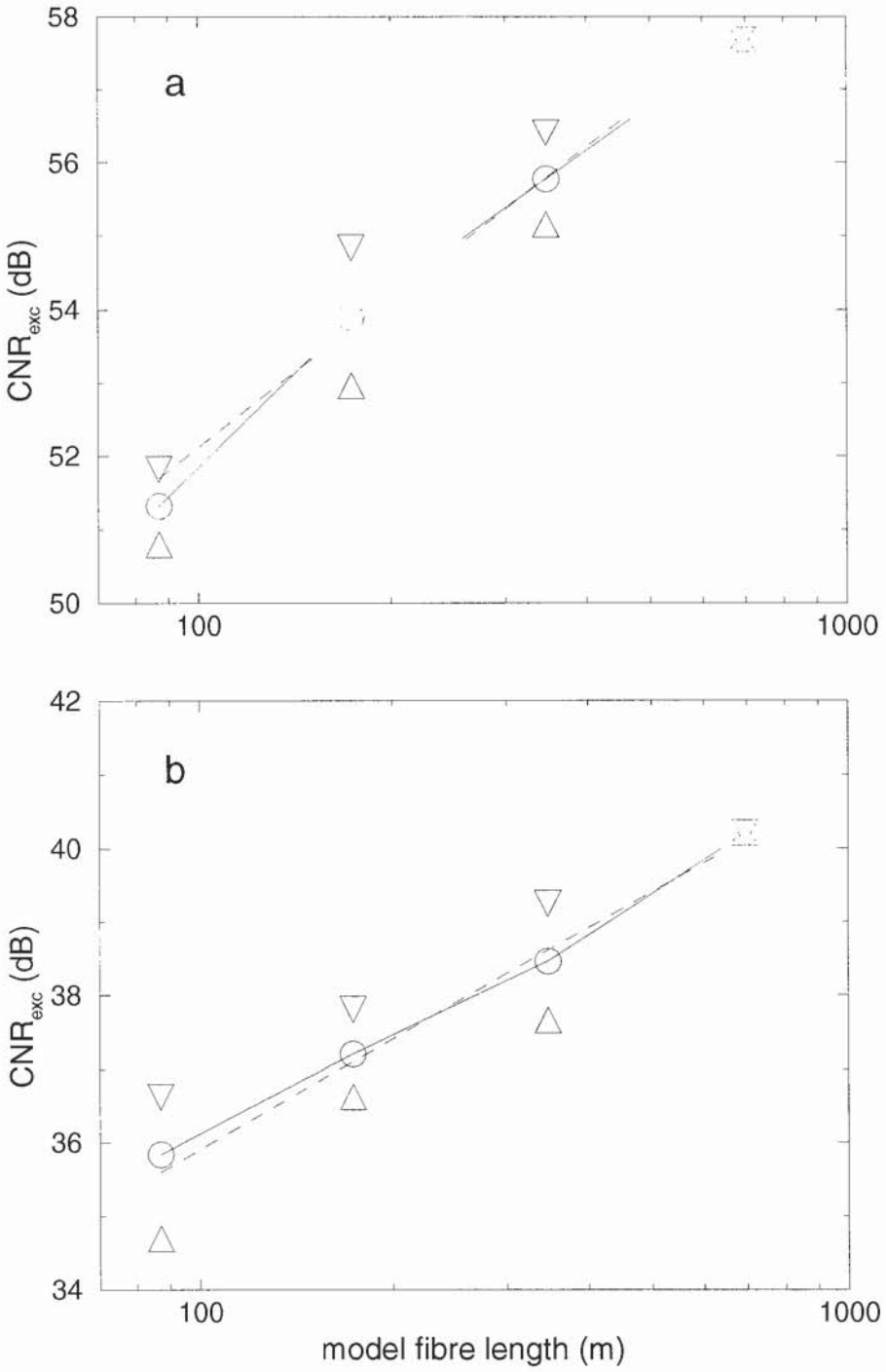

Fig. 5.4: Simulated characteristics, assuming uniform fibre model, of detected subcarrier excess CNR (in dB) as a function of model fibre length (log scale) for input powers of (a) 8 dBm and (b) 9 dBm. Excess CNR is that for which the noise is the difference between that for the full simulated CNR and that for the simulated CNR inferred at high model fibre lengths (see text). The average (circles), maximum (downward triangles) and minimum (upward triangles) of the simulated values for different thermal noise sequences are shown together with the best straight line fit (dashed) used for predicting excess CNR at the true fibre length.

9 dBm are also shown in fig. 5.5, corresponding mainly to uncertainties in the prediction slope R_{pl}, but also to scatter on the simulated values of CNR_{exclm0} and CNR_{hlm}.

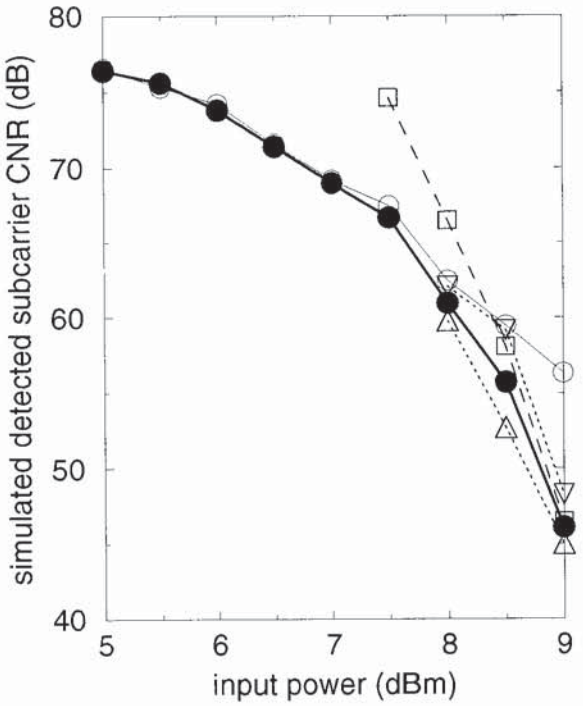

Fig. 5.5: Simulated characteristics, assuming uniform fibre model, of detected subcarrier CNR ($CNR_{sbs,lr}$) (filled circles, bold solid) with estimated upper (downward triangles, dotted) and lower (upward triangles, dotted) limits together with excess CNR (CNR_{exclr}) (unfilled squares, dotted), both predicted for the true fibre length, and CNR_{hlm} (unfilled circles, normal solid), the CNR inferred for very high model fibre lengths, as functions of input power.

In order to compare the modelled and experimental CNRs, the characteristic shown in fig. 3 of [1.3.14] of CNR measured in the absence of the 13 km fibre as a function of received power plus linear fibre loss is used to obtain the effective linear CNR of the link, CNR_{lin}, at each input power. CNR_{lin} is reproduced in fig. 5.6 together with the experimental CNR measured in the presence of the fibre, CNR_{expf}, and the CNR derived from simulated SBS, $CNR_{sbs,lr}$. If only CNR_{lin} and $CNR_{sbs,lr}$ are included in the calculation of modelled CNR, the disagreement between modelled and experimental CNRs is very noticeable, particularly for input powers between 6 and 8 dBm. The most likely explanation for this is that multipath interference (MPI) induced by signal double Rayleigh scattering (SDRS) is present [1.3.17].

In this effect, Rayleigh backscattered light from the transmitted signal is again backscattered so that it travels alongside the original signal and interferes with it. If the transmitted optical carrier is perturbed by any phase noise, interference gives rise

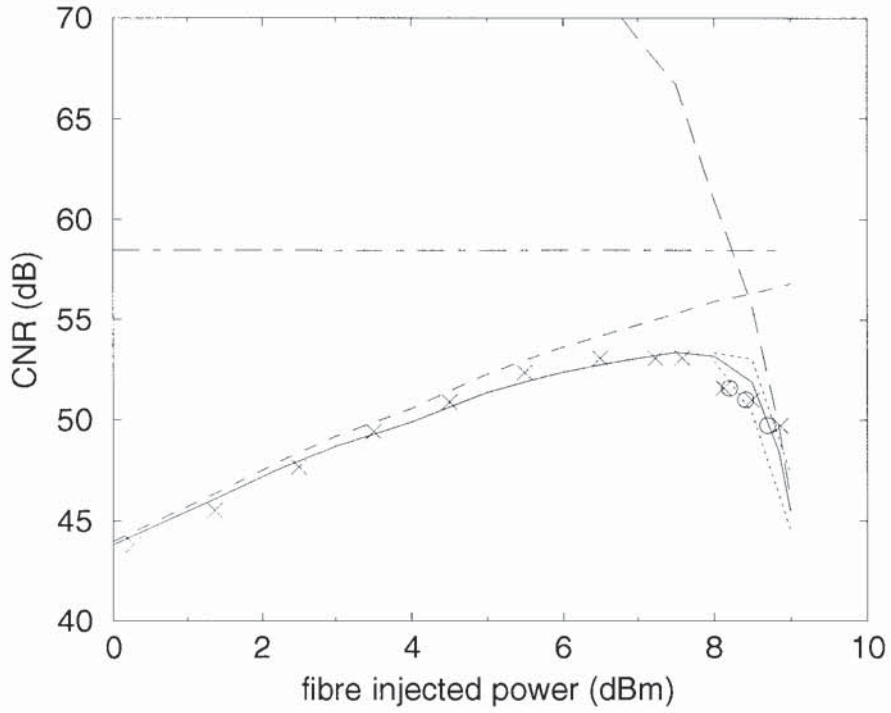

Fig. 5.6: Experimental and simulated characteristics, assuming uniform fibre model, of detected subcarrier CNR as functions of input power: (i) experimental with 13 km fibre (crosses) together with (ii) experimental points for which the input power has been adjusted such that experimental backscattered power points in fig. 5.1 would line up with the simulated backscattered power curve, (iii) experimental with linear attenuator instead of fibre (dotted), (iv) simulated SBS (dashed), (v) assumed level of CNR from multipath interference (MPI) induced by signal double Rayleigh scattering (SDRS) (dot-dashed), and (vi) total predicted CNR from experimental linear optical link, simulated SBS and MPI (solid) with (vii) estimated upper and lower limits (dotted) corresponding to limits on simulated SBS shown in fig. 5.5 (but omitted here for clarity).

to amplitude noise. This amplitude noise may be quantified as a detected noise power spectral density relative to the detected signal power for the unmodulated optical carrier, known as the Relative Intensity Noise due to MPI, RIN_{mpi}. Willems et al. have developed an approximate expression for RIN_{mpi} when a laser with an unmodulated FWHM linewidth of $\Delta\nu_L$ is frequency modulated (or "dithered") to give a modulated linewidth of $\Delta\nu_D$ [1.3.17]:

$$RIN_{mpi}(\Delta\nu_D) \approx (2R_{eff}^2/\pi\Delta\nu_D)[\arctan((f + \Delta\nu_D)/\Delta\nu_L) - \arctan((f - \Delta\nu_D)/\Delta\nu_L)], \qquad (5.2.4)$$

where f is the subcarrier frequency and R_{eff} is the geometric mean of the power reflection coefficients of the mirrors that form an optical cavity. For a single subcarrier with modulation index m_{sc} and detection bandwidth B, the CNR due to MPI, CNR_{mpi}, is given by

$$CNR_{mpi} = 10 \log_{10}[m_{sc}^2/(2\ RIN_{mpi}\ B)]\ dB. \qquad (5.2.5)$$

A very approximate estimate of RIN_{mpi} due to signal double Rayleigh scattering (SDRS) may be obtained by letting R_{eff} = -32.2 dB, the ratio of Rayleigh backscattered power to input power found to fit the experimental characteristic of fig. 5.1. For f = 67.25 MHz, m_{sc} = 4%, B = 4 MHz, and $\Delta\nu_D = \Delta\nu_L$ = 1 MHz, (5.2.4) yields RIN_{mpi} = -159.9 dB/Hz and, from (5.2.5), CNR_{mpi} = 62.9 dB. For $\Delta\nu_D = \Delta\nu_L$ = 2 MHz, CNR_{mpi} = 59.9 dB. Although the linewidth of the F-centre laser used in the experiment of [1.3.14] is not stated, except as being narrow, it seems plausible that it could have been of the order of 1 to 2 MHz, so that a CNR_{mpi} of about 60 dB is possible.

The overall modelled CNR is therefore taken to be given by

$$CNR_{mod} = -10 \log\{10^{-(CNR_{sbs,lr}/10)} + 10^{-(CNR_{lin}/10)} + 10^{-(CNR_{mpi}/10)}\}\ dB, \qquad (5.2.6)$$

where a constant value of CNR_{mpi} = 58.5 dB is chosen to give the best fit of the modelled CNR to the experimental CNR in the presence of the fibre, particularly for input powers between 6 and 7.5 dBm, at which the contribution from SBS is expected to be relatively small. The laser linewidth expected from (5.2.4) and (5.2.5) to give this value of CNR_{mpi} is 2.8 MHz.

The agreement between the modelled and experimental CNR characteristics of fig. 5.6 is good over all of the input power range, including the region in which SBS becomes dominant. However, the rate of decrease of CNR with input power between 8 and 9 dBm for the experimental points seems less rapid than for the modelled curve. This is consistent with the fact that the rate of increase of backscattered power with input power between 8 and 9 dBm, as shown in fig. 5.1, is less pronounced for the experimental points than for the modelled characteristic.

This trend has been confirmed by simulating the backscattered power at input powers higher than 9 dBm and comparing the simulated characteristic with the experimental points of fig. 1 of [1.3.14]. The comparison is not shown here, but indicates that the simulated backscattered power is a few dBs greater than for the experiment at higher input powers. A plausible explanation for the discrepancy has not been identified.

In order to illustrate the correlation between the disagreement of the experimental and modelled CNR characteristics of fig. 5.6 at input powers between 8 and 9 dBm and that of the corresponding backscattered power characteristics of fig. 5.1, modified experimental CNR points are also shown in fig. 5.6 for which the input power has been adjusted such that similarly translated experimental backscattered power points in fig. 5.1 would line up with the simulated backscattered power curve. These modified experimental CNR points agree well with the modelled CNR characteristic within the upper and lower limits of uncertainty indicated.

5.3 COMPARISON WITH EXPERIMENTAL RESULTS USING NONUNIFORM FIBRE MODEL

Simulations of detected CNR have been carried out using the nonuniform fibre model for comparison with the same experimental results as above. The Brillouin gain linewidth for each section of constant Brillouin shift frequency (BSF) has been assumed to be 11 MHz, as determined in the previous chapter for pure silica. The Brillouin gain coefficient, g_B, for each section is evaluated as $6.32.10^{-11}$ $m.W^{-1}$ from (2.1.17) for the parameters of bulk fused silica at a wavelength of 1.55 μm and the Brillouin gain linewidth of 11 MHz. The standard deviation of the BSF, σ_{BSF}, is chosen to give the best fit between the simulated and experimental characteristics of backscattered power as a function of input power shown in fig. 5.7 and is equal to 35.1 MHz. From the theoretical Brillouin gain coefficient spectrum (bgcs) shown in fig. 5.8, it can be seen that the peak bgcs and bgcs

linewidth for the nonuniform fibre model are $1.10.10^{-11}$ m.W^{-1} and 88.7 MHz, respectively, compared to $1.16.10^{-11}$ m.W^{-1} and 60 MHz as described in the last section for the uniform fibre model.

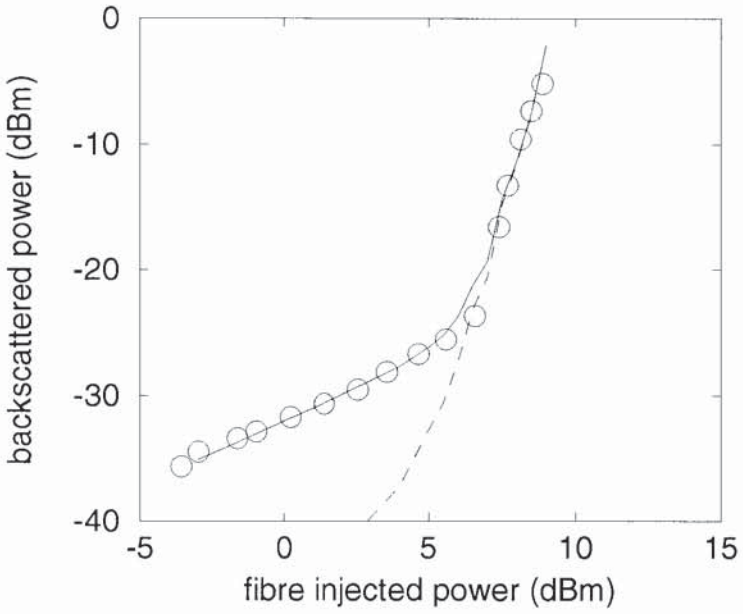

Fig. 5.7: Backscattered power as function of input power from (i) experiment (circles) [1.3.14], (ii) simulation assuming nonuniform fibre model and including Rayleigh backscattering at -32.2 dB (solid), (iii) simulation of SBS alone (dashed). The carrier is modulated by a single subcarrier at 67.25 MHz with a modulation index of 4%. The experimental fibre length of 13 km is simulated with a model fibre length of 120 m and the same total linear loss of 4 dB.

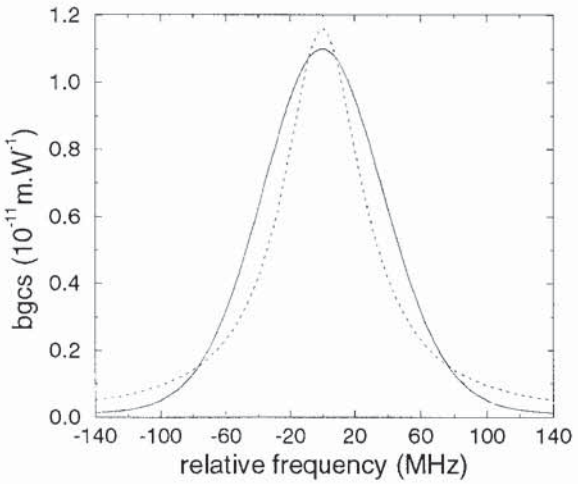

Fig. 5.8: Comparison of theoretical Brillouin gain coefficient spectra (bgcs) for nonuniform (solid) and uniform (dotted) fibre models. For the nonuniform model, $g_B = 6.32.10^{-11}$ m.W-1 and $\Delta\nu_B$ = 11 MHz in each section of constant BSF and the standard deviation of longitudinal BSF variations is 35.1 MHz.

Characteristics of CNR and CNR_{hlm} as functions of input power have been simulated for different model fibre lengths, L_m, and are shown in fig. 5.9. At low

input powers, the CNR curves converge on the CNR_{hlm} curves, which are similar for all L_m, as expected.

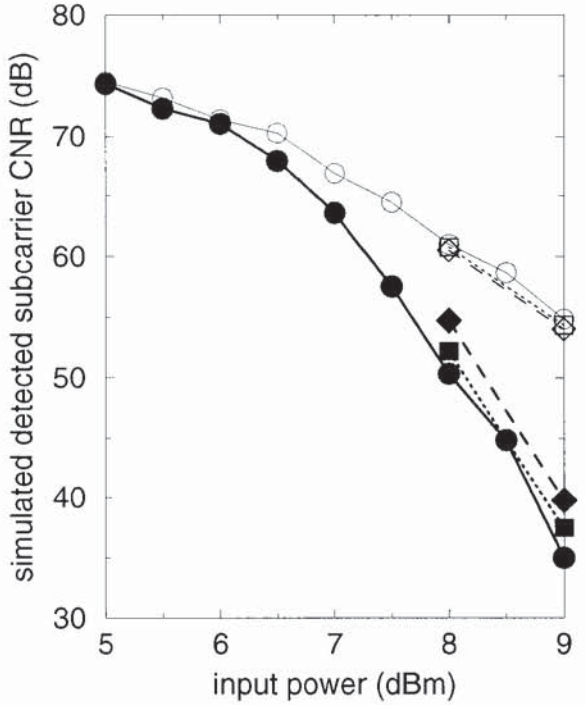

Fig. 5.9: Simulated characteristics assuming nonuniform fibre model of detected subcarrier CNR (filled, bold) and CNR_{hlm} (unfilled, normal) as functions of input power for model fibre lengths of (i) 120 m (circles), (ii) 241 m (squares), (iii) 482 m (diamonds).

As for the uniform fibre model, the CNR characteristics of fig. 5.9 at higher input powers are dominated by the component, $N_{sc-n\Delta c}$, of detected noise power in the subcarrier receiver bandwidth due to the beating of the transmitted field $E_{1n}(\zeta=1)$ at $+ f_{sc}$ and $- f_{sc}$ relative to the optical carrier frequency with spectral elements of the transmitted field $E_{1n}(\zeta=1)$ at a frequency band centred round the optical carrier frequency. This can be seen in fig. 5.10, which shows the power spectra of the simulated detected photocurrent, the backscattered field, the transmitted field and the inferred transmitted SBS noise field at various input powers and model fibre lengths. For example, the approximately triangular or Δ-shaped, L_m dependent component of the dotted power spectrum of the transmitted field in fig. 5.10d is just detectable in reduced form, as a slight rise in the spectral levels, centred round the subcarrier frequencies in the dotted power spectrum of the photocurrent in fig.5.10f.

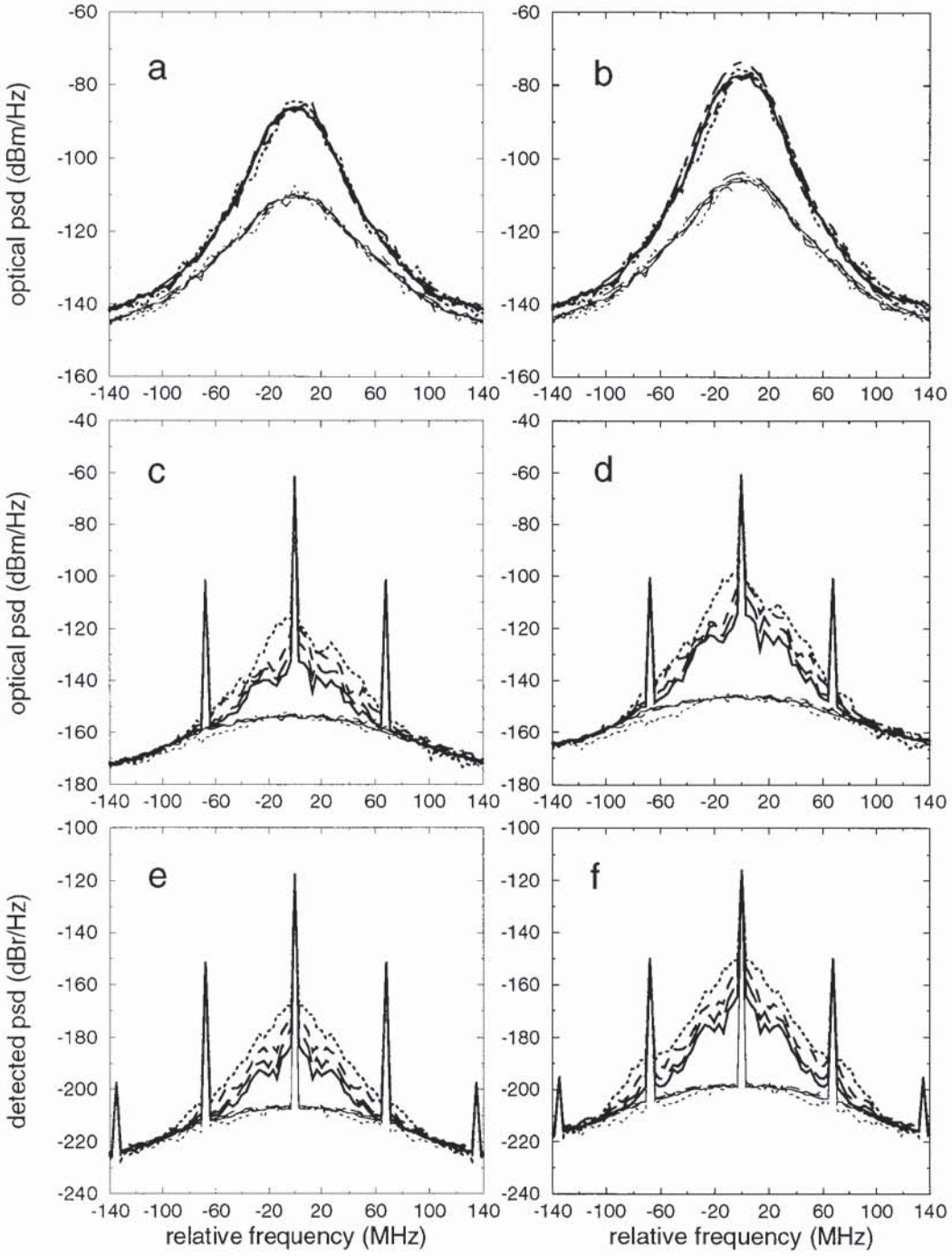

Fig. 5.10 : Simulated SBS backscattered power spectra (top (a,b)) for dominant (bold) and subsidiary (normal) polarisation modes, transmitted optical power spectra (middle (c,d), bold) with corresponding inferred noise spectra (middle (c,d), normal) and detected electrical power spectra (bottom (e,f), bold) with corresponding inferred spectra (bottom (e,f), normal) for input powers of 8 dBm (left (a,c,e)) and 9 dBm (right (b,d,f)). Model fibre lengths of 60 m (dotted), 120 m (dashed), 241 m (long dashed) and 482 m (solid) have been simulated. Theoretical SBS backscattered power spectra assuming no pump depletion from SBS (dot-dashed) are also shown in a,b. Each power spectral density (psd) is determined as the average in a bandwidth of 3.4 MHz. Detected electrical psds are expressed in dB relative to 1 A^2/Hz, assuming a photodetector responsivity of 1 A/W. A nonuniform fibre model has been assumed with parameters such that the theoretical Brillouin gain coefficient spectrum (bgcs) is as shown in fig. 5.8 with an effective linewidth of 88.7 MHz and a peak bgcs of 1.10. 10^{-11} $m.W^{-1}$. The fibre loss is equivalent to that for 13 km at 0.31 dB/km.

Another detected noise component, $N_{c-n\Delta tsc}$, is expected as a result of the tails of the Δ-shaped, L_m dependent part of the transmitted field power spectrum centred at

the optical carrier frequency, since the power spectral densities (PSDs) of these tails are significantly greater at the subcarrier sidebands than those of the inferred SBS noise for the simulated model fibre lengths, as illustrated in fig. 5.10d. The CNR for the $N_{c-n\Delta tsc}$ detected noise component alone, $CNR_{exctail}$, has been estimated by assessing the background levels of the detected PSDs of these tails at the subcarrier frequencies for each value of L_m and comparing these with those of the inferred SBS noise.

As for the uniform fibre model, the CNR arising only from the L_m dependent detected noise components may be determined as the excess CNR, CNR_{exc}, from the overall simulated detected CNR, CNR_{ov}, and the CNR inferred at high L_m, CNR_{hlm}, using (5.2.1). The CNR arising only from the L_m dependent detected noise components apart from $N_{c-n\Delta tsc}$ may be determined as CNR_{exc0} from CNR_{exc} and $CNR_{exctail}$ using the relation

$$CNR_{exc0} = -10 \log\{10^{-(CNR_{exc}/10)} - 10^{-(CNR_{exctail}/10)}\} \text{ dB}. \quad (5.3.1)$$

In fig. 5.11, $CNR_{exctail}$, CNR_{exc0} and CNR_{exc} are plotted as functions of L_m at an input power of 9 dBm for the same thermal noise and Brillouin shift frequency (BSF) longitudinal variation sequences, together with the best straight line fit for CNR_{exc}. Since $CNR_{exctail}$ is about 6 to 8 dB larger than CNR_{exc0} and since their rates of increase with L_m are similar, it seems reasonable not to attempt to predict $CNR_{exctail}$ and CNR_{exc0} at the real fibre length separately, but only CNR_{exc}.

In fig. 5.12, CNR_{exc} is plotted as a function of L_m at input powers of 8 and 9 dBm for the average, maximum and minimum of the simulated values for different thermal noise and BSF sequences. In addition, values of CNR_{exc} for two seeds defining these sequences are shown, together with the corresponding best straight line fits. These straight line fits are used for predicting approximate maximum and minimum limits for the excess CNR at the true fibre length, CNR_{exclr}.

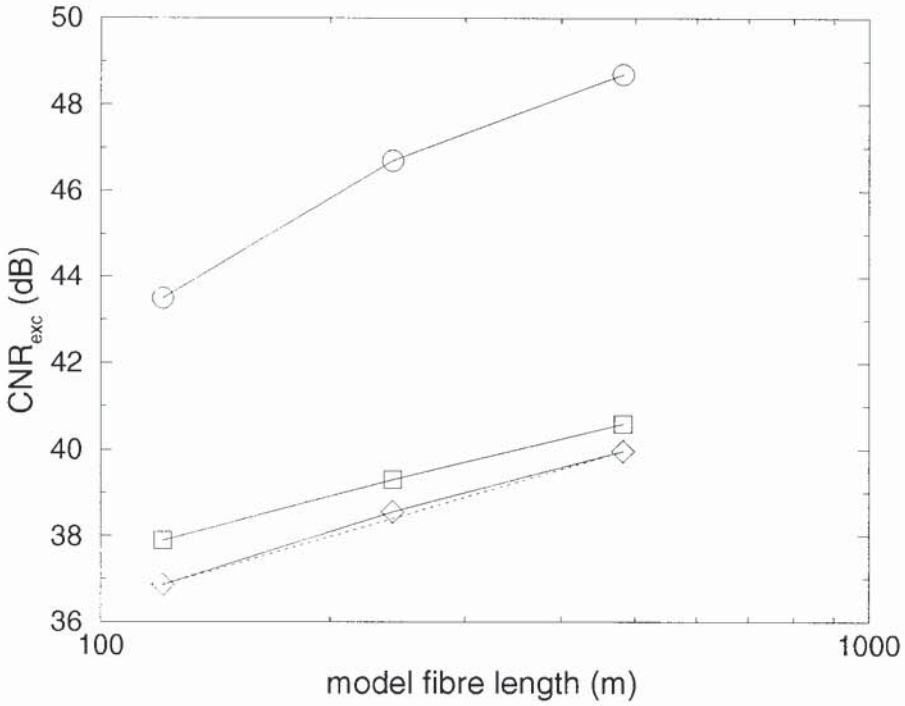

Fig. 5.11: Simulated characteristics, assuming nonuniform fibre model, of detected subcarrier excess CNR and excess CNR components (in dB) as functions of model fibre length (log scale) for an input power of 9 dBm: (i) $CNR_{exctail}$ (circles, solid), the component arising from the tails of the 'triangular' transmitted field spectrum centred at the carrier frequency, (ii) CNR_{exc0} (squares, solid), the component arising from the centres of the 'triangular' transmitted field spectra centred at the carrier frequency, f_c, and also at $f_c \pm f_{sc}$, where f_{sc} is the subcarrier frequency, and (iii) CNR_{excs} (diamonds, solid), the overall excess CNR from these two components, together with a straight line fit (dotted). The overall excess CNR is that for which the noise is the difference between that for the full simulated CNR and that for the simulated CNR inferred at high model fibre lengths (see text). These simulated values have been obtained for the same thermal noise and Brillouin shift frequency longitudinal variation sequences.

The CNR from SBS depletion at the real fibre length, $CNR_{sbs,lr}$, is calculated from CNR_{exclr} and CNR_{hlm} using (5.2.3). In fig. 5.13, $CNR_{sbs,lr}$, CNR_{exclr} and CNR_{hlm} are shown as functions of input power. In fig. 5.14, the experimental CNR measured in the presence of the fibre, CNR_{expf}, is compared with the total predicted CNR from the experimental linear optical link, simulated SBS and MPI. In order to illustrate the correlation between the disagreement of the experimental and modelled CNR characteristics of fig. 5.14 at input powers between 8 and 9 dBm and that of the corresponding backscattered power characteristics of fig. 5.7, modified experimental CNR points are also shown in fig. 5.14 for which the input power has been adjusted such that similarly translated experimental backscattered power points in fig. 5.7 would line up with the simulated backscattered power curve. These modified experimental CNR points agree well with the modelled CNR

characteristic taking into account the approximate upper and lower limits of uncertainty indicated.

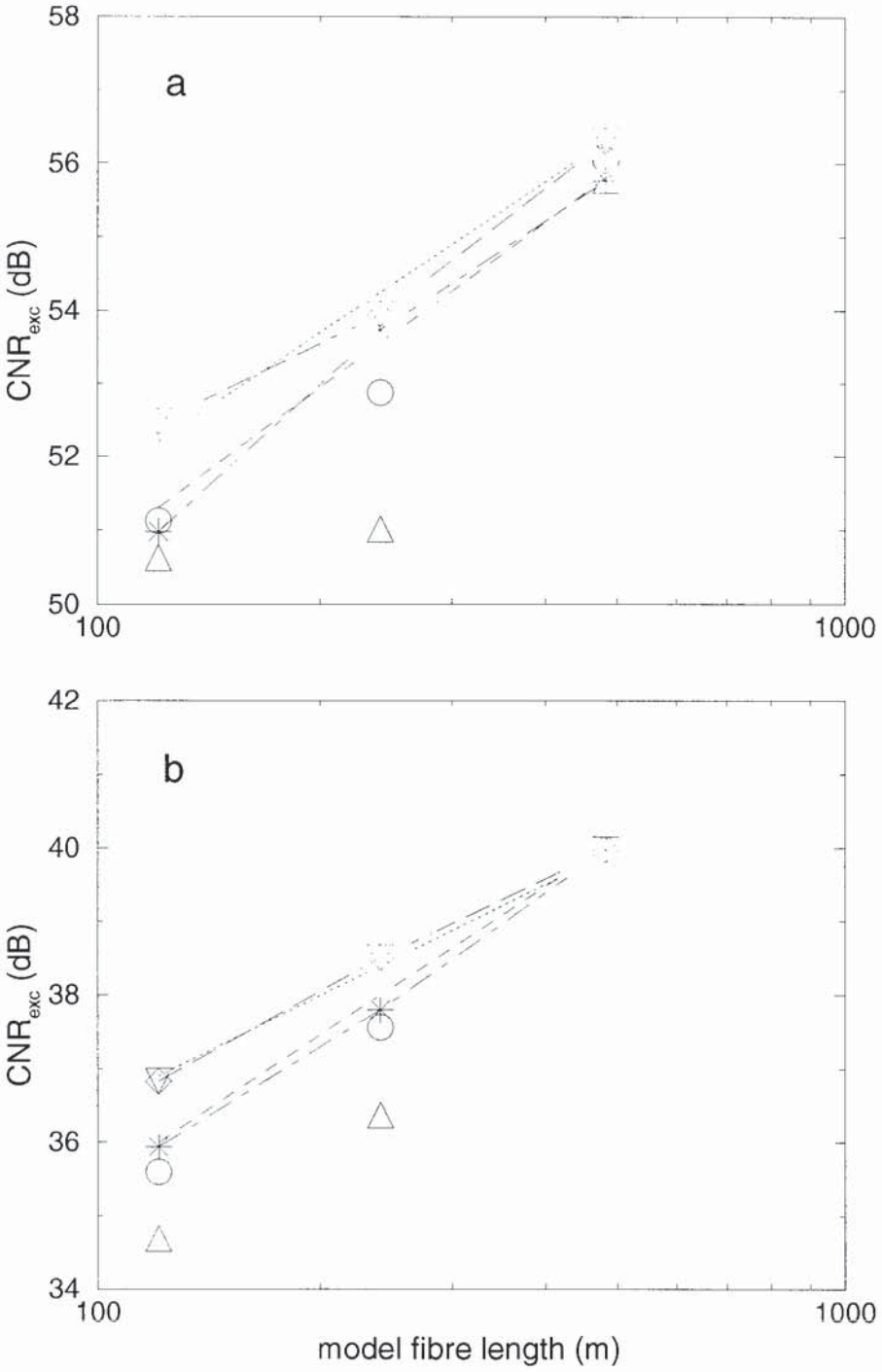

Fig. 5.12: Simulated characteristics, assuming nonuniform fibre model, of detected subcarrier excess CNR (in dB) as a function of model fibre length (log scale) for input powers of (a) 8 dBm and (b) 9 dBm. Excess CNR is that for which the noise is the difference between that for the full simulated CNR and that for the simulated CNR inferred at high model fibre lengths (see text). The average (circles), maximum (downward triangles) and minimum (upward triangles) of the simulated values for different thermal noise and Brillouin shift frequency longitudinal variation sequences are shown. Values for two seeds defining these sequences are shown as diamonds with long dashed lines and asterisks with dot-dashed lines, together with the corresponding best straight line fits (dotted for diamonds, dashed for asterisks) used for predicting approximate limits for the excess CNR at the true fibre length.

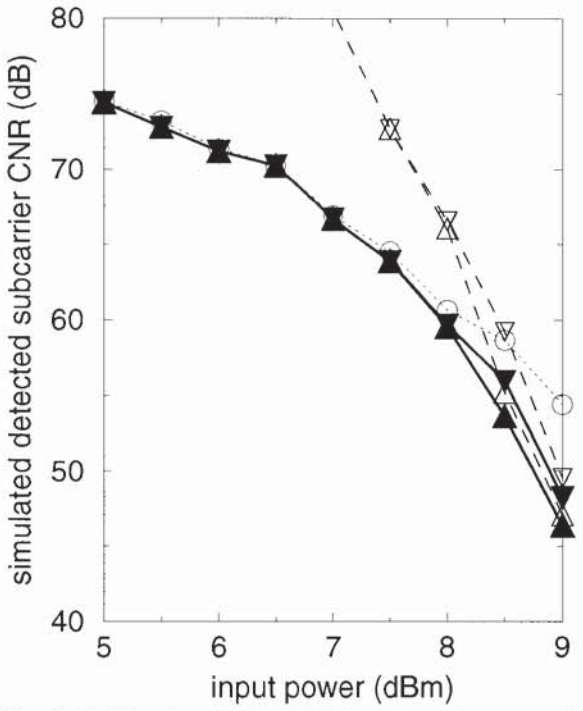

Fig. 5.13: Simulated characteristics, assuming nonuniform fibre model, of detected subcarrier CNR (bold solid, filled triangles: downward for maximum, upward for minimum) and excess CNR (dashed, unfilled triangles: downward for maximum, upward for minimum), both predicted for the true fibre length, and CNR_{hlm} (unfilled circles, dotted), the CNR inferred for very high model fibre lengths, as functions of input power.

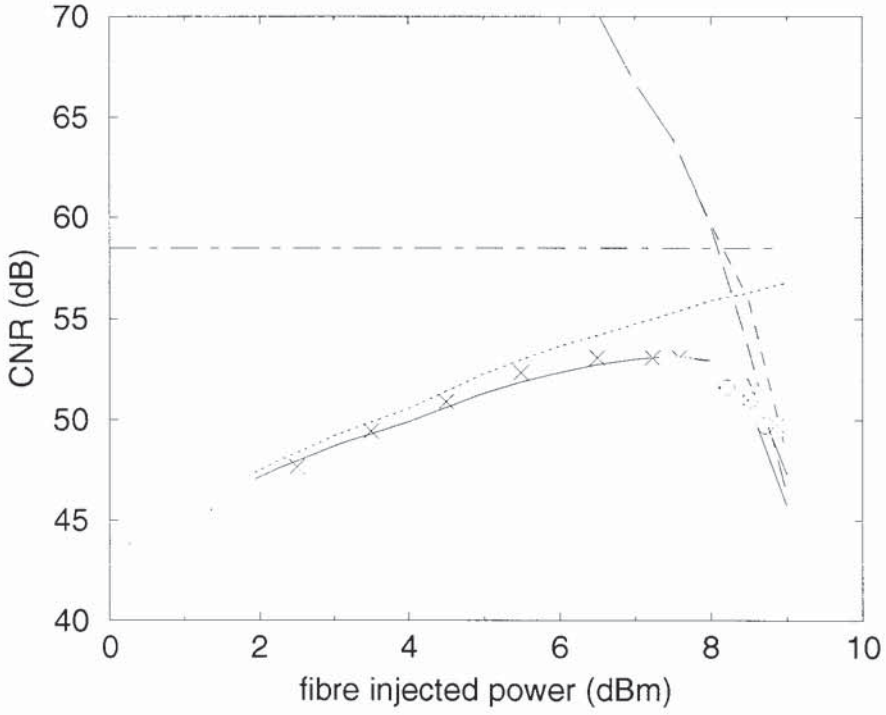

Fig. 5.14: Experimental and simulated characteristics, assuming nonuniform fibre model, of detected subcarrier CNR as functions of input power: (i) experimental with 13 km fibre (crosses), together with (ii) experimental points (circles) for which the input power has been adjusted such that experimental backscattered power points in fig. 5.7 would line up with the simulated backscattered power curve, (iii) experimental with linear attenuator instead of fibre (dotted), (iv) simulated SBS (maximum: dashed, minimum: long dashed), (v) assumed level of CNR from multipath interference (MPI) induced by signal double Rayleigh scattering (SDRS) (dot-dashed), and (vi) total predicted CNR from experimental linear optical link, simulated SBS and MPI (maximum and minimum: solid).

5.4 CONCLUSIONS

The computer model has been extended to include simulation of the detected photocurrent from a PIN photodiode placed at the output end of the model fibre. The input field envelope is modified to represent intensity modulation of the input carrier by a single subcarrier at a modulation index of m_{sc} and a frequency of f_{sc}. The carrier-to-noise ratio (CNR) of the detected subcarrier channel is evaluated from the simulated electrical power spectrum of the detected photocurrent. The optical output field spectrum inferred for high model fibre lengths, L_m, is constructed from the full optical output field spectral lines at frequencies of 0 and $\pm f_{sc}$ relative to that of the optical carrier and from the transmitted SBS optical noise field spectrum inferred for high L_m. The carrier-to-noise ratio inferred for high L_m (CNR_{hlm}) of the detected subcarrier channel is evaluated from the simulated electrical power spectrum of the detected photocurrent derived from the constructed "inferred" optical output field spectrum.

Characteristics of detected CNR for a single AM subcarrier as a function of input power have been simulated using both the uniform and nonuniform fibre models (UFM and NFM) and compared with that from an experiment by Mao et al. in which the modulation index of the subcarrier at 67.25 MHz is 4% and the CNR is measured in a 4 MHz bandwidth [1.3.14]. For the UFM, the Brillouin gain coefficient, g_B, is chosen to give the best fit between the simulated and experimental characteristics of backscattered power as a function of input power and is equal to $1.16.10^{-11}$ $m.W^{-1}$. The Brillouin gain linewidth is evaluated as 60 MHz from theory for the parameters of bulk fused silica at a wavelength of 1.55 μm and the fitting value of g_B.

For input powers of 8 and 9 dBm, and model fibre lengths between 87 and 695 m, the CNR arising only from the L_m dependent detected noise components has been determined as the excess CNR, CNR_{exc}, from the overall simulated detected CNR, CNR_{ov}, and the CNR inferred at high L_m, CNR_{hlm}. The graphs of excess CNR as

a function of model fibre length have been used to predict values of CNR_{exc} and hence CNR_{ov} at the real fibre length of 13 km for these and other input powers.

As well as including the CNR from SBS, the total predicted CNR, CNR_{tp}, takes into account the experimental CNR, CNR_{lin}, with the fibre replaced by a linear optical attenuator of the same loss and also the CNR from multipath interference induced by signal double Rayleigh scattering, CNR_{mpi}. CNR_{mpi} is chosen as 58.5 dB to give the best fit of the total predicted CNR to the experimental CNR in the presence of the fibre, particularly for input powers between 6 and 7.5 dBm, at which the contribution from SBS is relatively small. The laser linewidth calculated from theory to give this value of CNR_{mpi} is 2.8 MHz.

Agreement between the total predicted CNR, based on UFM simulation of SBS, and the experimental CNR in the presence of the fibre is good. The predicted CNR corresponds even better with modified experimental CNR points, for which the input power has been adjusted such that similarly translated experimental backscattered power points would line up with the UFM simulated backscattered power curve.

For the NFM simulations of detected CNR, the Brillouin gain linewidth for each section of constant Brillouin shift frequency (BSF) has been assumed to be 11 MHz, as determined in the previous chapter for pure silica. For this Brillouin gain linewidth, the Brillouin gain coefficient, g_B, for each section is evaluated as $6.32.10^{-11}$ $m.W^{-1}$ from theory for the parameters of bulk fused silica at a wavelength of 1.55 μm. With the standard deviation of the BSF chosen to give the best fit between the NFM simulated and experimental backscattered power characteristics, the peak and linewidth of the theoretical NFM Brillouin gain coefficient spectrum are $1.10.10^{-11}$ $m.W^{-1}$ and 88.7 MHz, respectively, compared to $1.16.10^{-11}$ $m.W^{-1}$ and 60 MHz for the UFM. The procedure for predicting excess and hence overall SBS CNRs at the real fibre length from simulations at NFM lengths of 120 to 482 m is in principle the same as for the UFM.

As in the case of the UFM, agreement between the total predicted CNR, based on NFM simulation of SBS, and the experimental CNR in the presence of the fibre is good. The predicted CNR corresponds even better with modified experimental CNR points, for which the input power has been adjusted such that similarly translated experimental backscattered power points would line up with the NFM simulated backscattered power curve.

A comparison of the UFM and NFM characteristics of SBS excess CNR predicted at the real fibre length, shown in figs. 5.5 and 5.13, reveals that these are broadly in agreement within the estimated limits of uncertainty. However, the UFM characteristic of SBS CNR inferred at high model fibre lengths, CNR_{hlm}, is 2 to 3 dB higher than the equivalent NFM characteristic. This is consistent with the fact that the UFM theoretical Brillouin gain coefficient spectrum at 67.25 MHz is lower than that for the NFM. The difference in CNR_{hlm} between UFM and NFM is not readily apparent in the two comparisons of total predicted CNR with experimental CNR. At input powers of 8.5 to 9 dBm, the SBS excess CNR dominates over CNR_{hlm}, at least for the lower estimated limit of CNR, for each model. At lower input powers, the CNRs from multipath interference and the linear attenuator link dominate over CNR_{hlm} for each model. However, if the real fibre length had been higher, or the subcarrier frequency lower, the difference in the total predicted CNRs for the two models would have been more noticeable.

6. CONCLUSIONS

The principal conclusions for the work presented in this thesis are described in section 6.1. Ideas for extending the computer model to allow estimation of Bit Error Rates for digital transmission systems influenced by SBS are discussed in section 6.2. Comments are also made with regard to the inclusion of Group Velocity Dispersion and other optical nonlinear effects in the model.

6.1 PRESENTED WORK

The primary objective of this project has been to provide a simulation tool for systems influenced by SBS which represents a substantial improvement on previous models, with particular emphasis on externally modulated AM-VSB CATV transmission links. This objective has been achieved in various respects. Although Höök and Bolle have simulated signal intensity waveform distortion from SBS for PSK modulated transmission, their model has relied on an injected Stokes seed and has consequently been found unsuitable for modelling a very significant class of transmitted SBS noise. An analysis of the three SBS PDEs including a description of distributed thermal acoustic noise (DTAN), presented in this work, to my knowledge, for the first time, has shown that a component of transmitted SBS noise arises from the product of the Stokes field and the spontaneous density variation. This Stokes-spontaneous density depletion noise (SSDDN) would not be generated by means of an SBS model with a Stokes seed, but only by the inclusion of simulated DTAN. Although simulations using the three SBS PDEs with DTAN have been carried out by Boyd et al. to investigate the statistical and spectral properties of the Stokes field, they have not studied the transmitted field in this way.

Boyd's model has been enhanced, probably for the first time, by the addition of two PDEs which describe the evolution of the SSDDN component of the transmitted field. Simulations using this enhanced model for the case of a CW pump input have

shown that the optical power spectrum of the transmitted field tends towards that of the depleted signal at the pump frequency and that of the separately simulated SSDDN at other frequencies as the model fibre length (MFL) is increased or as the input power is decreased. Since the simulated SSDDN spectrum is found to remain essentially independent of MFL, it represents the complete transmitted SBS noise spectrum at very high MFLs. By generating a set of optical power spectra for the entire transmitted field for increasing MFLs, together with a simulated SSDDN spectrum, the transmitted field spectrum may be predicted, at least approximately, for MFLs which are too long to simulate in a feasible processing time but which are representative of typical communication link lengths. Alternatively, additional software may be used to model a system performance parameter, such as Carrier-to-Noise Ratio for a subcarrier multiplexed system, for each simulated transmitted field or SSDDN time domain sequence or spectrum. The performance parameter may then be predicted for the required MFL from those obtained for other MFLs and that inferred at very long MFLs from the SSDDN case.

The Brillouin shift frequency (BSF) of a single mode optical fibre is known to vary with doping concentrations, residual stresses and temperature. Differences in BSF for light travelling in different parts of the core-cladding cross-section and fluctuations in BSF along the fibre length therefore arise and lead to a broadening of the Brillouin gain spectrum relative to that expected for pure fused silica. In the case of a GeO_2-doped silica core fibre with pure silica cladding, guidance of acoustic longitudinal modes leads to the presence of subsidiary lobes as well as the principal lobe of the Brillouin gain spectrum and to a dependence of the BSF of the main lobe on core radius and the difference in acoustic velocity between core and cladding. As a consequence of the dependence of the BSF on these factors, the Brillouin gain spectrum can vary substantially both in shape and bandwidth from fibre to fibre.

Previous dynamic SBS models have assumed the Brillouin shift frequency to be constant over the fibre length and hence the Brillouin gain spectrum to be Lorentzian. For SMFs with Brillouin gain spectra which are approximately

Lorentzian from half to full maximum gain, this assumption is justifiable for the simulation of total backscattered and transmitted powers and for modelling the distortion of periodic transmitted signal waveforms, but can lead to inaccuracy when simulating transmitted SBS noise spectra. This has been shown to be important for the modelling of the carrier-to-noise ratio contribution from SBS noise for an optical intensity modulated subcarrier representative of that in an AM-VSB CATV link, as discussed below. The development of Boyd's SBS model to include variations in BSF over the model fibre length therefore appears to both novel and useful.

For the predictive computer model, the simplifying assumption has been made that the variation of BSF with distance is a random variable with a Gaussian pdf and a uniform (or white) power spectral distribution. The validity of this assumption has been confirmed for the simple case of a nominally step-index single-mode fibre with a pure silica core and F-doped cladding, for which Brillouin amplified power spectral measurements at a wavelength of 1.55 μm are reported in [4.1.6]. The Brillouin gain spectrum derived from these measurements has been found to fit a theoretical spectrum consisting of the convolution of an 11 MHz FWHM bandwidth Lorentzian spectrum with a Gaussian probability density function (pdf) of standard deviation equal to 9.5 MHz.

Two computer models of SBS in optical fibres have been developed and compared. For the uniform fibre model (UFM), each section for the numerical solution of the three partial differential equations is assumed to have the same BSF. The phonon intensity decay rate for each section is determined directly by the measured or specified linewidth of the Brillouin gain coefficient spectrum (bgcs) for the fibre to be modelled. The Brillouin gain coefficient for each section is equal to the peak of the bgcs for the whole model fibre.

For the nonuniform fibre model (NFM), each section for the numerical solution of the three partial differential equations is assumed to have a different BSF with a random value for which the pdf is Gaussian. The phonon intensity decay rate and

Brillouin gain coefficient for each section are determined by the linewidth and peak of the bgcs assumed for the idealised homogeneous core material of the fibre to be modelled.

For both models, a normalised version of the thermal acoustic noise term described by Boyd et al. [2.1.8] has been included in the normalised partial differential equations of Höök and Bolle [2.2.3]. In accordance with the theory of Deventer and Boot [3.2.2], two orthogonal polarisation modes of the SBS backscattered (Stokes) wave are simulated. For a low-birefringence fibre, this theory indicates that the mixing efficiencies of the pump with the dominant and subsidiary polarisation modes of the Stokes wave are 2/3 and 1/3, respectively.

The UFM has been tested by reproducing representative simulation results reported by Boyd et al. for the example of SBS in CS_2 for a single polarisation mode [2.1.8]. The simulated mean and standard deviation of the Stokes intensity are in excellent agreement with the characteristics simulated in [2.1.8]. It is found that the simulation of optical fibre lengths greater than about 1 km requires excessive processing time, so the distance scaling strategy of Höök and Bolle [2.2.3] has been adopted for both models, whereby a model fibre, which is shorter than the real fibre but has the same end-to-end loss and Brillouin gain, is simulated.

Characteristics of mean optical output and backscattered powers as functions of input power for a CW input signal have been simulated using both models (UFM and NFM) and compared with those from an experiment by Deventer and Boot [3.2.2], in which light at 1.537 μm is coupled into a 12.7 km single-mode fibre. With the UFM Brillouin gain linewidth made equal to 42 MHz, the sum of the measured Brillouin gain and laser linewidths, the simulated and experimental characteristics agree very well if the UFM Brillouin gain coefficient, g_B, is set to $1.943.10^{-11}$ $m.W^{-1}$. The equivalent value predicted from theory for a Brillouin gain linewidth of 42 MHz, a fibre core refractive index of 1.44, an acoustic velocity of $5.81.10^3$ $m.s^{-1}$, corresponding to the measured BSF of 10.88 GHz, and other

parameters as for fused silica is $g_B = 1.73 \cdot 10^{-11}$ m.W^{-1}. The difference between this and the fitting factor is 0.5 dB.

With the NFM end-to-end Brillouin gain linewidth also made equal to 42 MHz, the sum of the measured Brillouin gain and laser linewidths, the simulated and experimental characteristics agree very well if the Brillouin gain coefficient, g_B, assumed in each model fibre section of constant BSF is set to $4.72.10^{-11}$ m.W^{-1}. The Brillouin gain linewidth in each constant BSF section is assumed to be 13 MHz, corresponding to the sum of the Brillouin gain linewidth assumed for the idealised core material of 11 MHz and the laser linewidth of 2 MHz. The equivalent value predicted from theory for a Brillouin gain linewidth of 13 MHz, a fibre core refractive index of 1.44, an acoustic velocity of $5.81.10^3$ m.s^{-1}, corresponding to the measured BSF of 10.88 GHz, and other parameters as for fused silica is $g_B = 5.59.10^{-11}$ m.W^{-1}. The discrepancy of 0.7 dB can be explained in terms of errors in the measured loss and Brillouin gain linewidth and differences in the density and photoelastic constant for the GeO_2 doped core compared to those for pure silica.

The theoretical NFM and UFM Brillouin gain coefficient spectra (bgcs), for which the simulated output and backscattered powers fit the same experimental characteristics, are very similar to each other from half to full maximum height, but diverge at lower heights. The peak value of the NFM bgcs is $1.922.10^{-11}$ m.W^{-1}, while that for the UFM is $1.943.10^{-11}$ m.W^{-1}. For both models, the simulated output and backscattered powers are independent of model fibre length in the ranges investigated (31 to 496 m for the UFM and 25 to 400 m for the NFM). Agreement of the simulated backscattered power characteristics with undepleted pump theory is excellent for input powers up to 9 dBm in both cases. The difference between the UFM and NFM curves is only noticeable at the lowest input power of 0 dBm at which the dominant polarisation mode backscattered power differs by up to about 1 dB. This divergence at low powers is attributable to the emerging difference in the two Brillouin gain coefficient spectra below half height.

For both models, the simulated transmitted power spectrum appears to consist of three elements:

(i) a line spectrum, corresponding to the attenuated and SBS depleted optical carrier, which is independent of L_m,

(ii) an underlying SBS noise spectrum which is also independent of L_m,

(iii) an approximately triangular spectrum which depends on L_m as well as input power.

The third of these elements decreases with increasing relative frequency and increasing L_m and increases with increasing input power. This arises from the depletion term corresponding to the product of the Stokes field and the Brillouin amplified, or stimulated, component of the density variation. It has been shown that the second of the spectral elements, the "inferred" transmitted SBS noise, may be simulated by solving two more partial differential equations in addition to the three principal ones for each of the two polarisation modes. The inferred transmitted SBS noise arises from the depletion term corresponding to the product of the Stokes field and the thermal, or spontaneous, component of the density variation.

For both models, the simulated inferred transmitted SBS noise power is found to be independent of model fibre length in the ranges stated above. As a consequence of the divergence in the two Brillouin gain coefficient spectra below half height, the NFM inferred noise power is about 2 dB lower than that for the UFM at an input power of 0 dBm and about 1 dB lower at input powers between 6 and 15 dBm.

The computer model has been extended to include simulation of the detected photocurrent from a PIN photodiode placed at the output end of the model fibre. The input field envelope is modified to represent amplitude modulation of the input power by a single subcarrier at a modulation index of m_{sc} and a frequency of f_{sc}. The carrier-to-noise ratio (CNR) of the detected subcarrier channel is evaluated from the simulated electrical power spectrum of the detected photocurrent. The optical output field spectrum inferred for high model fibre lengths, L_m, is constructed from

the full optical output field spectral lines at frequencies of 0 and $\pm f_{sc}$ relative to that of the optical carrier and from the transmitted SBS optical noise field spectrum inferred for high L_m. The carrier-to-noise ratio inferred for high L_m (CNR_{hlm}) of the detected subcarrier channel is evaluated from the simulated electrical power spectrum of the detected photocurrent derived from the constructed "inferred" optical output field spectrum.

Characteristics of detected CNR for a single AM subcarrier as a function of input power have been simulated using both the UFM and NFM and compared with that from an experiment by Mao et al. in which the modulation index of the subcarrier at 67.25 MHz is 4% and the CNR is measured in a 4 MHz bandwidth [1.3.14]. For the UFM, the Brillouin gain coefficient, g_B, is chosen to give the best fit between the simulated and experimental characteristics of backscattered power as a function of input power and is equal to $1.16.10^{-11}$ $m.W^{-1}$. The Brillouin gain linewidth is evaluated as 60 MHz from theory for the parameters of bulk fused silica at a wavelength of 1.55 μm and the fitting value of g_B.

For the NFM simulations of detected CNR, the Brillouin gain linewidth for each section of constant BSF has been assumed to be 11 MHz. For this linewidth, the Brillouin gain coefficient, g_B, for each section is evaluated as $6.32.10^{-11}$ $m.W^{-1}$ from theory for the parameters of bulk fused silica at a wavelength of 1.55 μm. With the standard deviation of the BSF chosen to give the best fit between the NFM simulated and experimental backscattered power characteristics, the peak and linewidth of the theoretical NFM Brillouin gain coefficient spectrum are $1.10.10^{-11}$ $m.W^{-1}$ and 88.7 MHz, respectively, compared to $1.16.10^{-11}$ $m.W^{-1}$ and 60 MHz for the UFM.

For input powers of 8 and 9 dBm, and model fibre lengths between 87 and 695 m for the UFM and between 120 and 482 m for the NFM, the CNR arising only from the L_m-dependent detected noise components has been determined as the excess CNR, CNR_{exc}, from the overall simulated detected CNR, CNR_{ov}, and the CNR

inferred at high L_m, CNR_{hlm}. The graphs of excess CNR as a function of model fibre length have been used to predict values of CNR_{exc} and hence CNR_{ov} at the real fibre length of 13 km for these and other input powers.

As well as including the CNR from SBS, the total predicted CNR, CNR_{tp}, takes into account the experimental CNR, CNR_{lin}, with the fibre replaced by a linear optical attenuator of the same loss and also the CNR from multipath interference induced by signal double Rayleigh scattering, CNR_{mpi}. CNR_{mpi} is chosen as 58.5 dB to give the best fit of the total predicted CNR to the experimental CNR in the presence of the fibre, particularly for input powers between 6 and 7.5 dBm, at which the contribution from SBS is relatively small. The laser linewidth calculated from theory to give this value of CNR_{mpi} is 2.8 MHz.

Agreement between the total predicted CNR and the experimental CNR in the presence of the fibre is good when SBS is simulated using either the UFM or the NFM. In each case, the predicted CNR corresponds even better with modified experimental CNR points, for which the input power has been adjusted such that similarly translated experimental backscattered power points would line up with the simulated backscattered power curve.

The UFM and NFM characteristics of SBS excess CNR predicted at the real fibre length are broadly in agreement within the estimated limits of uncertainty. However, the UFM characteristic of SBS CNR inferred at high model fibre lengths, CNR_{hlm}, is 2 to 3 dB higher than the equivalent NFM characteristic. This is consistent with the fact that the UFM theoretical Brillouin gain coefficient spectrum at 67.25 MHz is lower than that for the NFM. The difference in CNR_{hlm} between UFM and NFM is not readily apparent in the two comparisons of total predicted CNR with experimental CNR. At input powers of 8.5 to 9 dBm, the SBS excess CNR dominates over CNR_{hlm}, at least for the lower estimated limit of CNR, for each model. At lower input powers, the CNRs from multipath interference and the linear attenuator link dominate over CNR_{hlm}. However, if the real fibre length had been

higher, or the subcarrier frequency lower, the difference in the total predicted CNRs for the two models would have been more noticeable.

6.2 FUTURE WORK

The computer model could be enhanced to enable the effects of SBS on optical signals with more general modulation formats to be simulated. One of the most difficult aspects of SBS simulation is the prediction of SBS noise related performance measures such as CNR or Bit Error Rate (BER) for fibre lengths which are too long to simulate directly for the required sampling frequency. This has been achieved for the case of the subcarrier channel by using CNRs at increasing model fibre lengths (MFLs), in conjunction with the simulated CNR inferred for high MFLs, to extrapolate the "excess" CNR at the real fibre length and, from this and the inferred CNR, to predict the overall CNR from SBS. Although the transmitted SBS noise field spectrum inferred for high MFLs can be directly simulated to a good approximation at practicable MFLs, as described above, it is more difficult in general to simulate the SBS depleted signal field spectrum inferred for high MFLs for input signals with complicated power spectra.

For the simple example of a carrier amplitude modulated by a single subcarrier, this depleted signal spectrum has been obtained by selecting the full simulated optical output field spectral lines at frequencies of 0 and $\pm f_{sc}$ relative to that of the optical carrier. In this way, the sidebands associated with SBS depletion at low MFLs and the SBS noise present at all MFLs are eliminated. For input signals with power distributed over a wide optical spectral range, a possible technique might be to simulate the full optical output field as a time domain sequence for a number of different thermal noise pattern seeds and take the average of the field sequences. Further work would be needed to validate this technique.

An alternative technique for simulating the SBS depleted signal field spectrum inferred for high MFLs might be based on the simultaneous solution of steady state ordinary differential equations for the pump field and Stokes power spectral densities. These differential equations could be derived for a generalised input signal field spectrum using similar methods to those followed in Appendices 3.1 and 3.2 for the simple case of a CW carrier input.

In order to simulate the BER performance of digital transmission links for which SBS is expected to be important, a modelling package such as SPOCS (Simulation Program for Optical Communications Systems) [3.3.2], [6.2.1] could be used in conjunction with the SBS model. SPOCS allows for ASK, FSK and PSK modulated signals to be generated in the time domain and received by means of direct or coherent detection followed by digital filtering, receiver noise addition, demodulation and eye diagram sampling. For very high BERs, the provided option of comparison of the eye diagram samples with a decision threshold followed by direct error counting is appropriate. For BERs of 10^{-3} and below, it is usually better to use the option of estimating the BER from the first six moments of each of the probability distributions computed from the amplitudes of those eye diagram samples known from the transmitted data pattern to correspond to 'ones', and from the amplitudes of those known to correspond to 'zeroes'[3.3.2], [6.2.1], [6.2.2].

It seems likely that the prediction of the first six moments of the probability distributions of the ones and zeroes at the real fibre length from simulations at various practicable MFLs may best be achieved by generating separate simulated photocurrent sequences in the time domain for

(i) the SBS depleted signal inferred for high MFLs,

(ii) the SBS depleted signal with MFL-dependent sidebands arising from the depletion term corresponding to the product of the Stokes field and the Brillouin amplified, or stimulated, component of the density variation,

(iii) the SBS depleted signal inferred for high MFLs combined with the SBS transmitted noise inferred for high MFLs arising from the depletion term corresponding to the product of the Stokes field and the thermal, or spontaneous, component of the density variation.

The second of these elements, the SBS Stokes-stimulated density depleted signal, may be simulated using two additional PDEs for each polarisation mode equivalent to those described for the SBS Stokes-spontaneous density depletion noise (SSDDN), previously called the inferred transmitted noise. Although the optical power spectrum of the SSDDN has been found to remain approximately constant over a wide range of MFL, the normalised standard deviation of the instantaneous power of the SSDDN shows a significant variation with MFL at high input powers and approaches unity for large MFL. It may therefore be important to characterise the variations of the eye diagram statistics with MFL for the third element of photocurrent as well as for the second. It might then be possible to predict the eye diagram statistics for all three elements at the real fibre length and construct the equivalent statistics for the full photocurrent, including depletion sidebands and SBS noise. From these and from the required decision threshold, the BERs for the ones and zeroes may be estimated and hence also the average BER.

The incorporation of Group Velocity Dispersion (GVD) into the present SBS model in the form of distributing the GVD over the length of the model fibre does not at first sight appear to be easy. The usual method of simulating GVD consists of converting the optical signal field from the time domain to the frequency domain, introducing a frequency dependent phase change and converting the signal back to the time domain. For the simulation of optical nonlinear effects which only require the modelling of a forward propagating optical signal, the complete time domain signal after a section of nonlinearity can be derived without reference to the evolution of the signal through the rest of the model fibre, so there is no difficulty in converting this signal to the frequency domain. For a time-distance plane SBS model, the complete time domain transmitted signal at an intermediate point along

the model fibre can only be obtained after forward propagation and backscattering have been simulated.

Self phase modulation and cross phase modulation of the pump and Stokes waves, together with at least some reflected waves, can be included in this type of SBS model, as done by Lu et al. [6.2.3]. However, the usefulness of simulating SPM in conjunction with SBS, but without GVD, is likely to be of limited value in modelling communication systems. Nevertheless, the SBS model presented here can be used to establish through performance predictions whether SBS suppression is likely to be required for a system and to evaluate the effectiveness of SBS suppression techniques, even if other models are independently needed for the characterisation of transmission in the presence of GVD and other nonlinear effects.

REFERENCES

1.1.1 D.D. Hall, M.J. Wale, C. Edge, and N.J. Parsons, "Advances in Microwave Optoelectronics", GEC Journal of Research, 1993, vol. 10, no. 2, pp. 80-84

1.1.2 A. Seeds, "Optical Beamforming Techniques for Phased-Array Antennas", Microwave Journal, 1992, vol. 35, no. 7, pp. 74-83

1.1.3 W.S. Birkmayer and M.J. Wale, "Proof-of-concept model of a coherent optical beam-forming network", IEE Proc., 1992, vol. 139, pt. J, no. 4, pp. 301-304

1.1.4 O.K. Tonguz and H. Jung, "Personal Communications Access networks using subcarrier multiplexed optical links", J. Lightwave Technol., 1996, vol.14, no.6, pp. 1400-1409

1.1.5 H. Ogawa, D. Polifko, and S. Banba, "Millimeter-Wave Fiber Optics Systems for Personal Radio Communication", IEEE Trans. Microwave Theory Tech., 1992, vol. 40, no.12, pp. 2285-2293

1.1.6 T.-S. Chu and M.J. Gans, "Fiber Optic Microcellular Radio", IEEE Trans. Veh. Technol., 1991, vol. 40, no.3, pp. 599-606

1.1.7 P.E. Green, "Optical networking update", IEEE J. Selected Areas Commun., 1996, vol. 14, no.5, pp. 764-779

1.1.8 P. Cochrane, "A three click, one second world", Electronics & Communication Engineering Journal, August 1995, pp. 138-139

1.1.9 R.W. Slim, "Video transmission over fibre", FOCUS magazine (Fibre Optic Communication & User Systems), 1996, no 26, pp. 8-15

1.1.10 P.S. Henry, "Lightwave Primer", IEEE J. Quantum Electron., 1985, vol. QE-21, no.12, pp. 1862-1879

1.1.11 A.R. Rutkowski, "Collected Internet growth history of number of hosts and packets per month", Private communication, Internet Society, Mar. 26, 1995

1.1.12 J. Crowcroft, "The Internet: a Tutorial", Electronics & Communication Engineering Journal, June 1996, pp. 113-122

1.1.13 J. Kraushaar, "Fiber deployment update - End of year 1993", FCC Common Carrier Bureau, May 13, 1994

1.1.14 R. Woollem, "Britain plugged into the superhighway", FOCUS magazine (Fibre Optic Communication & User Systems), 1995, no 23, p. i.

1.1.15 J.R. Jones, "The pros and cons of switched versus broadcast local access systems", FOCUS magazine (Fibre Optic Communication & User Systems), 1995, no 23, pp. 2-25

1.1.16 C.A. Brackett, "Foreword to special issue: Is there an emerging concensus on WDM networking", J. Lightwave Technol., 1996, vol.14, no.6, pp. 936-941

1.1.17 I.P. Kaminow, C.R. Doerr, C. Dragone, T. Koch, U. Koren, A.A.M. Saleh, A.J. Kirby, C.M. Özveren, B. Schofield, R.E. Thomas, R.A. Barry, D.M. Castagnozzi, V.W.S. Chan, B.R. Hemenway, Jr., D. Marquis, S.A. Parikh, M.L. Stevens, E.A. Swanson, S.G. Finn, and R.G. Gallager, "A wideband all-optical WDM network", IEEE J. Selected Areas Commun., 1996, vol. 14, no.5, pp. 780-799

1.1.18 E. Hall, J. Kravitz, R. Ramaswami, M. Halvorson, S. Tenbrink, and R. Thomsen, "The Rainbow-II Gigabit optical network", IEEE J. Selected Areas Commun., 1996, vol. 14, no.5, pp. 814-823

1.1.19 G.-K. Chang, G. Ellinas, J. K. Gamelin, M. Z. Iqbal, and C.A. Brackett, "Multiwavelength reconfigurable WDM/ATM/SONET network testbed", J. Lightwave Technol., 1996, vol.14, no.6, pp. 1320-1340

1.1.20 S. Johansson, "Transport network involving a reconfigurable WDM network layer", J. Lightwave Technol., 1996, vol.14, no.6, pp. 1341-1348

1.1.21 E.-J. Bachus, T. Almeida, P. Demeester, G. Depovere, A. Ebberg, M.R. Ferreira, G.-D. Khoe, O. Koning, R. Marsden, J. Rawsthorne, and N. Wauters, "Coherent Optical Systems implemented for Business Traffic Routing and Access: The RACE COBRA Project", J. Lightwave Technol., 1996, vol.14, no.6, pp. 1309-1319

1.1.22 R.E. Wagner, R.C. Alferness, A.A.M. Saleh, and M.S. Goodman, "MONET: Multiwavelength optical networking", J. Lightwave Technol., 1996, vol.14, no.6, pp. 1349-1355

1.1.23 T.-K. Chiang, S.K. Agrawal, D.T. Mayweather, D. Sadot, C.F. Barry, M. Hickey, and L.G. Kazovsky, "Implementation of STARNET: A WDM computer communications network", IEEE J. Selected Areas Commun., 1996, vol. 14, no.5, pp. 824-839

1.1.24 H. Toba, K. Oda, K. Inoue, K. Nosu, and T. Kitoh, "An optical FDM-based self-healing ring network employing arrayed waveguide grating filters and EDFAs with level equalisers", IEEE J. Selected Areas Commun., 1996, vol. 14, no.5, pp. 800-813

1.1.25 R.A. Barry, V.W.S. Chan, K.L. Hall, E.S. Kintzer, J.D. Moores, K.A. Rauschenbach, E.A. Swanson, L.E. Adams, C.R. Doerr, S.G. Finn, H.A. Haus, E.P. Ippen, W.S. Wong, and M. Haner, "All-Optical Network Consortium - Ultrafast TDM Networks", IEEE J. Selected Areas Commun., 1996, vol. 14, no.5, pp. 999-1013

1.1.26 H. Taga, "Long distance transmission experiments using the WDM technology", J. Lightwave Technol., 1996, vol.14, no.6, pp. 1287-1298

1.1.27 N.S. Bergano and C.R. Davidson, "Wavelength Division Multiplexing in long-haul transmission systems", J. Lightwave Technol., 1996, vol.14, no.6, pp. 1299-1308

1.1.28 S.G. Grubb, "Diode-pumped solid-state laser pumping of co-doped erbium optical amplifiers", in Conference on Optical Fiber Communication (OFC'92), Jan./Feb. 1992, San Jose, CA, vol. 5, 1992 OSA Technical Digest Series (Optical Society of America, Washington DC, 1992), paper TuG1, p 31

1.1.29 H. Takenaka, H. Okuno, M. Fujita, Y. Odagiri, Y. Sunohara, and I. Mito, "Compact Size and High Output Power Er-doped Fiber Amplifier Modules Pumped With 1.48 μm MQW LDs", Topical OSA/IEEE meeting on "Optical Amplifiers and their Applications", July 24-26, 1991, Snowmass Village, Colorado, paper FD2, pp 254-257

1.1.30 Y. Aoki, T. Saito, K. Fukagai, Y. Sunohara, S. Ishikawa and S. Fujita, "Low Noise and High Saturation Output Power Erbium-Doped Fiber Amplifiers pumped with 0.98 μm and 1.48 μm LDs for Long-Distance Optical Communication", Proc. 17th Eur. Conf. on Opt. Comm./8th Int. Conf. on Integrated Optics and Opt. Fibre Comm. (IOOC-ECOC'91), 9-12 Sept. 1991, Paris, France, publ. by SEER, 1991, spons. by IEICE, LEOS and OSA, Vol. 1, paper WeC9-2, pp 585-588

1.1.31 P. Trischitta, M. Colas, M. Green, G. Wuzniak, J. Arena, "The TAT-12/13 cable network", IEEE Commun. Mag., Feb. 1996, vol. 34, no. 2, pp. 24-28

1.1.32 N.S. Bergano, C.R. Davison, D.L. Wilson, F.W. Kerfoot, M.D. Tremblay, M.D. Levonas, J.P. Morreale, J.D. Evankow, P.C. Corbett, M.A. Mills, G.A. Ferguson, A.M. Vengsarkar, J.R. Pedrazzani, J.A. Nagel, J.L. Zyskind, and J.W. Sulhoff, "100 Gb/s error free transmission over 9100 km using twenty 5 Gb/s WDM data channels", in Conf. Optic. Fiber Commun. (OFC '96), Feb. 1996, San Jose, CA, 1996 OSA Technical Digest Series (Optical Society of America, Washington DC, 1996), Postdeadline paper PD23

1.2.1 G.P. Agrawal, "Nonlinear Fiber Optics", Academic Press, 1989

1.2.2 R.N. Thurston, "Elastic Waves in Rods and Optical Fibers", Journal of Sound and Vibration, 1992, vol.159, no.3, pp. 441-467

1.2.3 D. Cotter, "Stimulated Brillouin Scattering in Monomode Optical Fiber", J. Opt. Commun., 1983, vol. 4, no.1, pp. 10-19

1.2.4 A.R. Chraplyvy, "Limitations on Communications Imposed by Optical-Fiber Nonlinearities", J. Lightwave Technol., 1990, vol. 8, no.10, pp. 1548-1557

1.2.5 R.G. Smith, "Optical Power Handling Capacity of Low Loss Optical Fibers as Determined by Stimulated Raman and Brillouin Scattering", Appl. Opt., 1972, vol. 11, no.11, pp. 2489-2494

1.2.6 N. Shibata, K. Nosu, K. Iwashita, and Y. Azuma, "Transmission Limitations Due to Fiber Nonlinearities in Optical FDM Systems", IEEE J. Selected Areas Commun., 1990, vol. 8, no.6, pp. 1068-1077

1.2.7 R.G. Waarts, A.A. Friesem, E. Lichtman, H.H. Yaffe, and R.-P. Braun, "Nonlinear Effects in Coherent Multichannel Transmission Through Optical Fibers", Proc. IEEE, 1990, vol. 78, no.8, pp. 1344-1368

1.2.8 E. Lichtman, "Bit Rate-Distance Product Limitations due to Fiber Nonlinearities in Multichannel Coherent Optical Communication Systems", Electron. Lett., 1991, vol. 27, no.9, pp. 757-759

1.2.9 J.C. Palais, T.-Y. Lin, and S. Tariq, "Power Limitations in Fiber-Optic Frequency-Division Multiplexed Systems", Fiber and Integrated Optics, 1991, vol. 10, no.1, pp. 75-94

1.2.10 T. Koyama, N. Henmi, and Y. Aoki, "Compensation for Nonlinear Pulse Distortion in Optical Fiber by Employing Prechirp Technique", Proc. 17th Eur. Conf. on Opt. Comm./8th Int. Conf. on Integrated Optics and Opt. Fibre Comm. (IOOC-ECOC'91), 9-12 Sept. 1991, Paris, France, publ. by SEER, 1991, spons. by IEICE, LEOS and OSA, Vol. 1, pp 469-472

1.2.11 O. Audouin, L. Prigent, J.P. Blondel, J.P. Hamaide, and J.M. Gabriagues, "Evaluation of Theoretical Limits of Cascaded EDFA Transmission Systems", Topical OSA/IEEE meeting on "Optical Amplifiers and their Applications", July 24-26, 1991, Snowmass Village, Colorado, paper ThA3, pp 86-89

1.2.12 S. Yamamoto, H. Taga, Y. Yoshida, and H. Wakabayashi, "Characteristics of Single-Carrier Fiber-Optic Transmission Systems using Optical Amplifiers", Topical OSA/IEEE meeting on "Optical Amplifiers and their Applications", July 24-26, 1991, Snowmass Village, Colorado, paper ThA4, pp 90-93

1.2.13 X.Y. Zou, M.I. Hayee, S.-M. Hwang, and A.E. Willner, "Limitations in 10 Gb/s WDM optical-fiber transmission when using a variety of fiber types to manage dispersion and nonlinearities", J. Lightwave Technol., 1996, vol.14, no.6, pp. 1144-1152

1.3.1 N. Ohkawa and Y. Hayashi, "Demodulated waveform distortion by SBS in CPFSK coherent systems", in Conference on Optical Fiber Communications, Feb. 1995, San Diego, CA, 1995 OSA Technical Digest Series (Optical Society of America, Washington DC, 1995), pp. 96-97

1.3.2 N. Ohkawa and Y. Hayashi, "Reduction of bit error rate performance deterioration caused by stimulated Brillouin scattering in high-power CPFSK coherent optical transmission systems", Electron. Lett., 1994, vol. 30, no. 6, pp. 515-516

1.3.3 Y. Hayashi, N. Ohkawa and D. Yanai, "Estimated performance of 2.488 Gb/s CPFSK optical non-repeatered transmission system employing high-output power EDFA boosters", J. Lightwave Technol., 1993, vol. 11, no. 8, pp. 1369-1376

1.3.4 E.M. Kimber, X. Gu, S.J. Pycock, E. Pittuck, B.L. Patel, D.M. Spirit, J. Wakefield, A.D. Ellis and C.J. Anderson, "Unrepeatered 2 x 10-Gbit/s narrow-band WDM field technology demonstration over 120 km of installed step-index fiber", in Conference on Optical Fiber Communications, Feb. 1995, San Diego, CA, 1995 OSA Technical Digest Series (Optical Society of America, Washington DC, 1995), paper TuC4, pp. 5-6

1.3.5 D.A. Fishman and J.A. Nagel, "Degradations due to stimulated Brillouin scattering in multigigabit intensity-modulated fiber-optic systems", J. Lightwave Technol., 1993, vol. 11, no. 11, pp. 1721-1728

1.3.6 P.B. Hansen, L. Eskildsen, S.G. Grubb, A.M. Vengsarkar, S.K. Korotky, T.A. Strasser, J.E.J. Alphonsus, J.J. Veselka, D.J. DiGiovanni, D.W. Peckham, D. Truxal, W.Y. Cheung, S.G. Kosinski, and P.F. Wysocki, "10 Gb/s, 411 km repeaterless transmission experiment employing dispersion compensation and remote post- and pre-amplifiers", Proc. 21st Eur. Conf. on Opt. Comm. (ECOC'95), 17-21 Sept. 1995, Brussels, Belgium, publ. by IMEC, Gent, Belgium, 1995, distr. by IMEC and IEEE, vol. 2, paper We.B.1.2, pp. 565-568

1.3.7 J-M.P. Delavaux, O. Mizuhara, P.D. Yeates and T.V. Nguyen, "10 Gb/s - 150 km bi-directional repeaterless optical fiber transmission", Proc. 21st Eur. Conf. on Opt. Comm. (ECOC'95), 17-21 Sept. 1995, Brussels, Belgium, publ. by IMEC, Gent, Belgium, 1995, distr. by IMEC and IEEE, vol. 2, paper We.B.2.1, pp. 593-596

1.3.8 J. Nakagawa, K. Shimuzu, T. Mizuochi, K. Takano, K. Motoshima, and T. Kitayama, "10 Gbit/s - 270 km non-repeated optical transmission experiment with high receiver sensitivity", Proc. 21st Eur. Conf. on Opt. Comm. (ECOC'95), 17-21 Sept. 1995, Brussels, Belgium, publ. by IMEC, Gent, Belgium, 1995, distr. by IMEC and IEEE, vol. 2, paper We.B.2.3, pp. 601-604

1.3.9 A. Hirose, Y. Takushima and T. Okoshi, "Suppression of Stimulated Brillouin Scattering and Brillouin Crosstalk by Frequency-Sweeping Spread-Spectrum Scheme", J. Opt. Commun., 1991, vol. 12, no.3, pp. 82-85

1.3.10 T. Sugie, N. Ohkawa, T. Imai and T. Ito, "A novel repeaterless CPFSK coherent lightwave system employing an optical booster amplifier", J. Lightwave Technol., 1991, vol.9, no.9, pp. 1178-1186

1.3.11 K. Shiraki, M. Ohashi, and M. Tateda, "SBS suppression in dispersion-shifted fiber with a dual shape core", Proc. 21st Eur. Conf. on Opt. Comm. (ECOC'95), 17-21 Sept. 1995, Brussels, Belgium, publ. by IMEC, Gent, Belgium, 1995, distr. by IMEC and IEEE, vol. 1, paper Tu.L.2.2, pp. 325-328

1.3.12 M. Tateda, "New optical fibers for long-span transmission systems", in Conference on Optical Fiber Communications, Feb. 1995, San Diego, CA, 1995 OSA Technical Digest Series (Optical Society of America, Washington DC, 1995), paper ThH4, pp. 262-264

1.3.13 R. Yamauchi, "Optical-fiber nonlinearity: measurements and countermeasures", in Conference on Optical Fiber Communications, Feb. 1995, San Diego, CA, 1995 OSA Technical Digest Series (Optical Society of America, Washington DC, 1995), paper FD2, p. 313

1.3.14 X.P. Mao, G.E. Bodeep, R.W. Tkach, A.R. Chraplyvy, T.E. Darcie, and R.M. Derosier, "Brillouin scattering in externally modulated lightwave AM-VSB CATV transmission systems", IEEE Phot. Tech. Lett., 1992, vol.4, no.3, pp. 287-289

1.3.15 J.C. van der Plaats, W. Muys, F.W. Willems, A.M.J. Koonen and J.S. Leong, "A bi-directional 1.5 μm AM-VSB video-on-demand lightwave system using a two-window optical branching amplifier and an isolatorless last stage EDFA", Proc. 21st Eur. Conf. on Opt. Comm. (ECOC'95), 17-21 Sept. 1995, Brussels, Belgium, publ. by IMEC, Gent, Belgium, 1995, distr. by IMEC and IEEE, vol. 1, paper Tu.L.3.5, pp. 363-366

1.3.16 H. Yoshinaga, M. Kagami, K. Kishuma, and K. Suto, "Nonlinear distortion due to stimulated Brillouin scattering and its suppression in SCM video-transmission systems", in Conference on Optical Fiber Communication/International Conference on Integrated Optics and Optical Fiber Communication (OFC/IOOC'93), Jan./Feb. 1993, 1993 OSA Technical Digest Series, vol. 4 (Optical Society of America, Washington, D.C., 1993), paper FC8, pp. 257-258

1.3.17 F.W. Willems, W. Muys, and J.S. Leong, "Simultaneous suppression of stimulated Brillouin scattering and interferometric noise in externally modulated lightwave AM-SCM systems", IEEE Phot. Tech. Lett., 1994, vol.6, no.12, pp. 1476-1478

1.3.18 F.W. Willems, J.C. van der Plaats and W. Muys, "Harmonic distortion caused by stimulated Brillouin scattering suppression in externally modulated lightwave AM-CATV systems", Electron. Lett., 1994, vol. 30, no. 4, pp. 343-345

1.3.19 Mao, X.P., Bodeep, G.E., Tkach, R.W., Chraplyvy, A.R., Darcie, T.E., and Derosier, R.M.: "Suppression of Brillouin scattering in lightwave AM-VSB CATV transmission systems", in Conference on Optical Fiber Communication/International Conference on Integrated Optics and Optical Fiber Communication (OFC/IOOC'93), Jan./Feb. 1993, 1993 OSA Technical Digest Series, vol. 4 (Optical Society of America, Washington, D.C., 1993), paper WI8, pp. 141-143

1.3.20 C. Desem, "Composite second order distortion due to self-phase modulation in externally modulated optical AM-SCM systems operating at 1550 nm", Electron. Lett., 1994, vol. 30, no. 24, pp. 2055-2056

2.1.1 D. Heiman, D.S. Hamilton and R.W. Hellwarth, "Brillouin scattering measurements on optical glasses", Phys. Rev. B, 1979, vol. 19, no. 12, pp. 6583-6592

2.1.2 R.J. Pressley (ed.), "Handbook of Lasers", Chemical Rubber Co., Cleveland (1971)

2.1.3 J. Schroeder, R. Mohr, P.B. Macedo, and C.J. Montrose, "Rayleigh and Brillouin scattering in K_2O-SiO_2 glasses", J. Am. Ceram. Soc., 1973, vol. 56, no. 10, pp. 510-514

2.1.4 X.P. Mao, R.W. Tkach, A.R. Chraplyvy, R.M. Jopson and R.M. Derosier, "Stimulated Brillouin threshold dependence on fiber type and uniformity", IEEE Phot. Tech. Lett., 1992, vol. 4, no. 1, pp. 66-69

2.1.5 Y. Aoki, K. Tajima and I. Mito, "Input power limits of single-mode optical fibers due to stimulated Brillouin scattering in optical communication systems", J. Lightwave Technol., 1988, vol. 6, no.5, pp. 710-719

2.1.6 T. Sugie, "Transmission limitations of CPFSK coherent lightwave systems due to stimulated Brillouin scattering in optical fiber", J. Lightwave Technol., 1991, vol.9, no.9, pp. 1145-1155

2.1.7 E. Lichtman, R.G. Waarts, and A.A. Friesem, "Stimulated Brillouin scattering excited by a modulated pump wave in single-mode fibers", J. Lightwave Technol., 1989, vol.7, no.1, pp. 171-174

2.1.8 R.W. Boyd, K. Rzazewski and P. Narum, "Noise initiation of stimulated Brillouin scattering", Phys. Rev. A, 1990, vol.42, no.9, pp. 5514-5521

2.1.9 E. Lichtman, A.A. Friesem, R.G. Waarts, and H.H. Yaffe, "Stimulated Brillouin scattering excited by two pump waves in single-mode fibers", J. Opt. Soc. Amer. B, 1987, vol.4, no. 9, pp. 1397-1403

2.1.10 A. Bolle, G. Grosso and B. Daino, "Brillouin Gain Curve Dependence on Frequency Spectrum of PSK-Modulated Signals", Electron. Lett., 1989, vol. 25, no. 1, pp. 2-3

2.1.11 A.S. Pine, "Brillouin scattering study of acoustic attenuation in fused quartz", Phys. Rev., 1969, vol.185, no.3, pp. 1187-1193

2.1.12 C. K. Jen, J.E.B. Oliveira, N. Goto, and K. Abe, "Role of guided acoustic wave properties in single-mode optical fibre design", Electron. Lett., 1988, vol.24, no. 23, pp. 1419-1420

2.1.13 C. K. Jen, and N. Goto, "Backward collinear guided-wave-acousto-optic interactions in single-mode fibers", J. Lightwave Technol., 1989, vol.7, no.12, pp. 2018-2023

2.1.14 C. K. Jen, A. Safaai-Jazi, and G.W. Farnell, "Leaky modes in weakly guiding fiber acoustic waveguides", IEEE Trans. Ultrason. Ferroelectr. Freq. Contr., 1986, UFFC-33, no. 6, pp. 634-643

2.1.15 A. Safaai-Jazi, C. K. Jen, and G.W. Farnell, "Analysis of weakly guiding fiber acoustic waveguide", IEEE Trans. Ultrason. Ferroelectr. Freq. Contr., 1986, UFFC-33, no. 1, pp. 59-68

2.1.16 Y. Azuma, N. Shibata, T. Horiguchi, and M. Tateda, "Wavelength dependence of Brillouin-gain spectra for single-mode optical fibres", Electron. Lett., 1988, vol.24, no. 5, pp. 250-252

2.1.17 N. Shibata, Y. Azuma, T. Horiguchi, and M. Tateda, "Identification of longitudinal acoustic modes guided in the core region of a single-mode optical fiber by Brillouin gain spectra measurements", Opt. Lett., 1988, vol.13, no. 7, pp. 595-597

2.1.18 N. Shibata, K. Okamoto, and Y. Azuma, "Longitudinal acoustic modes and Brillouin-gain spectra for GeO_2-doped-core single-mode fibers", J. Opt. Soc. Amer. B, 1989, vol.6, no. 6, pp. 1167-1174

2.1.19 N. Shibata, R.G. Waarts, and R.P. Braun, "Brillouin-gain spectra for single-mode fibers having pure-silica, GeO_2-doped, and P_2O_5-doped cores", Opt. Lett., 1987, vol.12, no. 4, pp. 269-271

2.1.20 R.W. Tkach, A.R. Chraplyvy, and R.M. Derosier, "Spontaneous Brillouin scattering for single-mode optical-fibre characterisation", Electron. Lett., 1986, vol.22, no. 19, pp. 1011-1013

2.2.1 P. Bayvel and P.M. Radmore, "Solutions of the SBS equations in single mode optical fibres and implications for fibre transmission systems", Electron. Lett., 1990, vol. 26, no. 7, pp. 434-436

2.2.2 I.L. Fabelinskii, "Molecular scattering of light", transl. R.T. Beyer, Plenum Press, New York, 1968

2.2.3 A. Höök and A. Bolle, "Transient dynamics of stimulated Brillouin scattering in optical communication systems", J. Lightwave Technol., 1992, vol.10, no.4, pp. 493-502

2.2.4 A.L. Gaeta and R.W. Boyd, "Stochastic dynamics of stimulated Brillouin scattering in an optical fiber", Phys. Rev. A, 1991, vol.44, no.5, pp. 3205-3209

2.2.5 R. Chu, M. Kanefsky, and J. Falk, "Numerical study of transient stimulated Brillouin scattering", J. Appl. Phys., 1992, vol.71, no.10, pp. 4653-4658

2.2.6 M.J. Damzen and H. Hutchinson, "Laser pulse compression by stimulated Brillouin scattering in tapered waveguides", IEEE J. Quantum Electron., 1983, vol. QE-19, no.1, pp. 7-14

2.2.7 A. Höök, "Pulse formation in phase-modulated optical fiber signals due to stimulated Brillouin scattering", J. Opt. Soc. Amer. B, 1991, vol.8, no.6, pp. 1284-1289

2.2.8 C. Montes and A.M. Rubenchik, "Stimulated Brillouin scattering from trains of solitons in optical fibers: information degradation", J. Opt. Soc. Amer. B, 1992, vol.9, no.10, pp. 1857-1875

2.2.9 C.G. Parazzoli, W.W. Buchman, and R.D. Stultz, "Numerical and experimental investigation of a stimulated Raman half resonator", IEEE J. Quantum Electron., 1988, vol.24, no.6, pp. 872-880

2.2.10 A. Höök, A. Bolle, G. Grosso and M. Martinelli, "Influence of stimulated Brillouin scattering on phase modulated signals in optical fibres", Electron. Lett., 1990, vol.26, no.7, pp. 470-472

2.2.11 A. Bolle, G. Grosso and B. Daino, "Temporal Characteristics of Phase Modulated Signals in the Presence of Stimulated Brillouin Scattering(SBS)", Proc. 15th European Conf. on Optical Communication (ECOC '89), Göteborg, Sweden, Sept. 1989, vol.1, paper TuB8-3, pp. 146-149

3.1.1 A. Yariv, "Optical Electronics", 4th ed., 1991, Saunders HBJ, London

3.2.1 R.H. Stolen, "Polarization effects in fiber Raman and Brillouin lasers", IEEE J. Quantum Electron., 1979, vol. QE-15, pp. 1157-1161

3.2.2 M.O. van Deventer and A.J. Boot, "Polarization properties of stimulated Brillouin scattering in single-mode fibers", J. Lightwave Technol., 1994, vol.12, no.4, pp. 585-590

3.2.3 E. Brinkmeyer, "Forward-backward transmission in birefringent single-mode fibers: interpretation of polarization-sensitive measurements", Optics Lett., 1981, vol.6, no.11, pp. 575-577

3.2.4 M.O. van Deventer, "Polarization properties of Rayleigh backscattering in single-mode fibers", J. Lightwave Technol., 1993, vol.11, no.12, pp. 585-590

3.2.5 T. Horiguchi, M. Tateda, N. Shibata, and Y. Azuma, "Brillouin gain variation due to a polarization-state change of the pump or Stokes field in standard single-mode fibers", Optics Lett., 1989, vol.14, no.6, pp. 329-331

3.3.1 J.A. Fleck, "Ultrashort-pulse generation by Q-switched lasers", Phys. Rev. B, 1970, vol.1, no.1, pp. 84-100

3.3.2 F. Libbrecht, "Studie en systeemsimulatie van optische informatietransmissie", PhD Thesis, Rijksuniversiteit Gent, Dec. 1990

3.3.3 R.F.W. Coates, G.J. Janacek and K.V. Lever, "Monte Carlo Simulation and Random Number Generation", IEEE J. Selected Areas Commun., 1988, vol. 6, no. 1, pp. 58-66

3.3.4 G.E.P. Box and M.E. Muller, "A Note on the Generation of Random Normal Deviates", Ann. Math. Statist., 1958, vol. 29, pp. 610-611

3.3.5 W.H. Press, B.P. Flannery, S.A. Teukolsky and W.T. Vetterling, "Numerical recipes: the art of scientific computing", 1986, Cambridge University Press

3.4.1 R.H. Enns and I.P. Batra, "Saturation and depletion in stimulated light scattering", Physics Lett. A, 1969, vol.28A, no.8, pp. 591-592

4.1.1 T.-O.Tsun, A. Wada, and R. Yamauchi, "Wavelength dependences of Brillouin frequency shifts of optical fibres in 1.55 μm wavelength region", Electron. Lett., 1991, vol. 27, no. 19, pp. 1764-1765

4.1.2 Y. Hibino, T. Edahiro, T. Horiguchi, Y. Azuma, and N. Shibata, "Evaluation of residual stress and viscosity in SiO_2-core/F-SiO_2 clad single-mode optical fibers from Brillouin gain spectra", J. Appl. Phys., 1989, vol. 66, no. 9, pp. 4049-4052

4.1.3 T. Horiguchi, T. Kurashima, M. Tateda, K. Ishihara, and Y. Wakui, "Brillouin characterization of fiber strain in bent slot-type optical-fiber cables", J. Lightwave Technol., 1992, vol. 10, no. 9, pp. 1196-1201

4.1.4 T. Kurashima, T. Horiguchi, and M. Tateda, "Thermal effects of Brillouin gain spectra in single-mode fibers", IEEE Photon. Technol. Lett., 1990, vol. 2, no. 10, pp. 718-720

4.1.5 K. Shimizu, T. Horiguchi, Y. Koyamada, and T. Kurashima, "Coherent self-heterodyne detection of spontaneously Brillouin-scattered light waves in a single-mode fiber", Optics Lett., 1993, vol.18, no.3, pp. 185-187

4.1.6 T.-O. Tsun, A. Wada, T. Sakai, and R. Yamauchi, "Novel method using white spectral probe signals to measure Brillouin gain spectra of pure silica core fibres", Electron. Lett., 1992, vol. 28, no. 3, pp. 247-249

5.1.1 S.K. Korotky and R.M. de Ridder, "Dual parallel modulation schemes for low-distortion analog optical transmission", IEEE J. Selected Areas Commun., 1990, vol. 8, no. 7, pp. 1377-1381

5.1.2 M.R. Phillips, T.E. Darcie, D. Marcuse, G.E. Bodeep and N.J. Frigo, "Nonlinear distortion generated by dispersive transmission of chirped intensity-modulated signals", IEEE Photon. Technol. Lett., 1991, vol. 3, no. 5, pp. 481-483

6.2.1 F. Libbrecht and P. Lagasse, "SPOCS a Versatile Tool for the System Analysis and Design of Optical Communication Systems", Proc. 16th European Conf. on Optical Communication (ECOC '90), Amsterdam, Netherlands, 16-20 Sept. 1990, publ. by PTT Nederland, spons. by AT&T Network Syst. Int., Vol. 1, pp. 171-174

6.2.2 R.F. Pawula, "Approximating distributions from moments", Phys. Rev. A, 1987, vol.36, no.10, pp. 4996-5007

6.2.3 W. Lu, A. Johnstone, and R.G. Harrison, "Deterministic dynamics of stimulated scattering phenomena with external feedback", Phys. Rev. A, 1992, vol.46, no.7, pp. 4114-4122

A1.1 K. Kikushima, E. Yoneda, K. Suto, and H. Yoshinaga, "Simultaneous distribution of AM/FM FDM TV signals to 65,536 subscribers using 4 stage cascade EDFAs", Topical OSA/IEEE meeting on "Optical Amplifiers and their Applications", August 6-8, 1990, Monterey, paper WB1, pp. 232-235

A1.2 A.H. Gnauck, T.E. Darcie, and G.E. Bodeep, "Comparison of direct and external modulation for CATV lightwave transmission at 1.5 μm wavelength", Electron. Lett., 1992, vol. 28, no. 20, pp. 1875-1876

A1.3 T.E. Darcie, "Subcarrier multiplexing for lightwave networks and video distribution systems", IEEE Journal on Selected Areas in Communications, 1990, vol. 8, no. 7, pp. 1240-1248

A1.4 J. Lipson, L.C. Upadhyayula, S.Y. Huang, C.B. Roxlo, E.J. Flynn, P.M. Nitzsche, C.J. McGrath, G.L. Fenderson, and M.S. Schaefer, "High-fidelity lightwave transmission of multiple AM-VSB NTSC signals", IEEE Transactions on Microwave Theory and Techniques, 1990, vol. 38, no. 5, pp. 483-493

A1.5 W.Susaki, "Recent progress in superlinear InGaAsP laser diodes", in Conference on Optical Fiber Communication (OFC'91), Jan./Feb. 1991, San Diego, CA, 1991 OSA Technical Digest Series (Optical Society of America, Washington DC, 1991), paper WG5

A1.6 C.Y. Kuo and E.E. Bergman, "Erbium-doped fiber amplifier second order distortion in analog links and electronic compensation", IEEE Photon. Technol. Lett., 1991, vol. 3, no. 9, pp. 829-831

A1.7 G.E. Bodeep, and T.E. Darcie, "Comparison of second and third order distortion in intensity modulated InGaAsP lasers and $LiNbO_3$ external modulators", in Conference on Optical Fiber Communication (OFC'89), Feb. 1989, Houston, 1989 OSA Technical Digest Series (Optical Society of America, Washington DC, 1989), paper WK2, p. 86

A1.8 F. Koyama and K. Iga, "Frequency chirping in external modulators", J. Lightwave Technol., 1988, vol. LT-6, no. 1, pp. 87-93

A1.9 R.B. Childs and V.A. O'Byrne, "Predistortion linearization of directly modulated DFB lasers and external modulators for AM video transmission", in Conference on Optical Fiber Communication (OFC'90), Jan./Feb. 1990, San Francisco, CA, 1990 OSA Technical Digest Series (Optical Society of America, Washington DC, 1990), paper WH6, p.79

A1.10 R.M. Deridder and S.K. Korotky, "Feedforward compensation of integrated optic modulator distortion", in Conference on Optical Fiber Communication (OFC'90), Jan./Feb. 1990, San Francisco, CA, 1990 OSA Technical Digest Series (Optical Society of America, Washington DC, 1990), paper WH5

APPENDICES

Appendix 1.1: Description of a representative optical subcarrier-multiplexed link for AM-VSB modulated CATV video channels using external optical intensity modulation

The use of single mode fibre links to carry amplitude modulated vestigial sideband (AM-VSB) CATV channels is attractive as a means of extending a CATV distribution zone previously served by coaxial cable feeders alone, particularly when EDFAs are also used together with optical splitters in cascade configurations [A1.1]. These SMF links can be inserted into an existing coaxial system without the need for an additional set-top unit at the subscriber's premises or costly equipment at the optical link output to convert from a more favourable transmission format such as FM. Typically, from 40 to 120 AM-VSB CATV channels may need to be transmitted over such a link, occupying frequencies between 50 and 750 MHz with a channel spacing of 6 MHz [A1.2, A1.3]. The required Carrier-to-Noise Ratio (CNR) for each channel before demodulation in a 4 MHz bandwidth is between 45 and 55 dB and the demands on linearity in the form of composite second order (CSO) and composite triple beat (CTB) distortion product specifications are also very stringent [A1.3, A1.4].

One of the main decisions in the design of a suitable SMF link concerns the method of achieving optical intensity modulation. Direct modulation of the laser injection current entails the need for a consistently high linearity of light output - drive current characteristic which can lead to a poor yield of adequate devices [A1.5]. In addition, the interaction of the frequency chirp, which accompanies direct laser modulation, with SMF group velocity dispersion [5.1.2] or nonuniform EDFA gain spectra [A1.6] produces distortion.

External intensity modulation of light from a laser using a Mach-Zehnder modulator fabricated from electro-optic waveguides, e.g. in $LiNbO_3$, is not immediately obvious as the preferred alternative, since such devices have inherently nonlinear

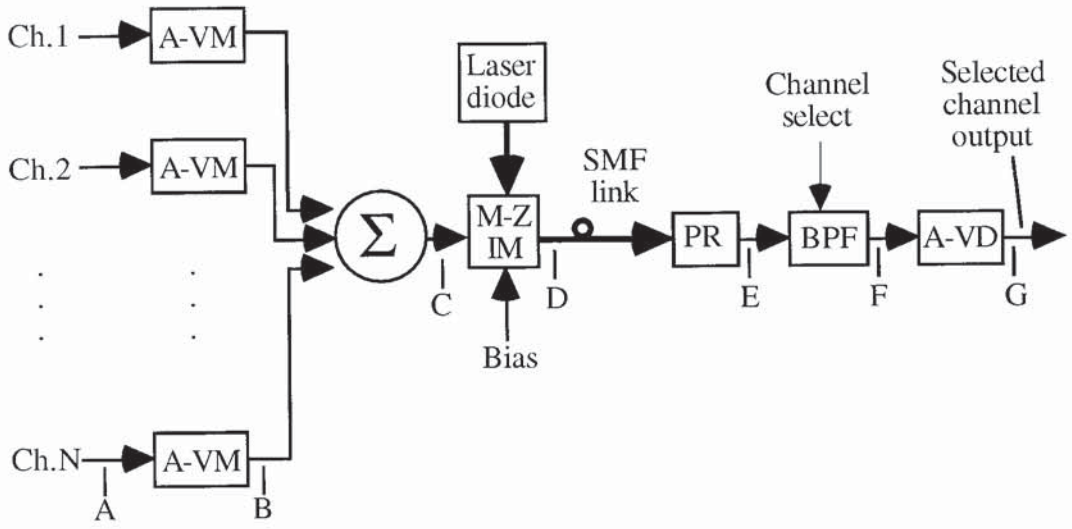

Fig. A1.1: Typical configuration of an AM-VSB modulated subcarrier-multiplexed optical link, in which the blocks A-VM represent AM-VSB modulators, Σ : linear summation, M-Z IM : Mach-Zehnder Intensity Modulator, PR : PIN-diode based optical receiver, BPF : tunable bandpass filter, A-VD : AM-VSB demodulator. Bold arrows represent optical paths while normal thickness arrows correspond to electrical paths.

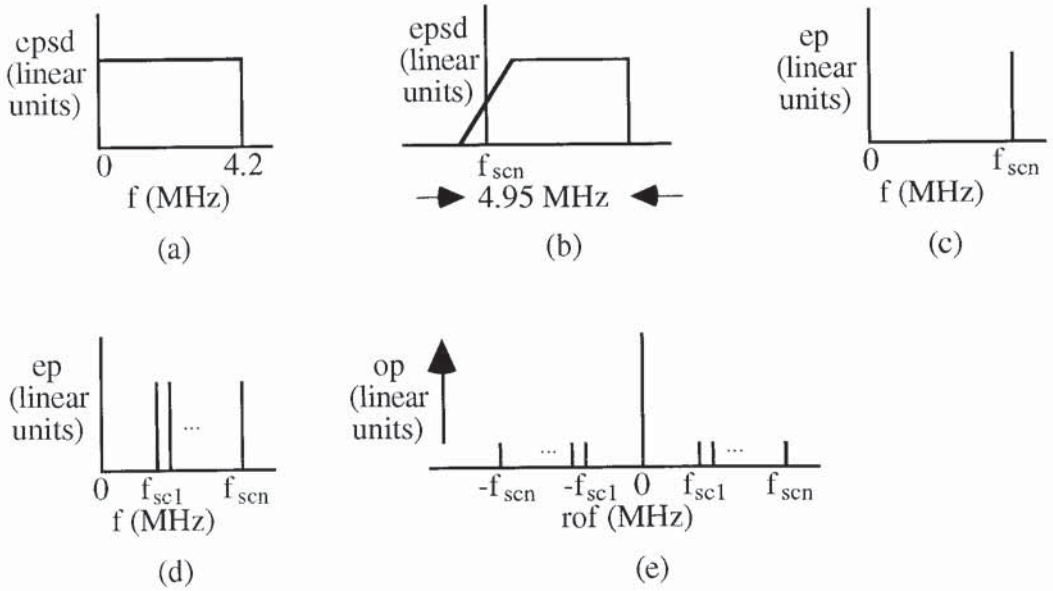

Fig. A1.2: Electrical and optical power spectra at various points in the typical AM-VSB modulated subcarrier-multiplexed optical link of fig. A1.1: (a) representative electrical power spectrum for a NTSC CATV channel at points A and G, (b) corresponding AM-VSB modulated spectrum at B and F, (c) spectrum of unmodulated electrical carrier at B and F for a DC input at A, (d) spectrum of unmodulated electrical carriers at C and E, (e) optical power spectrum at D corresponding to electrical power spectrum of (d). The following abbreviations are used: epsd : electrical power spectral density, ep : electrical power, op : optical power, rof : optical frequency relative to that of optical carrier, f_{sc1} : frequency of electrical carrier (or optical subcarrier) for channel 1, f_{scn} : frequency of electrical carrier (or optical subcarrier) for channel N.

light output - drive voltage characteristics. However, second order distortion products are extremely low when the modulator is biased at the half-transmission point [A1.7] and chirp can be eliminated [A1.8]. The unacceptably large triple beat distortion products can be reduced by electronic predistortion [A1.9], feedforward compensation [A1.10] or the use of a more complex, linearised design of modulator [5.1.1].

A representative configuration of an externally modulated SMF link for the transmission of multiple AM-VSB CATV channels is shown in fig. A1.1. Electrical and optical spectra at the points indicated in fig. A1.1 are shown in fig. A1.2. The CATV video bandwidth before AM-VSB modulation is typically 4.2 MHz and the AM-VSB channel bandwidth is 4.95 MHz with a 6 MHz channel spacing [A1.1]. It is usual to test and specify the performance of such an optical link using a matrix generator which produces an electrical waveform with a power spectrum as shown in fig. A1.2 (d), consisting of all the unmodulated electrical carriers for the channels to be transmitted. The CNR, CSO and CTB are measured for each channel at point F under this condition. The principal parameter to be optimised is the optical modulation index or depth per channel, which is defined as the peak amplitude of the optical power modulation for a channel divided by the average or unmodulated power. The optical power spectrum shown in fig. A1.2 (e) is drawn for the assumptions that the laser linewidth is negligible and that the modulation index is sufficiently small for only the fundamental modulation sidebands to be significant.

For a 60 channel experiment using electronic predistortion before the Mach-Zehnder modulator, a CNR of about 51 dB was achieved for all channels for a modulation index of 3.0% per channel, while maintaining adequate levels of CSO and CTB [A1.2]. No difference in these performance figures was observed between back-to-back attenuated optical transmission at a wavelength of 1.56 μm and transmission over 16 km of standard SMF. The experiment was repeated for the same modulation index, but with direct laser modulation instead of external modulation. In this case, the CSO distortion was increased by 12.5 dB to -41 dBc, compared to

a required value of -60 dBc, as a consequence of transmission over 16 km of SMF. The frequency chirp of the laser was 0.41 GHz/mA.

Appendix 3.1: Derivation of steady state differential equation for the photon occupation number of the SBS backscattered field envelope, assuming no depletion of the pump from SBS but only from linear attenuation

The partial differential equations of (3.1.1) together with the thermal noise term, f_{nthn}, described in (3.1.6) to (3.1.10) in accordance with [2.1.8], are taken as the starting point:

$$[\partial/\partial\tau + \partial/\partial\zeta]E_{1n} = -E_{2n}Q - \alpha_n E_{1n} \qquad \text{(A3.1.1a)}$$

$$[\partial/\partial\tau - \partial/\partial\zeta]E_{2n} = E_{1n}Q^* - \alpha_n E_{2n} \qquad \text{(A3.1.1b)}$$

$$[\partial/\partial\tau + \delta]Q = \gamma_n E_{1n}E_{2n}^* + f_{nthn}. \qquad \text{(A3.1.1c)}$$

Taking Fourier transforms with respect to the unnormalised time variable, t, of the corresponding ordinary differential equations along their characteristics, after expressing τ in (A3.1.1c) as tv_g/L and taking the complex conjugate of (A3.1.1c) yields:

$$[d/d\zeta + \alpha_n]E_{1n} = -E_{2n} * Q \qquad \text{(A3.1.2a)}$$

$$[-d/d\zeta + \alpha_n]E_{2n} = E_{1n} * Q^* \qquad \text{(A3.1.2b)}$$

$$[-i\omega_n + \delta]Q^* = \gamma_n E_{1n}^* * E_{2n} + f_{nthn}^*, \qquad \text{(A3.1.2c)}$$

where $\omega_n = \omega L/v_g$ is a normalised angular frequency variable, E_{1n},E_{2n} , Q and f_{nthn} are the Fourier transforms of E_{1n}, E_{2n}, Q and f_{nthn}, and $A * B$ represents the convolution of A with B. If the pump is assumed to be a CW carrier with negligible linewidth and if depletion of the pump is small enough at all frequencies other than the carrier frequency, then E_{1n} may be approximated as

$$E_{1n} = c_{1n}\delta(f), \qquad \text{(A3.1.3)}$$

where e_{1n} is a function only of distance and not relative frequency, f, under steady state conditions. In these circumstances, $E_{2n}\{\zeta\}$ may be solved as a function of $e_{1n}\{\zeta\}$ by first rewriting (A3.1.2b) and (A3.1.2c) as

$$[-d/d\zeta + \alpha_n]E_{2n} = e_{1n}Q^* \qquad \text{(A3.1.4a)}$$

$$[-i\omega_n + \delta]Q^* = \gamma_n e_{1n}E_{2n} + f_{nthn}^* . \qquad \text{(A3.1.4b)}$$

Substituting Q^* from (A3.1.4b) into (A3.1.4a) and expressing this in terms of the unnormalised distance variable, z, instead of ζ gives

$$[-d/dz + \alpha_n/L]E_{2n} = [L(-i\omega_n + \delta)]^{-1}[\gamma_n e_{1n}^2 E_{2n} + e_{1n}f_{nthn}^*]. \qquad \text{(A3.1.5)}$$

Now,

$$[-d/dz](E_{2n}.[E_{2n}]^*) = E_{2n}.[-d([E_{2n}]^*)/dz] + [E_{2n}]^*.[-d(E_{2n})/dz] - dz.[-d(E_{2n})/dz].[-d([E_{2n}]^*)/dz], \qquad \text{(A3.1.6)}$$

where the last of these terms normally vanishes but should be considered for the f_{nthn}^* component. Applying (A3.1.5) and its complex conjugate in (A3.1.6) results in:

$$[-d/dz](E_{2n}.[E_{2n}]^*) = (-2\alpha_n/L).(E_{2n}.[E_{2n}]^*) + (\omega_n^2 + \delta^2)^{-1}.[(2\gamma_n e_{1n}^2\delta/L).(E_{2n}.[E_{2n}]^*) - (dz).(e_{1n}^2/L^2).(f_{nthn}^*.[f_{nthn}^*]^*)]. \qquad \text{(A3.1.7)}$$

Now $(E_{2n}.[E_{2n}]^*)$ is equal to the normalised energy spectral density of E_{2n} and is the Fourier transform of the autocorrelation function of E_{2n}, which is an integral with respect to time. Let H_{e2n} be the normalised power spectral density of E_{2n}, equal to the Fourier transform of the average autocorrelation of E_{2n}, which may be defined as the autocorrelation function for a large but finite integration time interval divided by that time interval. Then (A3.1.7) may be rewritten as

$$[-d/dz]H_{e2n} = (-2\alpha_n/L).H_{e2n} + (\omega_n^2 + \delta^2)^{-1}.\ [(2\gamma_n e_{1n}^2\delta/L).H_{e2n} - (dz).(e_{1n}^2/L^2).H_{fnthn}], \qquad (A3.1.8)$$

where H_{fnthn} is the power spectral density of f_{nthn} and is equal to the Fourier transform of (3.1.9). If f_{nthn} is considered to be averaged over the distance interval of dz, then from (3.1.9), (3.1.10) and [2.1.8],

$$\begin{aligned} H_{fnthn} &= K_9^2.Q_{thn}/(dz) \\ &= \delta^2L^2.(g_B c k_B T/(2n\nu_a A_{eff}))/(dz). \end{aligned} \qquad (A3.1.9)$$

If the normalised power spectral density, H_{e2n}, is converted to the dimensionless photon occupation number of the Stokes wave, N_s, by multiplying (A3.1.8) by $P_{p0}/h\nu$, where P_{p0} is the input pump power and $h\nu$ is the photon energy, and if the frequency dependence is expressed in terms of

$$\begin{aligned} R\{f\} &= 1/(1 + (f/(\Delta\nu_B/2))^2) \\ &= 1/(1 + (\omega_n/\delta)^2), \end{aligned} \qquad (A3.1.10)$$

then (A3.1.8) becomes

$$\begin{aligned} [-d/dz]N_s &= (-2\alpha_n/L).N_s + R\{f\}.[(2\gamma_n e_{1n}^2/(\delta L)).N_s - (dz).(e_{1n}^2/(\delta^2L^2)).H_{fnthn}.P_{p0}/h\nu] \\ &= -\alpha N_s + R\{f\}.[(g_B P_{p0} e_{1n}^2/A_{eff}).N_s - e_{1n}^2(g_B c k_B T/(\lambda\nu_a A_{eff})).P_{p0}/h\nu] \\ &= (g_B\{f\}S_p\{z\}).(N_s + n_a) - \alpha N_s, \end{aligned} \qquad (A3.1.11)$$

where the definitions of α_n, γ_n, and ν_a given in (3.1.2), (3.1.3) and (2.1.6) have been applied, $S_p\{z\} = P_{p0}e_{1n}^2/A_{eff}$ is the pump intensity as a function of distance, $g_B\{f\} = g_B R\{f\}$ is the effective steady state Brillouin gain coefficient as a function of relative frequency and $n_a = k_B T/h\nu_a$ is approximately equal to the mean number of phonons per mode of the acoustic field given for (2.1.21) at room temperature.

(A3.1.11) is precisely the differential equation quoted by R.G. Smith in (B1) of [1.2.5] and reproduced as (2.1.21).

Appendix 3.2: Derivation of theoretical "inferred" SBS noise spectrum for CW optical carrier after transmission

The spectrum of the transmitted field may be obtained from (A3.1.2a) as:

$$[d/d\zeta + \alpha_n]E_{1n}(f_d) = -E_{2n} * Q$$
$$= -\int E_{2n}(f).Q(f_d - f)\, df. \qquad (A3.2.1)$$

If Q is determined from (A3.1.1c) using the same assumptions made in Appendix 3.1 that the pump is a CW carrier with negligible linewidth and that pump depletion is small enough at all frequencies other than the carrier frequency for E_{1n} to be approximated as $E_{1n} = e_{1n}\delta(f)$, then

$$[-i\omega_n + \delta]Q = \gamma_n e_{1n} E_{2n}^* + f_{nthn}\,. \qquad (A3.2.2)$$

A differential equation for the depletion at the carrier frequency as a function of the SBS backscattered power spectral density may be obtained by substituting Q from (A3.2.2) with $f_{nthn} = 0$ into (A3.2.1) for $f_d = 0$, noting that $E_{2n}^*(-f) = [E_{2n}(f)]^*$, and applying a similar method to that of Appendix 3.1 for deriving the pump power from the pump field:

$$[d/dz + \alpha]S_p\{z\} = -\int(g_B\{f\}S_p\{z\}H_s\{f,z\}/A_{eff})\, df, \qquad (A3.2.3)$$

where $S_p\{z\} = P_{p0}e_{1n}^2/A_{eff}$ is the pump intensity as a function of distance, $g_B\{f\} = g_B R\{f\}$ is the effective steady state Brillouin gain coefficient as a function of relative frequency and $H_s\{f,z\} = h\nu.N_s\{f,z\}$ is the SBS backscattered power spectral density.

A minimum limit for the SBS transmitted power spectral density, $H_{pmin}\{f_d, z\}$, may be evaluated by substituting Q from (A3.2.2) with $E_{2n}^* = 0$ into (A3.2.1), and

applying a similar method to that of Appendix 3.1 for deriving the pump power spectral density from the pump field:

$$[d/dz + \alpha]H_{pmin}\{f_d, z\} = - h\nu.n_a.\int(g_B\{f_d - f\}H_s\{f, z\}/A_{eff})\, df. \qquad (A3.2.4)$$

This "inferred" transmitted SBS noise may be simulated by numerically solving (A3.1.1a) to (A3.1.1c) to give E_{2n} and substituting this into corresponding modified versions (A3.1.1a') and (A3.1.1c'), in which new variables E_{1nx} and Q_x replace E_{1n} and Q and in which the product term $\gamma_n E_{1n} E_{2n}^*$ of (A3.1.1c) is not present in (A3.1.1c'). In order to ensure that the inferred noise represents a minimum limit, a different thermal noise variable f_{nthnx} is used in (A3.1.1c') instead of f_{nthn} in (A3.1.1c), where f_{nthnx} has the same statistics as f_{nthn} but is uncorrelated with it.

Appendix 5.1: Calculation of $CNR_{c\text{-}nxsc}$, the detected subcarrier to noise ratio for noise from the beat product of carrier with subcarrier sideband SBS inferred noise

As stated at the end of section 5.1, the output field $E_{1nhlm}(\zeta=1)$ inferred for high L_m can be derived from the sum of the DFT of the inferred transmitted SBS noise field $E_{1xn}(\zeta=1)$ at all frequencies and the DFT of the total output field $E_{1n}(\zeta=1)$ at the identified signal frequencies of f_c, $f_c + f_{sc}$ and $f_c - f_{sc}$ where f_c and f_{sc} are the optical carrier and detected subcarrier frequencies, respectively. If only the noise from the beating of the carrier with the SBS noise at the subcarrier sidebands is considered, then let the transmitted field representing these components be given by

$$E_{1nh1} = E_c + n_x \exp(i\omega_n t), \qquad \text{(A5.1.1)}$$

where E_c is $E_{1n}(\zeta=1)$ at f_c, n_x is the inferred transmitted SBS noise field envelope at $f_c + f_n$, and $\omega_n = 2\pi f_n$. The normalised detected power, P_{1nh1}, which may be defined as

$$P_{1nh1} = E_{1nh1}E_{1nh1}^*, \qquad \text{(A5.1.2)}$$

is then determined as

$$\begin{aligned} P_{1nh1} &= |E_c|^2 + |n_x|^2 + (E_c n_x^* \exp(-i\omega_n t) + \text{c.c.}) \\ &= |E_c|^2 + |n_x|^2 + 2E_c n_x^* \cos(\omega_n t). \end{aligned} \qquad \text{(A5.1.3)}$$

For negligible SBS depletion of the optical carrier and in the absence of noise, the normalised optical power at the fibre output of the carrier modulated by the subcarrier is proportional to that given in (5.1.4) and is given by

$$P_{1nso} = |E_c|^2 (1 + m_{sc} \cos(2\pi f_{sc} t)). \qquad \text{(A5.1.4)}$$

The ratio of the power of the component of detected signal photocurrent at the subcarrier frequency, f_{sc}, to the power of the component of detected noise photocurrent in a defined bandwidth B_{sc} near f_{sc} is therefore

$$\begin{aligned} CNR_{c\text{-}nxsc} &= |E_c|^4 \, m_{sc}^2/(4 \, |E_c|^2 \, N_{scb}) \\ &= |E_c|^2 \, m_{sc}^2/(4 \, N_{scb}) \end{aligned} \qquad \text{(A5.1.5)}$$

where N_{scb} is the total inferred transmitted SBS optical noise power in bandwidths of B_{sc} near $f_c + f_{sc}$ and near $f_c - f_{sc}$.

ABBREVIATIONS

acf	autocorrelation function
AM	amplitude modulation
AM-VSB	amplitude modulation with vestigial sideband
ASK	amplitude shift keying
BER	bit error rate
BGB	Brillouin gain bandwidth
bgcs	Brillouin gain coefficient spectrum
BGL	Brillouin gain linewidth
BGS	Brillouin gain spectrum
BSF	Brillouin shift frequency
CATV	community antenna television
CMI	complementary mark inversion
CNR	carrier-to-noise ratio
CPFSK	continuous phase frequency shift keying
CSO	composite second order distortion product specification
CTB	composite triple beat distortion product specification
CW	continuous wave (i.e. unmodulated)
DFT	discrete Fourier transform
DTAN	distributed thermal acoustic noise
EDFA	Erbium-doped fibre amplifier
FFT	fast Fourier transform
FM	frequency modulation
FSK	frequency shift keying
FWHM	full width between half maximum points
FWM	four wave mixing
GVD	group velocity dispersion
LAN	Local Area Network
MAN	Metropolitan Area Network

MFL (or L_m)	model fibre length
MPI	multipath interference
NFM	Nonuniform Fibre Model
NRZ	non-return-to-zero (a NRZ data pulse corresponding to a logical 1 does not include any excursions to the level corresponding to a logical 0)
nsd	normalised standard deviation (= standard deviation/mean)
ODE	ordinary differential equation
PDE	partial differential equation
pdf	probability density function
PIN	positive-intrinsic-negative (refers to doping of semiconductor layers in a type of photodiode)
psd (or PSD)	power spectral density
PSK	phase shift keying
RHS	right hand side
RIN	relative intensity noise
SBS	stimulated Brillouin scattering
SDRS	signal double Rayleigh scattering
SMF	single-mode optical fibre
SOP	state of polarisation
SPM	self phase modulation
SRS	stimulated Rayleigh scattering
SSDDN	Stokes-spontaneous density depletion noise
ssgsf	steady state gain of the Stokes field
TDM	time division multiplexing
UFM	Uniform Fibre Model
WDM	wavelength division multiplexing
XPM	cross phase modulation